Modelling of Optical Gates for Quantum Information Processing.

Taherkhani, Masoomeh

Publication date:
2018

Document Version
Publisher's PDF, also known as Version of record

Modelling of Optical Gates for Quantum Information Processing

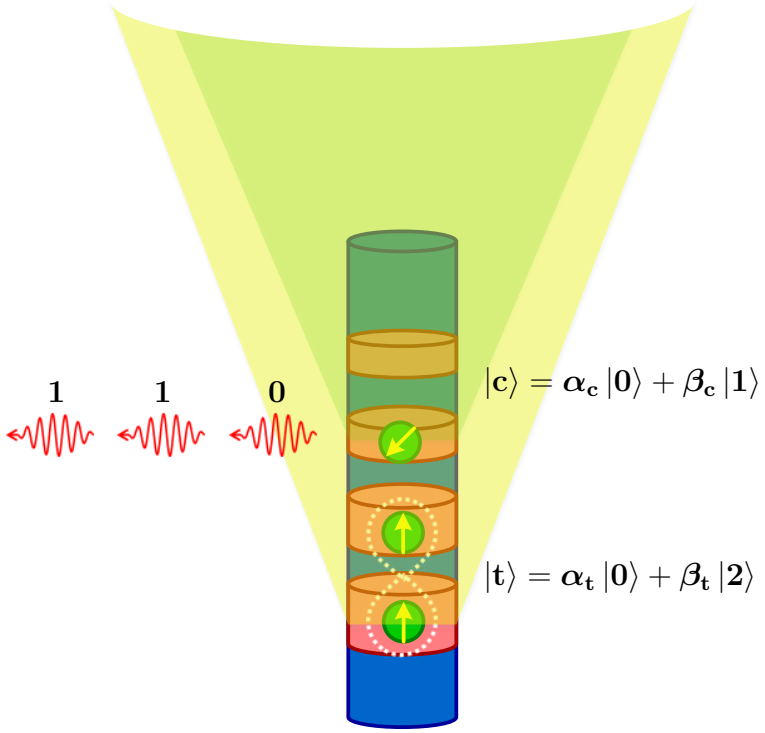

A dissertation submitted in partial fulfillment of the requirements for the degree of Doctor of Philosophy

Masoomeh Taherkhani

Ph.D. Thesis

July 2018

DTU Fotonik

Department of Photonics Engineering

Technical University of Denmark

Project period	May 2015 - July 2018
Main Supervisor	Assoc. Prof. Niels Gregersen
Co-supervisors	Prof. Jesper Mørk Assoc. Prof. Morten Willatzen Dr. Dara P. S. McCutcheon
Ph.D. defense committee	Prof. Antti-Pekka Jauho, Technical University of Denmark Dr. Oliver Marquardt, Weierstrass Institute Assoc. Prof. Nikolaj Thomas Zinner, Aarhus University
Comments and feedback	masoomehtaherkhani@gmail.com

Abstract

A numerical tool is developed to calculate the exciton energy and oscillator strength in newly emerged type-II nanowire quantum-dots. For a single-quantum-dot, the poor overlap of the electron part and the weakly confined hole part of the exciton wavefunction leads to a small oscillator strength compared to type-I systems. To increase the oscillator strength, we propose a double-quantum-dot structure featuring a strongly localized exciton wavefunction and a corresponding four-fold relative enhancement of the oscillator strength, paving the way towards efficient optically controlled quantum gate applications in the type-II nanowire system.

Next, an optical gating scheme for quantum computing based on type-II double-quantum-dots is proposed. The qubit is encoded on the electron spin and the gate operations are performed by stimulated Raman adiabatic passage (STIRAP) using the position degree of freedom in double-quantum-dots to form an auxiliary ground-state. Successful STIRAP gating processes require an efficient coupling of both qubit ground-states of the double-quantum-dot to the gating auxiliary state and we demonstrate that this can be achieved using a charged exciton state. Crucially, by using type-II quantum-dots, the hole is localized between the two spatially separated electrons in the charged-exciton complex, thereby efficiently coupling the electron states orbitals. We subsequently exploit the scheme to realize single- and two-qubit gates for quantum computation. The conditional operation is performed by using Coulomb coupling to induce a shift of the STIRAP transition frequencies leading to a conditional violation of the STIRAP two-photon resonance. We calculate the fidelity of gates and show their performance is robust against the spin and charge noises.

Preface

This thesis is submitted to the DTU Fotonik, the Department of Photonics Engineering at Technical University of Denmark (DTU) for the partial fulfillment of the degree of Doctor of Philosophy (Ph.D.). The work presented here is part of the Ph.D. project, which was carried out in the Quantum and Laser Photonics group from May 15th, 2015 to July 14th, 2018. The project has been supervised by main supervisor, Assoc. Prof. Niels Gregersen and co-supervisors, Prof. Jesper Mørk, Assoc. Prof. Morten Willatzen (February 2016-July 2018) and Dr. Dara McCutcheon (May 2015-February 2016) all from DTU Fotonik. The Ph.D. project was financed by Danish National Research Council for Technology and Production, 4005-00370, 703193.

Acknowledgments First and foremost, I am indebted to my supervisors and grateful for their guidance and input in the course of the project. I thank my mentor and main supervisor Niels whom I learned a lot for giving me the opportunity to grow and learn on many levels in the awesome atmosphere of DTU Photonics. I thank my co-supervisor Jesper for providing valuable supervision and encouraging input to the project with his enormous physical insight. I thank Dara for always having the time to discuss the little details and the big picture of the project and for being enthusiastic and persistent about my work. I give my deep thank you to Morten for the very informative guidance giving me on the semiconductor band structure and for his availability and assistance even during his stay in China. I should also thank Emil who contributed to my project with his solid theoretical knowledge. I also thank Nika to give me very informative input on the experimental point of view.

I thank all members of the Laser and Quantum Photonics group at DTU Photonics for creating an inspiring scientific atmosphere.

I wish to acknowledge Danish National Research Council for Technology and Production for financing the Ph.D. project, and Otto Mønsteds economical support toward the conference participation.

Now since I started expanding my thanks, I have to thank also my friends in Denmark (Azita, Maryam, Nezam, Nasim, Ali, Sanaz, Behzad, Iman, Elham) who I had fun with on weekends and vacations and got the energy for the week.

I should thank my colleagues and friends (Antonio, Daniel, Christine, Lorenzo, Andreas, Hafeez, Armin, Maryam, Simin, Ehsan) at DTU who we enjoyed the lunch, Friday bar, and the coffee break where we had funny discussions about news, science, life, and even politics.

Last but not least, I would like to thank my whole family and also my relatives who all support me throughout my life.

Publications

Journal Publication

- M. Taherkhani, M. Willatzen, J. Mørk, N. Gregersen, D. P. S. McCutcheon, "Type-II quantum-dot-in-nanowire structures with large oscillator strength for optical quantum gate applications", Physical Review B, vol: 96, no: 12, 2017

Submitted Manuscript

- M. Taherkhani, M. Willatzen, Emil V. Denning, I. E. Protsenko, and Niels Gregersen, "Optical quantum gates based on type II double quantum dots in a nanowire", submitted

Conference proceedings

- M. Taherkhani, N. Gregersen, J. Mørk, D. P. S. McCutcheon, M. Willatzen, "Efficient modeling of Coulomb interaction effect on exciton in crystal-phase nanowire quantum Dot", 16th International Conference on Numerical Simulation of Optoelectronic Devices (NUSOD), 2016, Sydney

- M. Taherkhani, N. Gregersen, M. Willatzen, J. Mørk, "Type-II quantum dot nanowire structures with large oscillator strengths for optical quantum gating applications", 17th International Conference on Numerical Simulation of Optoelectronic Devices (NUSOD), 2017, Copenhagen

- M. Taherkhani, N. Gregersen, J. Mørk, M. Willatzen, "Efficient modeling of excitons in type-II nanowire quantum dots", The European Conference on Lasers and Electro-Optics, CLEO Europe, 2017, Munich

Contents

Contents **vii**

1 Introduction **1**

2 Background and theory **9**

2.1 Type-II versus type-I quantum-dot 9

2.2 Modeling of the quantum-dots 11

2.2.1 Our modeling method 13

2.3 Modeling the exciton state 20

2.3.1 Configuration-interaction method 22

2.4 Stimulated Raman adiabatic passage (STIRAP) 23

2.4.1 STIRAP theory 24

2.4.2 Condition for the adiabatic following 30

2.4.3 Further aspects of the three-level STIRAP 31

2.5 Summary 34

3 Coulomb interaction **37**

3.1 Exciton 37

3.2 Oscillator strength 40

3.3 Convergence study of the configuration-interaction method . . 42

3.4 Exciton states in type-II QDs in nanowires 44

3.4.1 Single-quantum-dot in a nanowire 45

3.4.2 Double-quantum-dot in a nanowire 51

3.5 Exciton states in type-I QDs in nanowires 58

3.6 Validation of the results 61

3.7 Summary 65

4 Quantum gates **67**
4.1 Physical implementation of the three-state STIRAP in type-II double-quantum-dot . . . 69
4.2 Single-qubit rotation by stimulated Raman adiabatic passage . 72
4.2.1 Physical implementation of the four-state system in a type-II double-quantum-dot . . . 76
4.2.2 Charged-exciton state . . . 78
4.3 Two-qubit gate . . . 83
4.4 Fidelity . . . 88
4.4.1 Effects of decoherence . . . 89
4.4.2 Initializing electrons in DQDs in a nanowire . . . 92
4.5 Summary . . . 93

5 Conclusion and outlook **95**
5.1 Summary . . . 95
5.2 Future work . . . 98

Appendices **100**

A Single-particle solutions **101**
A.1 Solution in the z-direction . . . 102
A.2 Solution in the transverse direction . . . 102

B Basic differential equations of the STIRAP **107**
B.1 Interaction of a two-state system with a classical field . . . 107
B.2 Interaction of a three-state system with a classical field . . . 110

C Dipole moment in a periodic potential **113**

D Complementary results on exciton states **115**

Bibliography **121**

List of Abbreviations

1D ..... One-dimensional, one dimension.

2D ..... Two-dimensional, two dimensions.

2DEG ..... Two-dimensional electron gas.

3D ..... Three-dimensional, three dimensions.

CI ..... Configuration interaction.

CNOT ..... Controlled Not gate.

DQD ..... Double quantum dot.

FEM ..... Finite element method.

NV ..... Nitrogen vacancy.

OS ..... Oscillator strength.

QD ..... Quantum dot.

SQD ..... Single quantum dot.

STIRAP ..... Stimulated Raman adiabatic passage.

WZ ..... Wurtzite.

ZB ..... Zinc blende.

CHAPTER 1

Introduction

In this introductory chapter, we briefly describe the perspectives, structures, and methods covered in this thesis. Literature surveys on specific topics are presented in the next chapter.

Quantum information processing

The advent of quantum information processing, as an abstract concept, has given birth to a great deal of new thinking, in a very concrete form, about how to create physical computing devices that operate in the formerly unexplored quantum mechanical regime [1]. The non-classical correlations of quantum mechanics recently has been exploited in a wide range of applications with impact outside the laboratories. Quantum cryptography [2] guarantees secure exchange of information and quantum computation [3] brings algorithms which outshine their classical counterparts. The initial concern that quantum coherence may be too fragile to be exploited has been dispelled by theoretical works showing that noise and decoherence are not fundamental obstacles to the implementation of quantum information processing [4, 5]. Consequently, increasing effort is being devoted towards physically realizing quantum computers and there are many proposals, including those based on atomic or molecular systems [6, 7] and others based on solid state approaches [8].

In this thesis, we use type-II quantum-dots (QDs) in nanowires as a platform for realizing a quantum computer. The work to be reported here is focused on the modeling and simulating these systems by developing a fast and efficient numerical tool based on the configuration-interaction method. We aim to design optical quantum gates for quantum computation based on the studied nanostructures.

In the following section, we provide a brief overview of quantum computation. The reader can refer to [3] for a thorough review on the subject.

Qubits and quantum gates

The fundamental unit of information in a classical computer, the bit, is a binary variable, whose value is commonly indicated by 0 or 1. In a quantum computer, bits are called qubits and encode the superposition of two states, usually indicated by $|0\rangle$ and $|1\rangle$, which for instance could be different energy levels in an atom or QD. A qubit can therefore be expressed as $|\psi\rangle = \alpha\,|0\rangle + \beta\,|1\rangle$, where the coefficients are complex numbers that fulfill the relation $|\alpha|^2 + |\beta|^2 = 1$. Qubits offer an exponential increase in computaional power with respect to classical computations. While a qubit exists in a superposition of the states $|0\rangle$ and $|1\rangle$, whenever we make a measurement, we will find that it is in either $|0\rangle$ or $|1\rangle$ with probability $|\alpha|^2$ or $|\beta|^2$, respectively, and the system collapses onto the measured state.

As in classical computation, quantum algorithms can be decomposed into gates acting on either one or two qubits. A set of gates, from which all algorithms can be created, is called *universal*. It has been shown that a complete set of single-qubit gates, plus a two-qubit gate called the controlled NOT gate (CNOT) form a universal set for quantum computation [3]. There is an infinite number of single-qubit gates possible on the state vector $|\psi\rangle$. The single-qubit gate can be visualized as a rotation of the state vector from one position on the Bloch sphere to another arbitrary point.

Although many different two-qubit gates exist, quantum computing theorists often work in terms of the CNOT gate. This gate has two inputs and two outputs, as shown in Fig. 1.1. The top qubit of the CNOT gate is called the control qubit and it is unaffected by the gate. The bottom qubit is called

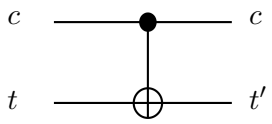

Figure 1.1: Notation for a CNOT gate, with input qubits c and t and output qubits c and t'.

Inputs		Outputs	
c	t	c	t'
0	0	0	0
0	1	0	1
1	0	1	1
1	1	1	0

Figure 1.2: Truth table for the CNOT gate

the target qubit and it is flipped if the control qubit is 1 while unaffected if the control qubit is 0. The CNOT gate's truth table is shown in Fig. 1.2.

Physical implementation of a quantum computer

Several quantum systems are being explored as qubits, each with their specific advantages and challenges. Examples include single atoms in ion traps [9], nitrogen vacancy (NV) defect centers in diamond [10], semiconductor QDs [11, 12] and superconducting circuits [13]. Among these, semiconductor-based qubits are attractive due to their electrical tunability and ease of integration with the electronics industry. However, a perfect semiconductor platform that simultaneously satisfies the requirements of fast quantum control, long coherence time, and scalability to thousands of coupled qubits has not been developed, yet. A prominent semiconductor system in which single- and two-qubit operations were demonstrated is a two-dimensional electron gas (2DEG) at the interface between GaAs and AlGaAs [14, 15]. By using metallic gates on top of the heterostructure to isolate small regions of 2DEG, QDs containing single electrons have been electrostatically defined. While two-dimensional systems currently lead the race among semiconductors, there is still a long way to a practical quantum computer. Among challenges going forward is the need to simultaneously carve zero-dimensional QDs out of a 2D sheet of electrons, and couple thousands of these dots while only being able to place control electrodes on top of a heterostructure [16]. Another drawback of two-dimensional systems is the limited design freedom of the material. In fact, in order to avoid strain and consequent incorporation of dislocations, high quality 2DEGs can only be fabricated with (nearly) lattice matched materials; this is

possible only for a small set of material combinations [17].

Another solid-state platform that has demonstrated promise for quantum computing is a semiconductor self-assembeled QD which has been widely studied since the 1990s because of its appealing electronic and photonic properties [18, 19]. However, the standard fabrication methods adopted to fabricate self-assembled QDs involve a degree of dispersity which limits exact reproducibility within an ensemble of dots [20, 21, 22]. This, in turn, poses a challenge for the scalability of many technological applications demonstrated at a single QD level. Crystal-phase QDs in nanowires [23] are likely to mitigate this problem. Nanowires are the one dimensional nanostructures grown perpendicular to the surface of the substrate, as shown in Fig. 1.3 (a) [24], usually adopting the vapor-liquid-solid (VLS) method. By controlling the temperature and the diameter of the nanowire during the growth process, it is possible to create along the nanowire different regions of zinc-blende (ZB) and wurtzite (WZ) crystal phases [23], as it is shown in Fig. 1.3 (b). Since these crystal phases of a *single material* have different band gaps at Γ point [25], the alternating ZB and WZ phases can define a QD in the nanowire which is called crystal-phase QD. The ZB and WZ regions do not intermix within a monolayer and thus always have atomically sharp interfaces, as depicted in Fig. 1.3 (c), allowing for the geometry control with the precision of a single atomic layer. This is not possible in self-assembled QDs because alloying blurs the interfaces. From the qubit scalability point of view, an important advantage of using nanowire is that they allow for multiple local metallic or superconducting contacts and electrostatic gates on top, beneath, and next to the wire [26, 27]. Furthermore, due to the small transverse dimension of nanowires, strain can be relieved at their surface. This allows an almost unlimited material design freedom in terms of the chemical composition.

The WZ-ZB interface is well known to exhibit a type-II band alignment, with conduction and valence bands in WZ phase being higher than in the ZB phase. In crystal-phase QDs this type-II band alignment entails that the electron and hole are confined on different crystal phases, whereas in conventional type-I QDs the electron and hole are confined on the same site [28, 29]. While extensive studies of optical properties in type-I QDs are already available in the literature (e.g., [30, 31, 32]), studies of the optical properties

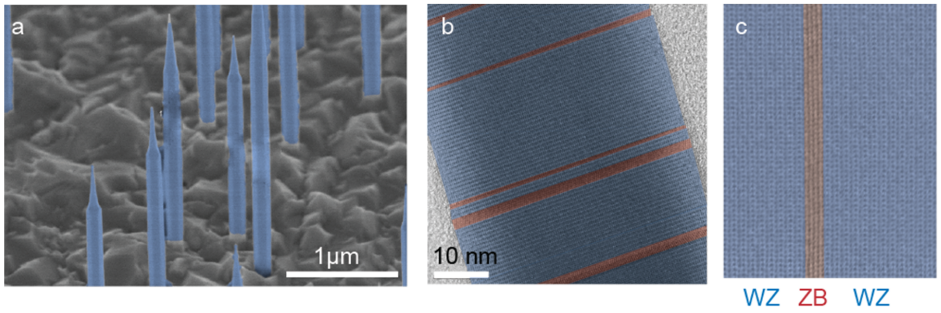

Figure 1.3: (a) Scanning electron microscope image of the InP nanowire sample. (b) Transmission electron microscopy of the InP nanowires showing short segments of the zinc-blende (red) in a wurtzite (blue) nanowire. (c) A high resolution-transmission electron microscopy image of the zinc-blende segment in the otherwise wurtzite lattice [24].

of type-II QDs have only recently been initiated [33, 34]. For this reason we study the novel crystal-phase type-II QDs in nanowires and use them as platform for designing optical quantum gates for quantum computation.

Computational framework

In this thesis, we develop a numerical tool for simulating and modeling of type-II QDs in nanowires. An introduction to the description of single-particle energies and wavefunctions of carriers in crystal-phase QDs in nanowires is given in Chapter 2. Consecutive derivation of many-particle states of an interacting electron and hole in a configuration-interaction scheme is presented in Chapter 3 by usage of the previously calculated single-particle wave functions and energies. Configuration-interaction is a numerical method with which one may solve the Schrödinger equation for a system with a few interacting particles [35]. This method has many advantages, but its main drawback is that it can only handle very small systems, say five particles or so [36]. For larger systems, the workload becomes much too large for nowadays computers.

The calculation procedure of the interacting electron-hole system in this thesis by means of the configuration-interaction method can be summarized as follows:

1. The single-particle states in a QD in a nanowire with specific geometrical

and material parameters are calculated by solving the single-particle Schrödinger equation using finite difference equations (Chapter 2).

2. The configuration-interaction Hamiltonian for interacting electron and hole systems is generated (Chapter 3).

3. The configuration-interaction Hamiltonian for each interacting electron-hole system is diagonalized (Chapter 3).

The details of the method and also its strengths and weaknesses are discussed in Chapter 2 and 3. The convergence of the configuration-interaction method is studied and the calculation results are compared to that of a semi-analytical solution of the exciton problem, solved by using COMSOL finite element method (FEM). Based on the structure studied in Chapter 3, universal, addressable and scalable single- and two-qubit gates for quantum computation are proposed in Chapter 4.

Scope of the thesis

Two overall goals of the project reported in this thesis are: **(1)** developing a numerical tool to study the optical properties of the novel type-II crystal-phase QDs and **(2)** to use the results and the framework for designing optical quantum gates.

The thesis is done in the Quantum and Laser Photonics group where we work theoretically and experimentally to explore the fundamentals of light-matter interactions in nanostructures. The initial motivation to work on this *new* subject in the group was to provide the essential theory for analyzing the experimental results of our experimentalist collaborators at DTU Photonics. qLab at DTU Photonics founded in 2015, has started to operate recently in 2018 due to some technical challenges. Because of this delay, the work reported here is restricted to the *theoretical* modeling and investigation.

Structure of the thesis

The thesis is divided into five chapters and below we provide short summaries of structures and methods.

Chapter 1, Introduction: The main motivations of the work are reviewed.

Chapter 2, Background and theory: The preliminaries of theory and structures that we use and build on in the following chapters are presented. The methods of calculating single-particle states and exciton states are reviewed. Single-particle states in type-II QDs are calculated. The theory of the stimulated Raman adiabatic passage (STIRAP) for quantum gating is outlined and its main features are explained.

Chapter 3, Coulomb interaction: Using an efficient method based on a configuration-interaction description, the main properties of excitons in type-II single and double quantum dots in nanowires is investigated. Energy spectra, oscillator strengths, and electron and hole exciton sizes are calculated as a function of the all relevant geometrical parameters. We propose a double quantum dot (DQD) structure for which the exciton oscillator strength can be increased to more than four times its value compared to that of a single quantum dot (SQD) nanowire while the exciton remains well-confined to the DQD region. The convergence of the method is studied and its accuracy is validated.

Chapter 4, Quantum gates: We demonstrate the less explored type-II DQD system performs significantly better than the traditional type-I DQD for optical quantum gating by using the STIRAP. We develop a multi-band formalism and show that a charged exciton state with a mixed hole provides efficient coupling in the STIRAP scheme without involving additional external fields. The Coulomb interaction leading to a conditional violation of the STIRAP two-photon resonance condition is used to implement two-qubit CNOT gate. The robustness of the scheme against charge and spin noises is investigated.

Chapter 5, Conclusion and Outlook: The major results of this thesis are summarized and the possible future extension of the work are also discussed.

CHAPTER 2

Background and theory

In this chapter, the relevant background to the rest of the thesis will be set out. The chapter doesn't include any new work which we are contributing and we just outline here the framework we are working in. The chapter is organized as follows. First, the difference between type-I and type-II QDs is discussed. Then, details of the single-particle energy and wavefuction calculation is presented. The Hamiltonian of the interacting electron-hole system is written and the method to solve it, is introduced. Finally, the stimulated Raman adiabatic passage is outlined and its main features will be discussed.

2.1 Type-II versus type-I quantum-dot

We distinguish between two types of QDs. In type-I QDs, the band gap of one material is contained entirely within that of another. In this case, both the electron and hole are confined in the material with the narrower band gap as shown in Fig. 2.1 (a) for a SQD configuration. However, in the recently emerging type-II QD systems [37, 38, 39], both the conduction band (CB) and the valence band (VB) edges of one material lie above the corresponding edges of the neighboring material, which typically results in the electron and hole being confined in different regions as shown in Fig. 2.1 (b). In general, type-II QDs have shown interesting physics, such as the Aharanov-Bohm effect [40], excitonic Mott transitions [41], and applications to solar cells and photon-

detectors [42]. In this work we show that they have also promising features for application in quantum computation. When encoding the qubits on the excitons (bound electron-hole pair) of neighboring QDs, two-qubit operations can be performed using controlled interaction of the excitons in the QDs [43]. In a type-I DQD configuration, the interaction between two excitons confined inside the QDs as shown in Fig. 2.2 (a) is weak even when two QDs are in a close proximity to each other, and an external electric field is needed in these systems to make the excitons interact with each other [44]. In contrast, in a type-II DQD structure, since the hole state is confined between two QDs as illustrated in Fig. 2.2 (b), interaction is possible even in the absence of an external electric field or when the QDs are far from each other. This feature makes type-II QDs a promising structure for implementing quantum gates [33]. Extensive studies of exciton properties in type-I QDs have been

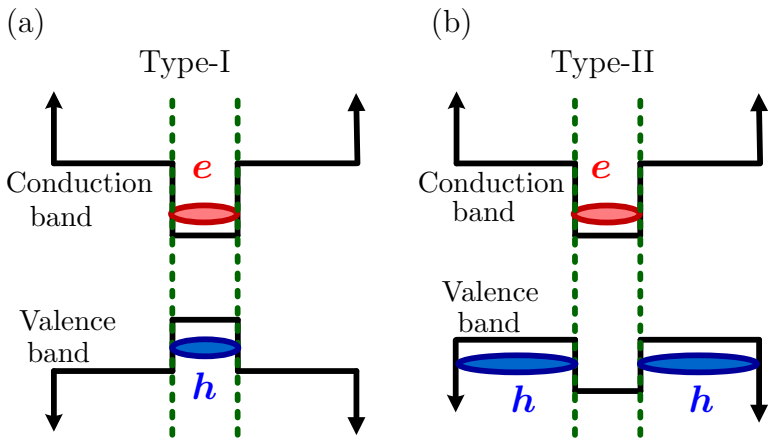

Figure 2.1: The conduction and valence band potential profiles of a (a) type-I and (b) type-II quantum dot.

conducted [30, 31], and exploitation of type-I QD structures for quantum gate operations have been proposed [45, 46, 47]. However, studies of the optical properties of type-II QDs have only recently been initiated, and a detailed scheme for using type-II QDs for implementing quantum gates has not yet been proposed to the best of our knowledge.

For this reason, we study optical properties of the type-II QDs in this thesis. We consider type-II InP crystal-phase QDs in a nanowire, as is shown

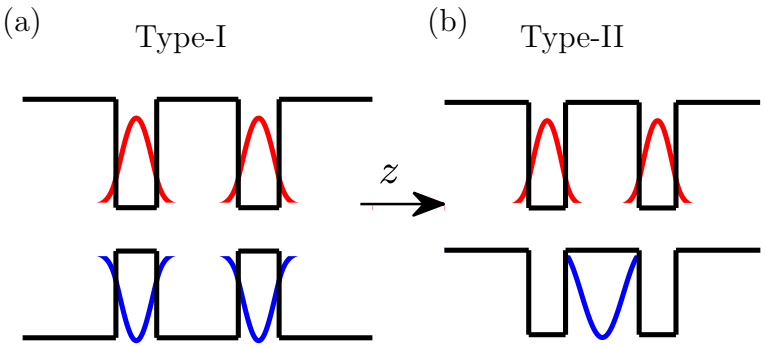

Figure 2.2: The conduction and valence band potential profiles of a (a) type-I and (b) type-II double-quantum-dot with electron (red) and hole (blue) wave functions schematically illustrated in both configurations.

schematically in Fig. 2.3 (a). The conduction and valence band potential profiles of this structure along the nanowire z axis are shown in Fig. 2.3 (b). The material parameters used in this thesis for InP are listed in Table 2.1. The electron is confined in the ZB region and the hole in the WZ region. This leads to indirect transitions between different crystal structures featuring a small emission intensity or brightness which is proportional to the overlap of the electron and the hole wavefunctions. This overlap is much smaller in the type-II configuration in comparison to that of the type-I configuration as it can also be observed by comparing of the electron and the hole overlap in Fig. 2.1 (a) and Fig. 2.1 (b). We overcome this weakness by designing a DQD structure in Chapter 3 and demonstrate that the structure has excellent properties in terms of the brightness. We also design quantum gates and show that quantum gating is much more efficient in these structures in comparison to the type-I structures.

2.2 Modeling of the quantum-dots

The electronic and optical properties are often calculated using different methods to try to capture the essential features. The theoretical frameworks typically used to calculate band structures or single-particle energies and wave functions of semiconductor QDs are [48]: the effective-mass single-band ap-

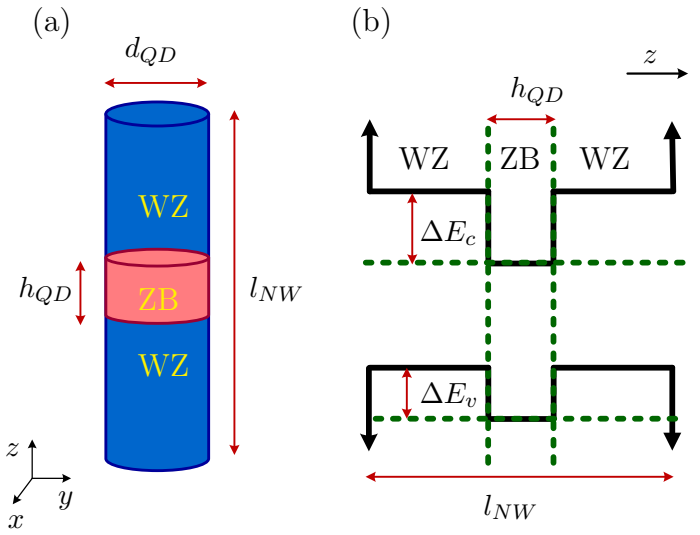

Figure 2.3: (a) A single-quantum-dot in a nanowire. (b) The conduction and valence band potential profiles along the nanowire z axis.

Parameters	value
electron mass m_e^*	$0.068\, m_0$
heavy-hole mass m_h^*	$0.64\, m_0$
ΔE_c	128.6 meV
ΔE_v	64.6 meV
ϵ	12.5
E_g of WZ crystalline phase	1.474 eV
E_g of ZB crystalline phase	1.410 eV
m_0 free electron mass	9.1×10^{-31} Kg

Table 2.1: InP crystal-phase QD material parameters [24].

proach, the **k**.**p** formalism, the empirical pseudopotential theory and the tight-binding theory [49], each of which being advantageous in certain respects. All methods generally predict similar qualitative features, however some persisting discrepancies include the number of confined levels and the energies of those levels for a particular QD morphology.

The effective-mass single-band theory is a very well established method to obtain the band structure in the case of weak perturbing inhomogeneous semiconductor potentials [50]. The basic idea behind the effective mass theory is actually rather simple: Near the band edges the electrons can be described

to behave as if they are in free space except their masses taking some effective value m^*. Therefore, in this method, the electron states are described by a single Schrödinger equation around the given point of the Brillouin zone, assuming the (conduction) band parabolic. The physical accuracy of this simple effective-mass approach decreases as one wanders away from the Γ point since the band non-parabolicity originating from band mixing, or inter-valley mixing, starts to be important.

In the framework of the effective-mass approach, this limitation was overcome by employing the model referred to as **k**.**p** theory [51, 52, 53]. It is based on selecting a few $3D$-periodic Bloch orbitals taken from the Brillouin zone center which single-particle wavefunctions are expanded in. The multiband **k**.**p** accounts for the proper structure of the valence band, including heavy, light and spin split-off hole bands. It is however limited to the top of the valence band, and it also does not account for the atomistic character of the interfaces between the dot and barrier material, and is expected to break down as the size of the nanostructure decreases.

The atomistic structure of the nanostructure is captured in either the tight-binding or pseudopotential approaches. Empirical tight-binding, as formulated in the 1980s [54], is a common method to calculate single-particle electronic properties of solids which is both accurate and efficient. Tight-binding models use atomistic scale wavefunctions but involve a large number of parameters which are determined using complicated fitting procedures [55] such as genetic algorithms [56, 57]. Pseudopotentials also require a large number of form factors and must rely on complex fitting procedures [58, 59]. The electronic structure calculation for different crystal polytypes is still an active field of research.

2.2.1 Our modeling method

In this thesis, we study the crystal-phase type-II QDs in a nanowire and design quantum devices based on them, so we need to perform geometrical parameter sweeps to analyze and optimize the device performance. For this reason, we prefer to use a less computationally demanding two-band effective-mass model where only the heavy-hole valence band and the conduction band

are included. Fortunately, under the conditions relevant for quantum-optics experiments, i.e., QDs with a large aspect ratio at low temperatures and small carrier populations, many features of QDs can be described remarkably well with this method [60, 61].

The relevant physical effects in crystal-phase QDs include the strain and piezoelectric effects as well as polarization fields in the wurtzite phase. However, it was shown by Faria Jr. et al. [62] using **k**.**p** method that the strain and polarization fields do not have strong influence on the optical properties of type-II InP crystal-phase QDs, and these effects were for this reason neglected in their later work [63]. Similarly, we exclude also these physical effects from the model to keep it as simple as possible for our device design purposes.

We use effective-mass and envelop function approximations in our model. In semiconductors, the electron or hole wave functions $\Psi_k(\boldsymbol{r})$ are Bloch states that are written as the product of a slowly-varying envelope function $\Phi_k(\boldsymbol{r})$, which matches the boundary conditions of the confining potential, and a periodic Bloch function $u_k(\boldsymbol{r})$ that captures the periodicity of the underlying atomic potential as [64]:

$$\Psi_k(\boldsymbol{r}) = u_k(\boldsymbol{r})\Phi_k(\boldsymbol{r}) \tag{2.1}$$

where $k \in e, h$ is a subscript denoting the electron or hole, respectively. This description of the localized states is known as the envelope function approximation. The key assumption here is that within a given energy band, the Bloch function is not a strong function of **k** (at least in the proximity of the band edge) and can thus be approximately represented by the band edge ($\mathbf{k} = 0$) Bloch function, $u(\mathbf{k}, \boldsymbol{r}) = u(\boldsymbol{r})$. The Bloch function $u(\boldsymbol{r})$ is a complex periodic function that satisfies Schrödinger's equation using the atomic-scale potential. Each energy band in the crystal has its own Bloch function. Fortunately, one never really needs to determine $u(\boldsymbol{r})$ precisely. Only the symmetry properties of these functions are necessary for most calculations. Thus, we can concentrate our attention on the envelope function $\Phi_k(\boldsymbol{r})$ which is a slowly varying function satisfying Schrödinger's equation using the macroscopic potential and an appropriate effective mass:

$$\hat{H}_k\Phi_k = \Big[\frac{\hat{p}_k^2}{2m_k^*} + V^k\Big]\Phi_k \tag{2.2}$$

where m_k^* is the effective mass that we assume to be constant in the whole system for the electron (hole); $\hat{p}_k$ is the three-dimensional momentum operator; the first term of Eq. (2.3) is the kinetic energy of the electron (hole); V^k is the QD confinement potentials for the electron (hole). In the following we show how to solve this equation for a QD in a nanowire.

Electron and hole single-particle states in a QD in a nanowire

In a QD in a nanowire as is shown in the Fig. 2.3 (a), the diameter of the dot is usually several times larger than its height then, the vertical confinement energies are almost one order of magnitude larger than the lateral confinement ones. For this reason, the confinement potential in cylindrical coordinate can be separated into the transverse (R, θ) plane and in the perpendicular z direction:.

$$V^k(\boldsymbol{r}) = V^k(R, \theta, z) = V_T^k(R, \theta) + V_{QW}^k(z) \tag{2.3}$$

where $V_{QW}^k(z)$ and $V_T^k(R, \theta)$ are the decoupled confinement potentials for the electron (hole) along the nanowire z axis and in the transverse plane, respectively. We approximate the transverse confinement potential by a hard wall potential:

$$V_T^k(R, \theta) = \begin{cases} 0 & R \leq d_{QD}/2 \\ \infty & R \geq d_{QD}/2 \end{cases} \tag{2.4}$$

It might also be assumed that the transverse confinement potential to be parabolic as:

$$V_T^k(R, \theta) = \frac{1}{2} m_k \omega_k^2 R^2 \tag{2.5}$$

here, ω_k is the in-plane parabolic potential for the electron (hole). Such parabolic lateral confinement is also known to mimic the most important features of various kinds of QDs and to give results in a good agreement with the experiment [65, 66].

The solutions of the non-interacting Hamiltonian (2.2) are, using the method of the separation of variables, separated wavefunctions in the z and in the transverse direction as:

$$\Phi(R, \theta, z) = \Phi_{QW}(z)\ \phi_T(R, \theta) \tag{2.6}$$

The wave function along the z axis $\phi_{QW}(z)$ with the potential $V^k_{QW}(z)$ being the single-well band structure shown in Fig. 2.3 (b), is a piecewise function defined differently in each region of the nanowire. For the electron in the conduction band of the type-II SQD nanowire, by considering the center of the coordinate system in the middle of the SQD along the z axis, $\phi_{QW}(z)$ becomes:

$$\phi_{QW}(z) = \begin{cases} Ae^{k_e z} & -l_{NW}/2 \leq z < -h_{QD}/2 \\ Be^{-il_e z} + Ce^{il_e z} & -h_{QD}/2 \leq z \leq h_{QD}/2 \\ De^{-k_e z} & h_{QD}/2 < z \leq l_{NW}/2 \end{cases} \tag{2.7}$$

where $l_e = \sqrt{2m^*_e E_{ze}}/\hbar$, $k_e = \sqrt{2m^*_e(\Delta E_c - E_{ze})}/\hbar$ and E_{ze} is the electron energy because of the confinement along the z axis. The constants A, B, C and D are calculated from the boundary conditions. In Appendix A, we explain how to implement these boundary conditions. The electron ground-state in the conduction band of a type-II SQD nanowire $\phi^1_{QW}(z)$ is shown in Fig. 2.4. This eigenstate is the only confined state in the z direction in this configuration. While Schrödinger equation for the electron in the z direction in the conduction band has only one solution, there are many solutions for holes in the valence band of the type-II SQD nanowire in the form of:

$$\phi_{QW}(z) = \begin{cases} Ae^{-il_h z} + Be^{il_h z} & -l_{NW}/2 \leq z < -h_{QD}/2 \\ Ce^{-k_h z} + De^{k_h z} & -h_{QD}/2 \leq z \leq h_{QD}/2 \\ Ee^{-il_h z} + Fe^{il_h z} & h_{QD}/2 < z \leq l_{NW}/2 \end{cases} \tag{2.8}$$

where $l_l = \sqrt{2m^*_h E_{zh}}/\hbar$, $k_h = \sqrt{2m^*_h(\Delta E_v - E_{zh})}/\hbar$ and E_{zh} is the hole energy because of the confinement along the z axis. The constants A, B, C, D, E and F are calculated from the boundary conditions which we explain in the Appendix A. The twelve lowest energy eigenstates are shown in the Fig. 2.5. As it can be seen in this figure, unlike the electron state which was confined inside the QD, the hole states are not confined inside the QD and the wavefunctions are spread all over the nanowire outside of the QD.

The transverse part of the wavefunction $\phi_T(R, \theta)$ by considering the parabolic confinement (2.5) becomes the Fock-Darwin state with the analytical expres-

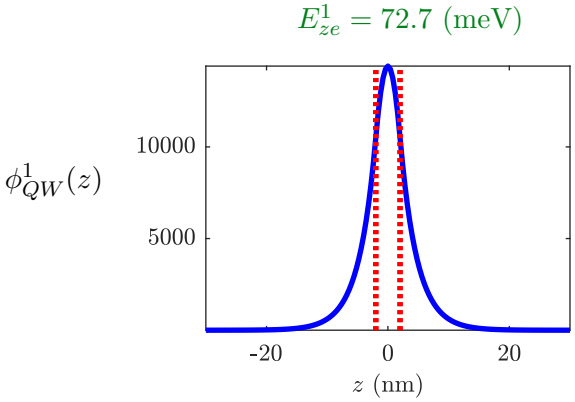

Figure 2.4: Normalized ground-state electron wavefunction $\phi^1_{QW}(z)$ in the z direction in the conduction band of an InP crystal-phase SQD in a nanowire. The geometrical parameters of the structure are: $h_{QD} = 4$ nm, $l_{NW} = 60$ nm.

sion for the wavefunction:

$$\phi^{lm}_T(R,\theta) = R^{|m|}e^{\left(\frac{-R^2}{2}\right)}\mathcal{L}^{|m|}_l(R^2)e^{im\theta} \tag{2.9}$$

where $\mathcal{L}$ is the Laguerre polynomial. $l = 0, 1, ..$ and $m = 0, \pm 1, ...$ are the quantum numbers which come up in the solution of the Schrödinger equation in the transverse direction. The single-particle energy in the transverse direction is:

$$E_T = (2l + |m| + 1)\hbar\omega_k \tag{2.10}$$

The ten lowest-energy transverse eigenstates of an electron in a SQD nanowire are shown in the Fig. 2.6.

By considering an infinite potential well in the transverse direction as in Eq. (2.4), the solution is given by the Bessel functions:

$$\phi^{lm}_T(R,\theta) = J_m(\lambda_l R)e^{im\theta} \tag{2.11}$$

and the energy of the single-particle electron or hole states is calculated as:

$$E_T = \frac{\hbar^2\lambda^2}{2m^*_k} \tag{2.12}$$

here λ is calculated from the boundary condition where the transverse eigenstate in (2.11) need to be zero at the nanowire boundary: $J_m(\lambda_l d_{QD}/2) = 0$. The transverse solution in Eq. (2.11) is expected to be a closesr resemblance

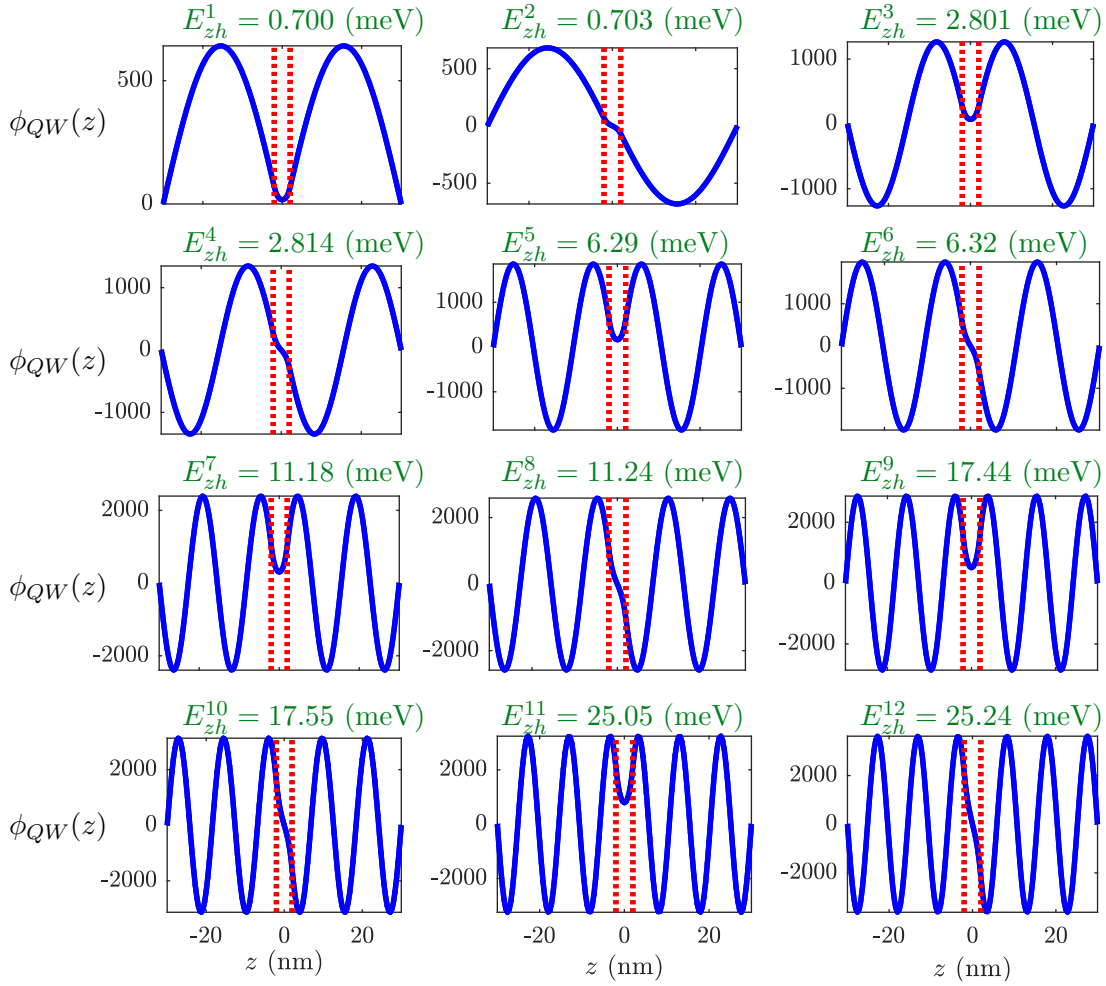

Figure 2.5: Lowest-energy normalized single-particle hole wavefunctions in the z direction $\phi_{QW}(z)$ in the valence band of an InP crystal-phase type-II SQD in a nanowire. The geometrical parameters of the structure are: $h_{QD} = 4$ nm, $l_{NW} = 60$ nm.

with the real wavefunctions in nanowires in comparison to the solution in Eq. (2.9), since for nanowires we suspect the potential to be flat throughout the transverse part of the nanowire as in Eq. (2.4). The ten lowest energy transverse eigenstates are shown in the Fig. 2.7. The details of the single-particle Schrödinger equation calculation is carried out in the Appendix A.

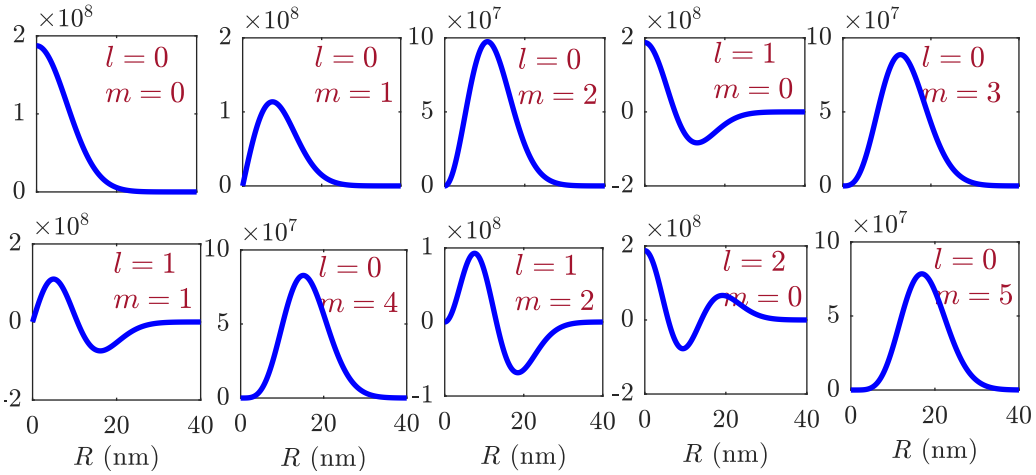

Figure 2.6: Lowest-energy normalized transverse wavefunctions $\phi_R^{ml}(R)$ of the single-particle electron in a type-I GaAs/AlGaAs SQD in a nanowire with geometrical parameters of $d_{QD} = 80$ nm, $h_{QD} = 4$ nm, $l_{NW} = 100$ nm. By considering $\hbar\omega_e = 20$ meV, the corresponding energies in the transverse direction are calculated as: $E_T = 20, 40, 60, 60, 80, 80, 100, 100, 100, 120$ meV.

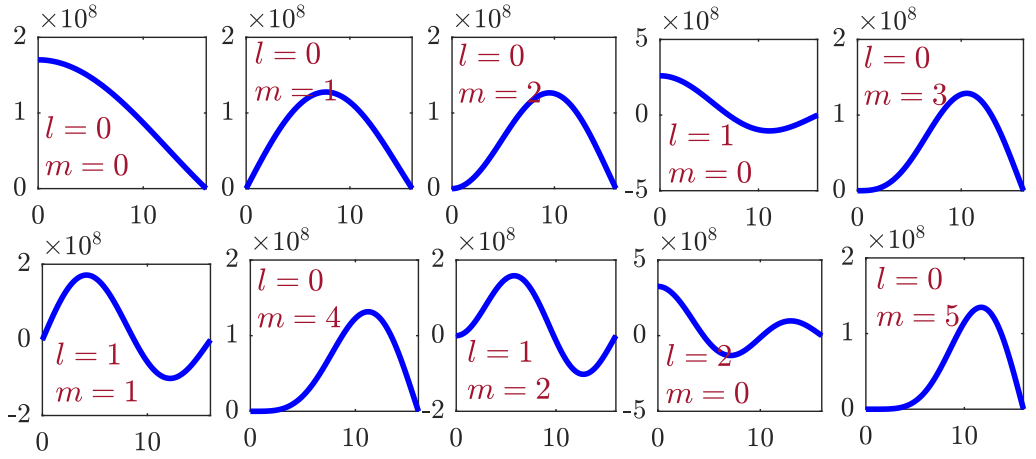

Figure 2.7: Lowest-energy normalized transverse wavefunctions $\phi_R^{ml}(R)$ of the single-particle electron in a crystal-phase InP SQD in a nanowire with geometrical parameters of $d_{QD} = 32$ nm, $h_{QD} = 4$ nm, $l_{NW} = 60$ nm. The corresponding transverse energies are calculated as: $E_T = 12.68, 32.21, 57.86, 66.85, 89.30, 107.97, 126.32, 155.43, 164.29, 168.77$ meV.

2.3 Modeling the exciton state

In the previous section, a single-particle model of the QD has been described. Two kinds of non-interacting particles are considered: electrons and heavy-holes, distinguished by their opposing charges and differing masses. In order to describe the system realistically, however, the strong Coulomb interaction among and between the species must be taken into account. An electron-hole pair attracted to each other by Coulomb interaction form a bound-state which is called an *exciton*. In type-II QDs where the single-particle hole is not confined inside the QD and instead it is spread all over the nanowire outside of the QD [cf. Fig. 2.5], the Coulomb interaction effect becomes significantly important since it is the only confining potential which make the hole bound to the electron. For this reason, we need to develop a method capable of describing a system of interacting particles with a sufficient accuracy.

The Hamiltonian of a system consisting of an interacting electron and hole can be written as:

$$\hat{H} = \hat{H}_h + \hat{H}_e + \hat{H}_C \tag{2.13}$$

here, $\hat{H}_{e/h}$ is the single-particle Hamiltonian for the electron/hole in Eq. (2.2) which we explained how to solve it in the previous section and $\hat{H}_C$ is the Coulomb interaction between the electron and hole. In working with a system of interacting particles, it is much more convenient to use the second quantization representation. Its a method for representing wave functions and operators in a compact and convenient way in comparison to the rather cumbersome task of constructing linear combination of all possible many-particle Slater determinants. The Coulomb operator in the second quantization representation is written as [67]:

$$\hat{H}_C = \frac{1}{2}\sum_{\sigma\sigma'}\int\int d\boldsymbol{r}\, d\boldsymbol{r}'\, \hat{\psi}^\dagger_\sigma(\boldsymbol{r})\hat{\psi}^\dagger_{\sigma'}(\boldsymbol{r}')\frac{q_1 q_2}{4\pi\epsilon|\boldsymbol{r}-\boldsymbol{r}'|}\hat{\psi}_{\sigma'}(\boldsymbol{r}')\hat{\psi}_\sigma(\boldsymbol{r}) \tag{2.14}$$

here $\hat{\psi}^\dagger_\sigma(\boldsymbol{r})$ and $\hat{\psi}_\sigma(\boldsymbol{r})$ are field operators that respectively create and annihilate a particle of the spin σ at the position $\boldsymbol{r} : (R, \theta, z)$. The anti-symmetry of the

exciton state is guaranteed by the fermionic anti-commutation rules:

$$\{\hat{\psi}_\sigma(\boldsymbol{r}), \hat{\psi}^\dagger_{\sigma'}(\boldsymbol{r}')\} = \delta_{\sigma\sigma'}\delta(\boldsymbol{r}-\boldsymbol{r}') \qquad \{\hat{\psi}_\sigma(\boldsymbol{r}), \hat{\psi}_{\sigma'}(\boldsymbol{r}')\} = \{\hat{\psi}^\dagger_\sigma(\boldsymbol{r}), \hat{\psi}^\dagger_{\sigma'}(\boldsymbol{r}')\} = 0 \tag{2.15}$$

where $\{A, B\} = AB + BA$. The field operators maybe expanded in terms of a set of single-particle wavefunctions $\Phi_i(\boldsymbol{r})$ independent of the spin:

$$\psi^\dagger_\sigma(\boldsymbol{r}) = \sum_i \Phi^*_i(\boldsymbol{r}) C^\dagger_{i\sigma}, \quad \psi_\sigma(\boldsymbol{r}) = \sum_i \Phi_i(\boldsymbol{r}) C_{i\sigma} \tag{2.16}$$

here, $C^\dagger_{i\sigma}(C_{i\sigma})$ is either an operator on the electron or the hole subspace creating (annihilating) an electron or a hole in the single-particle state i with spin σ whose wavefunction is $\Phi_i(\boldsymbol{r})$. Even though $\Phi_i(\boldsymbol{r})$'s are independent of the spin but the expansion (2.16) is exact since $\Phi_i(\boldsymbol{r})$s span the single-particle Hilbert space, i.e. they form a complete set. Inserting the expansion (2.16) into (2.14) yields:

$$\hat{H}_C = \frac{1}{2}\sum_{ijkl}\sum_{\sigma\sigma'} \underbrace{\int\int d\boldsymbol{r}\, d\boldsymbol{r}' \Phi^*_i(\boldsymbol{r})\Phi^*_j(\boldsymbol{r}') \frac{q_1 q_2}{4\pi\epsilon|\boldsymbol{r}-\boldsymbol{r}'|} \Phi_k(\boldsymbol{r}')\Phi_l(\boldsymbol{r})}_{V_{ij,kl}} C^\dagger_{i\sigma}\, C^\dagger_{j\sigma'}\, C_{k\sigma'}\, C_{l\sigma} \tag{2.17}$$

or:

$$H_C = \frac{1}{2}\sum_{ijkl}\sum_{\sigma\sigma'} V_{ij,kl}\, C^\dagger_{i\sigma}\, C^\dagger_{j\sigma'}\, C_{k\sigma'}\, C_{l\sigma} \tag{2.18}$$

Here, $V_{ij,kl}$ is called the Coulomb matrix element (CME) between particles in the states i, j, k and l. Depending on the operator sequence two categories of the Coulomb matrix elements can be identified [68]:

1- Electron-hole *direct interaction* elements: $C^\dagger_{i\sigma}C^\dagger_{j\sigma'}C_{k\sigma'}C_{l\sigma} = C^{e\dagger}_{i\sigma}C^{h\dagger}_{j\sigma'}C^h_{k\sigma'}C^e_{l\sigma}$ or $C^{h\dagger}_{i\sigma}\, C^{e\dagger}_{j\sigma'}\, C^e_{k\sigma'}\, C^h_{l\sigma}$.

2- Electron-hole *exchange interaction* elements: $C^\dagger_{i\sigma}C^\dagger_{j\sigma'}C_{k\sigma'}C_{l\sigma} = C^{e\dagger}_{i\sigma}C^{h\dagger}_{j\sigma'}C^e_{k\sigma'}C^h_{l\sigma}$ or $C^{h\dagger}_{i\sigma}\, C^{e\dagger}_{j\sigma'}\, C^h_{k\sigma'}\, C^e_{l\sigma}$.

The first category describes the direct attraction of the electron and the hole, where for example an electron in the state k and a hole in the state l are annihilated and an electron in the state i and a hole in the state j are created. The second category corresponds to the process of the electron and the hole exchanging their status during the interaction. This interaction process occurs because of the undistingushibality due to the quantum nature of these

particles. Although the electron and the hole can be distinguished by their respective masses, these processes occur and therefore the matrix elements exist. Usually these interactions are neglected because they have considerably smaller amplitude in comparison to the direct terms. These matrix elements are partly responsible for the excitonic fine-structure splitting. Refs. [69] and [70] showed the electron-hole exchange interaction of type-I InGaAs/GaAs QDs is enhanced with respect to its bulk value because of the confinement-induced increased overlap of the electron and the hole wavefunctions; Ref. [71] has reported an exciton exchange-interaction of 200 μeV as compared to the 20 μeV of bulk GaAs value, i.e., an enhancement by a factor of ten [70]. In type-II QDs, confinement reduces the exchange interaction [72, 73] since the overlap of the electron and the hole wavefunctions decreases in these structures in comparison to the bulk one. For this reason, we neglect the exchange interaction in our calculations in this thesis.

2.3.1 Configuration-interaction method

The configuration-interaction method is a way to find approximate solutions of the Schrödinger equation for a system with interacting particles. The name configuration-interaction is the one most commonly used in the field of quantum chemistry, see e.g. reference [74]. In condensed matter physics, one more often uses the name *exact diagonalization*, which may be misleading since the obtained solution is always a numerical approximation. Nuclear physicists typically use the name *shell model calculations*, or *no-core shell model calculations* [75].

In configuration-interaction method, the exciton wavefunction -a priori unknown wavefunction- is expanded as a linear combination of several many-particle basis states (configurations), and the states are then allowed to mix (interact) with each other to minimize the energy. In theory, the method provides solutions to the Schröodinger equation to an arbitrary numerical precision. In practice, however, the numerical complexity limits the usage to systems with very few particles. Even if the capabilities of our computers continue to increase at a similar rate to that of the last decades, the configuration-interaction method will most likely not become an all-purpose

method for quantum many-particle physics. But it has some advantages compared to other methods. It is very general, as it is applicable for both fermions and bosons and is not limited to a single type of interaction. It gives both the ground-state as well as the excited-states. It typically also makes it possible to obtain an estimate of the associated numerical error. For a chosen basis space, the actual ground-state within that space is obtained. This is in sharp contrast to many variational procedures for energy minimization, which may be hindered by the presence of a local minima in the energy functional.

There are several other quantum many-particle methods; for example the so-called coupled-cluster method may allow for the treatment of larger particle numbers. Recent studies have applied this method to e.g. QD systems [76] and trapped bosonic gases [77], demonstrating that the coupled-cluster method can be a powerful alternative to the configuration-interaction method, at least for the considered systems. Quantum Monte Carlo methods may treat much larger particle numbers (see e.g. references [78, 79]). However, a disadvantage is that they in general do not give excited states of a system.

We use configuration-interaction method to calculate the exciton states in this thesis. In Chapter 3, we present the calculation results and also the convergence study of the configuration-interaction calculations to examine the exciton state in type-II crystal-phase QDs in nanowires.

2.4 Stimulated Raman adiabatic passage (STIRAP)

In our scheme for quantum computing, we use the spin of an electron in a QD as a qubit. For manipulating the spin qubits, we use the all-optical STIRAP technique. STIRAP is an efficient method for transferring population adiabatically between two discrete quantum states by coupling them using two radiation fields via an intermediate state which is usually a radiatively decaying state [80, 81]. The use of two lasers coupling three states, rather than a single laser coupling two states, offers many advantages: the excitation efficiency can be made relatively insensitive to many of the experimental details of the pulses such as the laser intensity, the pulse timing and the pulse

shape. In addition, with the three-state system, one can produce excitation between states of the same parity, for which single-photon transitions are forbidden. These features have made STIRAP a popular tool in optical quantum information processing [82, 83, 84, 85].

In this section, we present the basic of the STIRAP process and the equations that govern the time dependence of the probability amplitudes used in the mathematical description of the STIRAP process. Further details of the STIRAP process which are important in designing quantum gates are also discussed.

2.4.1 STIRAP theory

The STIRAP scheme involves a three-state, two-photon Raman process, in which an interaction with a pump pulse P links the initial state $|1\rangle$ with an intermediate state $|e\rangle$, which in turn interacts via a Stokes pulse S with a final, target state $|2\rangle$. Figure 2.8 illustrates the connections. Typically the states $|1\rangle$ and $|2\rangle$ are metastable states of a quantum system such that their lifetimes is long in comparison to the length of the laser pulse. On the other hand, the intermediate state will undergo spontaneous emissions not only to the states $|1\rangle$ and $|2\rangle$, but also to other states. The objective is to transfer all of the population from the state $|1\rangle$ into the state $|2\rangle$, losing none by spontaneous emission from the state $|e\rangle$. At the first glance, the possibility of radiative decay from the intermediate level to states other than the desired final state seems to be detrimental to the implementation of an efficient transfer to a single quantum state. However, as we shall see, the STIRAP process has the remarkable property of placing almost no population into the intermediate state $|e\rangle$, and thus it is insensitive to any possible decay from that state.

The instantaneous Hamiltonian of the Λ three-state system shown in Fig. 2.8, in the Rotating Wave Approximation (RWA) [37, 38] is written in the $|1\rangle, |e\rangle, |2\rangle$ basis as:

$$\mathrm{H}(t) = \frac{\hbar}{2}\begin{bmatrix} 0 & \Omega_P(t)e^{i\psi_P} & 0 \\ \Omega_P(t)^* e^{i\psi_P} & 2\Delta_P & \Omega_S(t)e^{i\psi_S} \\ 0 & \Omega_S(t)^* e^{i\psi_S} & 2(\Delta_P - \Delta_S) \end{bmatrix} \tag{2.19}$$

The details of this derivation is presented in Appendix B. Here, the Rabi frequencies $\Omega_S(t)$ and $\Omega_P(t)$ describe the coupling strength between the states

which are defined as:

$$\Omega_P(t) = d_P\mathcal{E}_P(t)/\hbar\,, \quad \Omega_S(t) = d_S\mathcal{E}_S(t)/\hbar \tag{2.20}$$

d_P and d_S are respectively the $|1\rangle - |e\rangle$ and $|2\rangle - |e\rangle$ transitions' dipole moment. $\mathcal{E}_P(t)$ and $\mathcal{E}_S(t)$ are respectively the electric field amplitudes of the Stokes and pump lasers at a fixed point. The diagonal elements of Eq. (2.19): Δ_P is the detuning of the pump laser from the $|1\rangle$-$|e\rangle$ transition such that $\hbar\Delta_P = E_e - E_1 - \hbar\omega_P$ and $\hbar\Delta_S$ is the detuning of the Stokes laser from the $|e\rangle$-$|2\rangle$ transition such that $\hbar\Delta_S = E_e - E_2 - \hbar\omega_S$. We define the single-photon detuning as $\Delta \equiv \Delta_P$ and the two-photon detuning as $\delta \equiv \Delta_P - \Delta_S$. With these definitions of the Δ and δ, the equivalent three-level Λ system is shown in Fig. 2.8 (b).

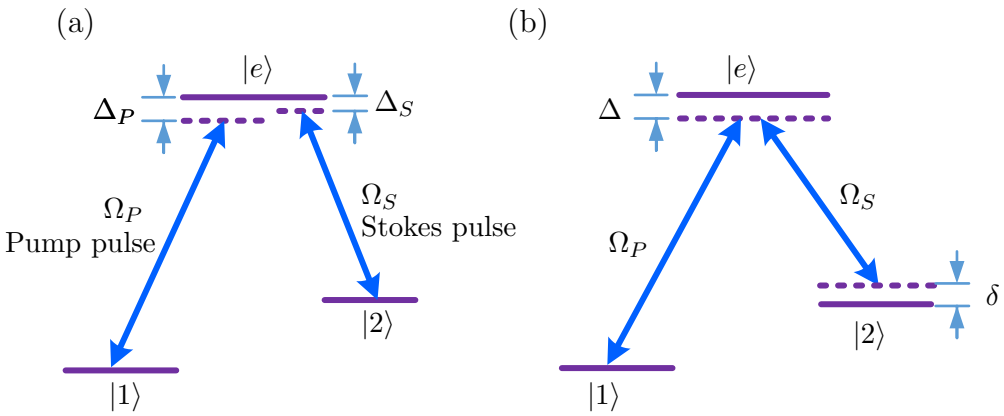

Figure 2.8: (a) STIRAP scheme in a three-level Λ system. (b) The scheme is equivalent to (a) by defining the single-photon detuning $\Delta = \Delta_P$ and two-photon detuning $\delta = \Delta_P - \Delta_S$.

The principal observables of a multistate quantum system, e.g. the three-level Λ system; are the probabilities $P_n(t)$ that the system be found in the state n at time t. These probabilities, known also as populations, are expressible as the absolute squares of the complex-valued probability amplitudes $C_n(t)$:

$$P_n(t) = |C_n(t)|^2 \tag{2.21}$$

Probability amplitudes $C_n(t)$ are calculated from the time dependent Schrödinger

equation:

$$\frac{d}{dt}\mathrm{C}(t) = -\frac{i}{\hbar}\mathrm{H}(t)\mathrm{C}(t) \tag{2.22}$$

where $\mathrm{C}(t)$ is a vector of time-dependent probability amplitudes $C_1(t)$, $C_2(t)$, and $C_3(t)$. In transferring population from $|1\rangle$ to $|2\rangle$, the population transfer efficiency at the end of the process is defined as:

$$TE = \frac{P_2(t)}{P_1(t)}\Big|_{t=t_{end}} \tag{2.23}$$

For transferring the population, first the Stokes laser couples the two empty states $|e\rangle$ and $|2\rangle$ and thus it does not change the population of the state $|1\rangle$. However, this does not mean that the Stokes laser has no effect. In fact, this laser creates a coherent superposition of the two initially unpopulated states $|e\rangle$ and $|2\rangle$. When this coherent superposition state is subsequently coupled to the populated state $|1\rangle$ by the pump laser, a so-called dark state is formed - a state from which the pump laser cannot transfer population to the radiatively decaying intermediate state. Rather, the population is directly channeled into state $|2\rangle$, as the following discussion and the equations reveal.

Diagonalising $\mathrm{H}(t)$ in (2.19) analytically is not straight forward. Here for showing analytical solution, we will only consider two-photon resonance $\delta = \Delta_P - \Delta_S = 0$. In this case we find eigenvalues as:

$$\begin{aligned} \left|a^+\right\rangle &= \sin(\Theta)\sin(\Phi)\,|1\rangle + \cos(\Phi)\,|e\rangle + \cos(\Theta)\sin(\Phi)\,|2\rangle \\ \left|a^0\right\rangle &= \cos(\Theta)\,|1\rangle - \sin(\Theta)\,|2\rangle \\ \left|a^-\right\rangle &= \sin(\Theta)\cos(\Phi)\,|1\rangle - \sin(\Phi)\,|e\rangle + \cos(\Theta)\cos(\Phi)\,|2\rangle \end{aligned} \tag{2.24}$$

where the (time-varying) mixing angle Θ is defined by the relationship

$$\tan(\Theta) = \frac{\Omega_P(t)}{\Omega_S(t)} \tag{2.25}$$

and the angle Φ is a function of the Rabi frequencies and the single photon detuning:

$$\tan(2\Phi) = \frac{\sqrt{\Omega_P^2 + \Omega_S^2}}{\Delta} \tag{2.26}$$

The adiabatic energies corresponding to these eigenstates, the eigenvalues of the Hamiltonian (2.19) are:

$$\begin{aligned} \omega^{\pm} &= \Delta_P \pm \sqrt{\Delta_P^2 + \Omega_P^2 + \Omega_S^2} \\ \omega^0 &= 0 \end{aligned} \tag{2.27}$$

The objective is to control the system state vector $|\Psi\rangle$ thereby controlling the distribution of the population among the three states. At very early times, $|\Psi\rangle$ will be identical to $|1\rangle$. At very late times, we require that $|\Psi\rangle$ be parallel to $|2\rangle$. We wish to avoid even transient placement of the population into $|e\rangle$, which will radiatively decay to other states that are not connected by the coherent radiation fields.

The eigenstates $|a^+\rangle$ and $|a^+\rangle$ are represented by a linear combination of all three bare states. They include, in particular, a component of the bare state $|e\rangle$, which is the leaky state. We therefore wish to avoid population in either of these two dressed states, whether produced directly or by nonadiabatic coupling during the process. The state $\left|a^0\right\rangle$ is, at all times, free of any contribution from the leaky state $|e\rangle$, thus it will be the appropriate vehicle for transferring population from state $|1\rangle$ to state $|2\rangle$ without populating state $|e\rangle$. The mixing angle Θ can be experimentally controlled through the ratio of the Rabi frequencies.

If the Stokes laser precedes the pump laser, as shown in Fig. 2.9, we identify three distinctly different intervals I, II, and III. The lasers' envelopes are considered to be Gaussian shaped as:

$$\begin{aligned} \mathcal{E}_P(t) &= A_P e^{-\frac{t^2}{2\tau^2}} \\ \mathcal{E}_S(t) &= A_S e^{-\frac{(t+\Delta T)^2}{2\tau^2}} \end{aligned} \tag{2.28}$$

with the pulses width of τ. The maxima of the $\mathcal{E}_P(t)$ and $\mathcal{E}_S(t)$ are separated by ΔT in time. In region I, only the Stokes laser is present; the Rabi frequency due to the pump laser is zero, i.e., the mixing angle Θ is zero. Therefore, as the system is only exposed to the Stokes laser, the state $\left|a^0\right\rangle$ is identical to the state $|1\rangle$ as well as to the state vector $|\Psi\rangle$. Thus as is shown in Fig. 2.10, in region I, three vectors are aligned: the vector representing the bare state $|1\rangle$, the vector $\left|a^0\right\rangle$ of the strongly coupled system, and the state vector $|\Psi\rangle$.

In the interval II, as is shown in Fig. 2.9 (a), the Stokes laser Rabi frequency is smoothly reduced while the pump laser Rabi frequency increases to its maximum value, changing the mixing angle smoothly from 0° to 90°. As shown in Fig. 2.10, the vector $\left|a^0\right\rangle$ is rotated into a position parallel to the bare state $|2\rangle$ in a plane perpendicular to the bare state $|e\rangle$. Therefore, during this motion, the vector never acquires a component of the leaky state $|2\rangle$. The

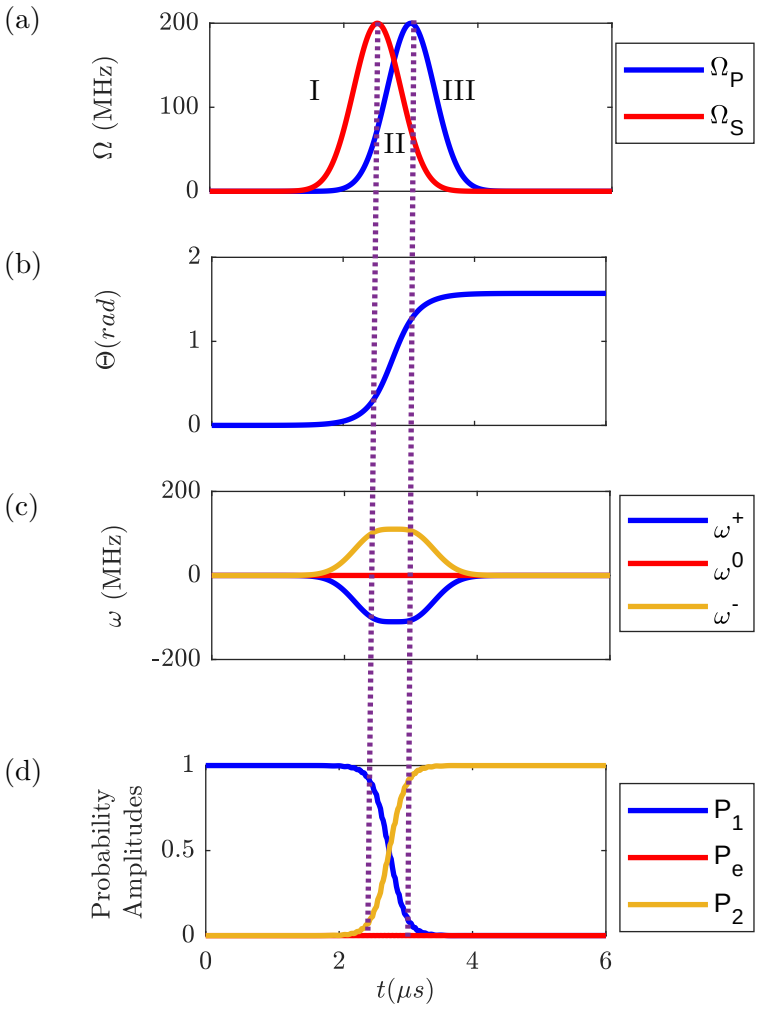

Figure 2.9: Time evolution of (a) the Rabi frequencies of the pump and the Stokes laser [see Fig. 2.8]; (b) the mixing angle [see Fig. 2.10]; (c) the dressed-state eigenvalues [see Eq. (2.27)]; and (d) the population of the initial level (starting at unity) and the final level (reaching unity). In this calculation $d_P = d_S = 1$ is been considered.

crucial question is whether or not the coupling of the states by the radiation fields is strong enough that the flow of population (or the state vector $|\Psi\rangle$) follows the motion of the vector $|a^0\rangle$ adiabatically. The STIRAP process authenticity condition is addressed later in this section. The evolution of the system can also bee understood by looking at the dressed-state eigenvalues [see Fig. 2.9 (c)]. At very early times, when both Rabi frequencies are zero,

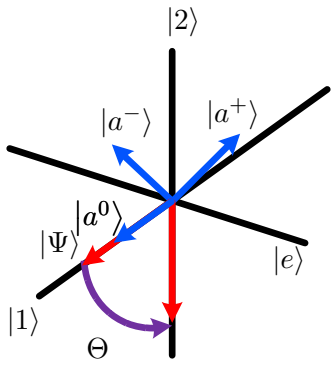

Figure 2.10: Graphic representation of the Hilbert space for the three-level system in the basis of the bare states $|1\rangle, |e\rangle, |2\rangle$ and in the basis of the dressed states $|a^0\rangle$,$|a^+\rangle$, and $|a^-\rangle$. Since the population is initially in state $|1\rangle$, the state vector $|\Psi\rangle$ is also aligned parallel to $|1\rangle$. At later times, the components of the state vector $|\Psi\rangle$ along the three dressed or bare states give the population in these states.

all three eigenvalues are degenerate. During interval I, the Stokes laser couples states $|e\rangle$ and $|2\rangle$ while state $|1\rangle$ is not involved in the interaction. At this time, therefore, the splitting of the eigenvalues is due to the coupling of states $|e\rangle$ and $|2\rangle$ alone. The eigenvalue that remains unchanged is associated with $|a^0\rangle$ (which is identical to state $|1\rangle$ at this early time). The vector $|a^0\rangle$ still remains in its original position [cf. Fig. 2.10], but the degeneracy with the eigenvalues of states $|a^+\rangle$ and $|a^-\rangle$ is lifted. During interval II, the splitting of the eigenvalues ω^+,ω^-, and ω^0 is largest, i.e. the coupling is strongest and both radiation fields contribute to it, as the vector moves from its position parallel to state $|1\rangle$ into the position parallel to state $|2\rangle$. This motion results in a complete population transfer if the state vector $|\Psi\rangle$ evolves adiabatically. If the coupling is insufficient (i.e., if the Rabi frequencies are too small), the motion of the state vector $|\Psi\rangle$ will lag behind the motion of the dressed states; it will precess around $|a^0\rangle$. It is qualitatively obvious that the state vector then acquires a component along $|a^+\rangle$ or $|a^-\rangle$ (by nonadiabatic coupling). This implies that some population reaches the leaky state $|e\rangle$ and the transfer process will be incomplete.

Here, we neglected the spontaneous emission from the decaying state $|e\rangle$

out of the system in our calculations. The description of this process requires equations for the density matrix [86, 87]. Radiative decay is important because it serves as a leak responsible for the loss of the population from the three-level system. The population lost by the spontaneous emission might reach states that one wishes would remain unpopulated. The consequence of spontaneous emission within the Λ system, from state $|e\rangle$ to states $|1\rangle$ and $|2\rangle$, was studied in [88, 89]. For small-to-moderate decay rates STIRAP is not significantly affected by spontaneous emission because the middle state is unpopulated. For strong decay rates, STIRAP degenerates into incoherent optical pumping. Ref. [90] studied this problem by using an effective Hamiltonian derived from a microscopic model.

2.4.2 Condition for the adiabatic following

As was pointed out in the previous section, insufficient coupling by the coherent radiation fields may prevent the state vector $|\Psi\rangle$ from adiabatically following the evolution of the trapped state $\left|a^0\right\rangle$, and the loss of the population due to the nonadiabatic transfer to the states $|a^+\rangle$ and $|a^-\rangle$ may occur. The condition for adiabatic following can be derived from general considerations in quantum mechanics which need to be invoked whenever the Hamiltonian is explicitly time dependent. The Hamiltonian matrix element for nonadiabatic coupling between state $\left|a^0\right\rangle$ which carries the population and evolves in time, and either one of the states $|a^+\rangle$ or $|a^-\rangle$ is given by $\langle a^{\pm}|\dot{a}^0\rangle$. Nonadiabatic coupling is small if this matrix element is small compared to the field induced splitting $|\omega^{\pm} - \omega^0|$ of the energies of these states, i.e.,

$$\langle a^{\pm}|\dot{a}^0\rangle \ll |\omega^{\pm} - \omega^0| \tag{2.29}$$

Using Eqs. (2.24)-(2.27) we find $\langle a^{\pm}|\dot{a}^0\rangle = -\dot{\Theta}\sin\Phi$, and therefore the adiabaticity constraint, by considering $\sin\Phi = 1$, reads

$$\dot{\Theta} \ll |\omega^{\pm} - \omega^0| \tag{2.30}$$

It is straightforward to show that Eq. (2.30) can be written in the form [91]:

$$|\omega^{\pm} - \omega^0| = \Omega_{rms}(t) \gg |\dot{\Theta}(t)| = \frac{\Omega_S(t)\dot{\Omega}_P(t) - \Omega_P(t)\dot{\Omega}_S(t)}{\Omega_P(t)^2 + \Omega_S(t)^2} \tag{2.31}$$

where $\Omega_{rms} = \sqrt{\Omega_P^2 + \Omega_S^2}$. This condition quantifies the smoothness required for the pulses: the relationship must hold at any time during the transfer process (hence a *local* condition). When the adiabatic condition is fulfilled, the completeness of STIRAP is insensitive to small variations of the laser intensity, the duration, and the delay of the pulses as well as to variations in the transition dipole moments.

A useful *global* condition is derived by integrating Eq. (2.31) over the interaction duration which we denote by T. The integral of the rms Rabi frequency is the rms pulse area

$$\mathcal{A} = \int_T \Omega_{rms}(t)dt = \int_T \sqrt{\Omega_P^2 + \Omega_S^2}\, dt \tag{2.32}$$

and because the integral over $\dot{\Theta}(t)$ produces the value $\pi/2$, the inequality (2.31) reduces to

$$\mathcal{A} \gg \pi/2 \tag{2.33}$$

Because the integral in (2.32) is proportional to the peak Rabi frequency Ω_{max} (assuming, for simplicity, it is the same for both pulses) and the pulses' overlap time T, Eq. (2.33) demands that the intensities and the pulses' overlap time must be large enough. We can write Eq. (2.33) as

$$\Omega_{max} T > \mathcal{A}_{min} \tag{2.34}$$

where $\mathcal{A}_{min}$ is some minimum pulse area, dependent on the pulse shape and the required population transfer efficiency TE. By considering minimum 95% efficiency, usually, pulse areas of $\mathcal{A}_{min} \geq 3\pi$ have sufficed to provide efficient population transfer. Obviously, the global condition (2.34) is simpler to evaluate (and less restrictive) than the local condition (2.31). For smooth pulses the global condition (2.34) usually also guarantees the fulfillment of the local condition.

2.4.3 Further aspects of the three-level STIRAP

This section examines the basic properties, requirements, and restrictions for STIRAP.

Optimal pulse delay and width

The pulse delay ΔT between the P and S pulses affects the efficiency of STIRAP through (i) the adiabatic condition, and (ii) the completeness of the projection of the state vector $|\Psi(t)\rangle$ onto the dark state $\left|a^0\right\rangle$ at the initial and final times t_i and t_f. The optimum delay is determined by the following arguments.

Coincident pulses: In this case, and for identical pulse shapes, the mixing angle Θ is constant; then the nonadiabatic coupling vanishes ($\dot{\Theta} = 0$) and the evolution is perfectly adiabatic according to (2.31). However, the state vector $\Psi(t)$ is not initially aligned with the dark state $a^0(t)$, but instead $\Psi(t) = [a^0(t) + a^-(t)]/\sqrt{2}$, and a similar relation applies at the end time t_f. The interference between different evolution paths $a^0(t)$ and $a^-(t)$ from the state $|1\rangle$ to the state $|2\rangle$ leads to oscillations in the final population of the state $|2\rangle$ instead of complete population transfer as shown in Fig. 2.11 (a).

Small delay, very large overlap: For small delay, the overlap is large and the mixing angle $\Theta(t)$ is nearly constant during most of the overlap $\Theta(t) = \Theta$; hence $\dot{\Theta}(t) = 0$ and adiabaticity is good there. However, due to the small delay, $\Theta(t)$ rises too quickly from 0 to about Θ_0 before the overlap, and then again from about Θ_0 to $\pi/2$ after the overlap. These rapid rises generate large nonadiabatic couplings $\dot{\Theta}(t)$ at early and late times, which cause nonadiabatic transitions from the dark state to the other two adiabatic states. These two nonadiabatic zones lead again to interference and oscillations in P_2 as it can be observed in Fig. 2.11 (b).

Large delay, very small overlap: The initial state vector is $\Psi(t_i) = a^0(t_i)$. Because for most of the time only one pulse is present, the mixing angle $\Theta(t)$ stays nearly constant for most of the excitation: $\Theta(t) \approx 0$ early and $\Theta(t) = \pi/2$ late as we can see in the in Fig. 2.11 (c). However, $\Theta(t)$ rises from 0 to $\pi/2$ during the very short period when the pulses overlap, thereby generating a large nonadiabatic coupling $\dot{\Theta}(t)$, which ruins the population transfer.

Optimum delay: For maximal adiabaticity, the mixing angle $\Theta(t)$ must change slowly and smoothly in time [cf. Fig. 2.9], so the nonadiabatic coupling $\dot{\Theta}(t)$ remains small. The optimal value of ΔT depends on the pulse shapes: for Gaussian pulses, the optimum delay is slightly larger than the pulse width

$\Delta T \geq \tau$.

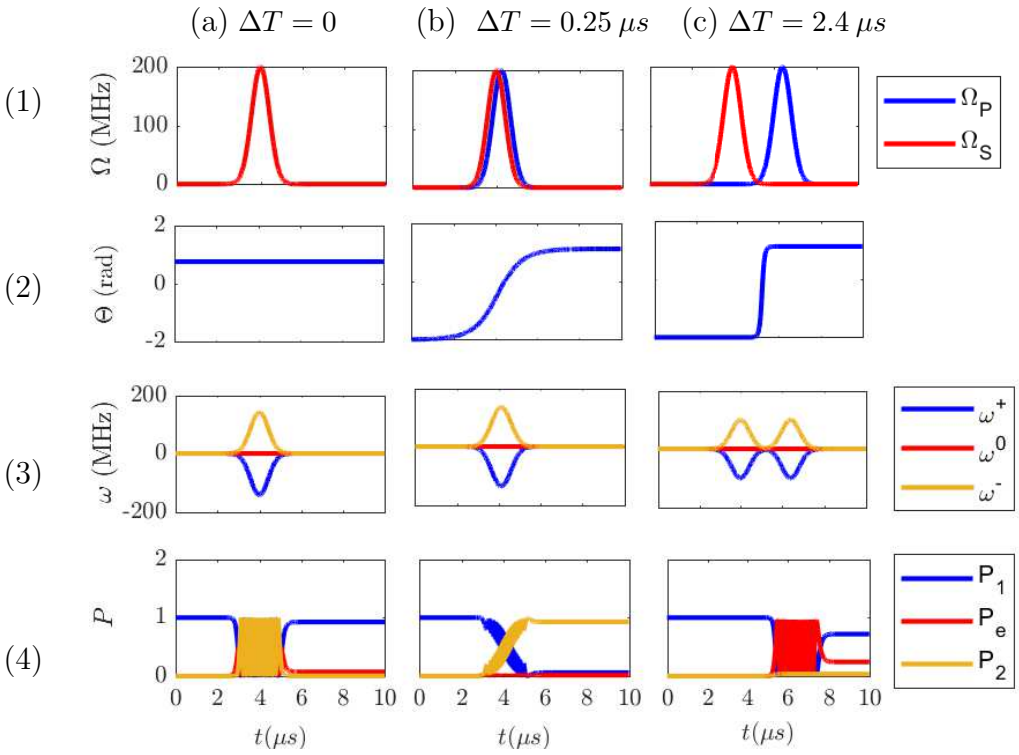

Figure 2.11: (a) Coincident pump and Stokes pulses $\Delta T = 0$. (b) Pump and Stokes pulses are separated in time by of $\Delta T = 0.25\,\mu s$. (c) Pump and Stokes pulses are separated in time by $\Delta T = 2.4\,\mu s$. Time evolution of (1) the Rabi frequencies of the pump and Stokes lasers; (2) the mixig angle Θ; (3) the dressed-state eigenvalues ω and (4) the probability amplitudes of the states. In this calculation: $d_P = d_S = 1$, $\tau = 0.6\,\mu s$ have been considered.

Single- and two-photon linewidths

A characterizing feature of the STIRAP is the variation of the single- and two-photon linewidths with the detunings Δ_P and Δ_S. Variation of either carrier frequency, while keeping the other fixed, will change the two-photon detuning δ. Variation of both the P and S frequencies, while maintaining the two-photon resonance condition, will produce the single-photon detuning. The dependencies of the transfer efficiency TE on δ and Δ are different. STIRAP is very sensitive to the two-photon detuning δ because the formation of the dark state $|a_0\rangle$ requires two-photon resonance $\delta = 0$. On the other hand, the

formation of the dark state $|a_0\rangle$ is not prevented by a non-zero single-photon detuning Δ. As it can be seen in the Fig. 2.12, increasing the single-photon detuning Δ does not limit the transfer efficiency as long as we are close to the two-photon resonance, $\delta = 0$. This criterion gets stricter as we increase the single-photon detuning.

Fig. 2.13 shows that considerable population transfer from the state $|1\rangle$ to $|2\rangle$ can occur if the nonadiabatic couplings arising from non-zero δ are suppressed by increasing Rabi frequency, which leads to the estimate of the full width at half maximum (FWHM) of the two-photon resonance $\delta_{1/2} \propto \Omega_{max}$ [92]. Hence the two-photon linewidth is proportional to the square root of the peak intensity of the laser light.

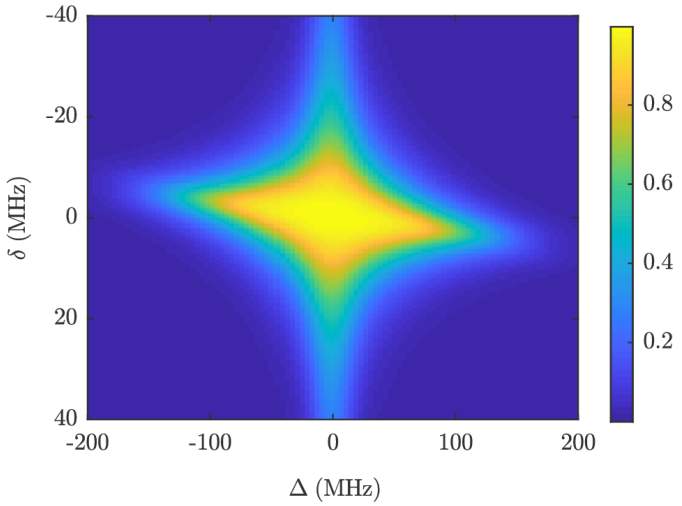

Figure 2.12: Transfer efficiency from the state $|1\rangle$ to $|2\rangle$ in the three-level Λ system shown in Fig. 2.8 (b). In this calculation $A_P = A_S = 100$ MHz, $d_P = d_S = 1$, $\tau = 0.5\ \mu$s, and $\Delta T = 2.5\ \mu$s are considered.

2.5 Summary

In this chapter, we first introduced the difference between the conventional type-I QDs and the newly emerged type-II QDs. Then, we explained the numerical tools for calculating the single-particle states of the QDs and also the method that we have chosen to use in this work. For calculating exciton state

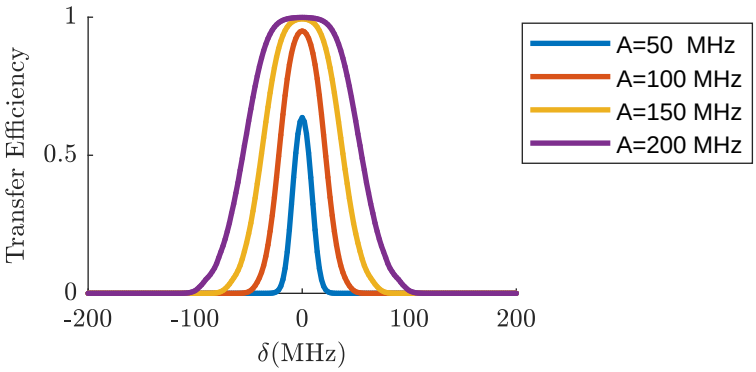

Figure 2.13: Transfer efficiency TE as a function of the two-photon detuning δ for different values of the lasers' peak amplitude: $A = A_P = A_S = 50$, 100, 150, 200 MHz. In this calculation, we considered $d_P = d_S = 1$, $\tau = 0.5\ \mu s$, $\Delta T = 1.2\ \mu s$, $\Delta = 0$.

we need to include Coulomb interaction in the model since it is the dominant effect in comparison to the QD confinement effect in the type-II configuration. Including Coulomb interaction makes the Schrödinger equation difficult to solve. For this reason, we presented the basic theory of the configuration-interaction method for solving the exciton problem.

Quantum gates are going to be designed based on the studied model of the type-II QDs by using the stimulated Raman adiabatic passage. Thus, we also presented the essential basic theory of this process in the last section of this chapter. In Chapter 4, we will explain the novel scheme we develop for implementing scalable and addressable single- and two-qubit gates based on type-II QDs in a nanowire.

CHAPTER 3

Coulomb interaction

This chapter is organized as follows. After a short introduction on the exciton problem, I develop the formalism to calculate the Coulomb matrix elements for the exciton problem in a QD nanowire in a cylindrical coordinate. Then, the formula to calculate the exciton oscillator strength is presented. The convergence of the configuration-interaction method to calculate the exciton states is explored. Next, a thorough investigation of the exciton properties in the novel type-II SDQ and DQD nanowires is presented. We also bring some important features of the type-I QD exciton properties to compare with those of the type-II QDs. Finaly we develop a semi-analytical formalism of the exciton problem and solve it with FEM COMSOL to verify the developed numerical tool based on the configuration-interaction method.

Our contribution here is developing a formalism to calculate the exciton properties in a QD nanowire and carry out all the research, development and implementation of the numerical code, convergence check and validation of the computational method, interpretation and discussion of the computation results.

3.1 Exciton

The simplest excitation in a semiconductor occurs when an electron from the valence band jumps across the band gap into the conduction band. In this

case, an empty positively charged hole state is created within the valence band. Charges of the opposite signs, the electron and the hole are bound by the Coulomb interaction between them. This bound electron-hole state is known as the exciton. Since the hole mass is generally much larger than the electron mass, the exciton is similar to a hydrogen atom such that the electron orbits the hole. The exciton moves, as a free particle with mass $M = m_e^* + m_h^*$, whereas the mass of the exciton's relative motion is $\mu = m_e^* m_h^*/M$. The difference in energy between an electron-hole pair interacting by their mutual Coulomb attraction and an uncorrelated electron-hole pair known as exciton binding energy, in the bulk semiconductor by the hydrogen-like analog becomes [93]:

$$E_B = -\frac{\mu e^4}{2\epsilon^2 \hbar^2} = -\frac{e^2}{2\epsilon a_{ex}} \tag{3.1}$$

where ϵ is the dielectric constant and $a_{ex} = \epsilon\hbar^2/\mu e^2$ is the effective Bohr radius characterizing the spatial extent of the exciton in the semiconductor after which the exciton wavefunction rapidly goes to zero. Using the typical values for the bulk InP, one can obtain the exciton binding energy of -5.4 meV and the Bohr radius of 11 nm. The total energy of the exciton in the bulk is simply the energy of the band gap plus the exciton binding energy (since the Coulomb potential energy is negative, the excitonic levels will be below the conduction band in the bulk), whereas in a nanostructure like a QD there are additional components due to the electron and the hole confinement:

$$E_{ex} = E_g + E_B \ \text{(bulk)} \qquad E_{ex} = E_g + E_e + E_h + E_B \ \text{(QD)} \tag{3.2}$$

here E_e and E_h are the single-particle energies which I described and calculated in Chapter 2. They depend on the shape and size of the QD. The exciton binding energy in a QD is also a function of the dimension of the QD. In fact, both the electron and the hole, which are bound by the Coulomb interaction are also confined by the conduction and valence band offsets, ΔE_c and ΔE_v, respectively. It has been shown in type-I QDs that confining an exciton increases its binding energy through increasing the spatial overlap between the electron and the hole [94, 93, 30]. In this chapter, we study how the QD size affects the excitonic properties in the novel type-II QD structures.

To calculate the exciton energy and wave function, the Hamiltonian of (2.13) has to be diagonalized. In Sec. 2.3, I showed how the Hamiltonian

matrix elements (the Coulomb matrix elements) in the basis of the single-particle states are calculated from the following integral:

$$V_{ij,kl} = \langle ij|\, \hat{H}_C \,|kl\rangle = \int\int d\boldsymbol{r}\, d\boldsymbol{r}' \Phi_i^*(\boldsymbol{r})\Phi_j^*(\boldsymbol{r}')\frac{q_1 q_2}{4\pi\epsilon|\boldsymbol{r}-\boldsymbol{r}'|}\Phi_k(\boldsymbol{r}')\Phi_l(\boldsymbol{r}) \quad (3.3)$$

This integral is problematic to evaluate due to the divergence at $\boldsymbol{r} = \boldsymbol{r}'$. In the following, I show how to calculate the Coulomb matrix elements in Eq. (3.3).

Calculating Coulomb Integral

We can write $\frac{1}{|\boldsymbol{r}-\boldsymbol{r}'|}$ based on the generating function of the circular cylindrical harmonics as [95]:

$$\frac{1}{|\boldsymbol{r}-\boldsymbol{r}'|} = \sum_{s=-\infty}^{+\infty} e^{is(\theta-\theta')}\int_0^\infty J_s(kR)J_s(kR')e^{-k|z-z'|}dk \quad (3.4)$$

By assuming that ϵ is constant in Eq. (3.3), which is a good approximation in crystal-phase QDs, and by substituting Eqs. (3.4) and (A.17) into Eq. (3.3):

$$\begin{aligned} V_{ij,kl} = -\frac{e^2}{4\pi\epsilon}\int\int \sum_{s=-\infty}^{+\infty} e^{is(\theta-\theta')}\int_0^\infty J_s(kR)J_s(kR')e^{-k|z-z'|}dk \\ \times \mathcal{R}_e^k(R)\Theta_e^k(\theta)\mathcal{Z}_e^k(z)\mathcal{R}_h^l(R')\Theta_h^l(\theta')\mathcal{Z}_h^l(z') \\ \times \mathcal{R}_e^{i*}(R)\Theta_e^{i*}(\theta)\mathcal{Z}_e^{i*}(z)\mathcal{R}_h^{j*}(R')\Theta_h^{j*}(\theta')\mathcal{Z}_h^{j*}(z') \\ \times R\,dR\,d\theta\,dz\,R'\,dR'\,d\theta'\,dz' \end{aligned} \quad (3.5)$$

For simplicity of notations in this section, I use $\phi_{QW}(z) \equiv \mathcal{Z}(z)$, $\phi_R(R) \equiv \mathcal{R}(R)$ and $\phi_\theta(\theta) \equiv \Theta(\theta)$ for single-particle wavefunctions. For calculating the integral in (3.5), I first integrate over θ, then make the summation over s. Therefore, I need to calculate the following expression first:

$$\sum_{s=-\infty}^{+\infty} J_s(kR)J_s(kR')\int\int e^{is(\theta-\theta')}\Theta_e^k(\theta)\Theta_h^l(\theta')\Theta_e^{i*}(\theta)\Theta_h^{j*}(\theta')d\theta\,d\theta' \quad (3.6)$$

By using the normalized $\Theta(\theta) = \frac{1}{\sqrt{2\pi}}e^{im\theta}$ [from Eq. (2.11)] Eq. (3.6) becomes:

$$(\frac{1}{\sqrt{2\pi}})^4 \sum_{s=-\infty}^{+\infty} J_s(kR)J_s(kR')\int\int e^{is(\theta-\theta')}e^{im_k\theta}e^{im_l\theta'}e^{-im_i\theta}e^{-im_j\theta'}\,d\theta\,d\theta' \quad (3.7)$$

Since $\int_0^{2\pi} \frac{e^{in'\theta}e^{in\theta}d\theta}{2\pi} = \delta_{n,n'}$, the above expression is simplified as:

$$\sum_{s=-\infty}^{+\infty} \delta_{s,m_k-m_i}\delta_{s,m_j-m_l} J_s(kR)J_s(kR') = J_s(kR)J_s(kR') \tag{3.8}$$

where $s = m_k - m_i = m_j - m_l$ in the right-hand side of the above equation. By substituting the right-hand side of Eq. (3.8) in Eq. (3.5):

$$V_{ij,kl} = -\frac{e^2}{4\pi\epsilon}\int\int_{k,z,z'} dk\, dz\, dz'\, e^{-k|z-z'|}\mathcal{Z}_e^{n_k}(z)\mathcal{Z}_h^{n_l}(z')\mathcal{Z}_e^{n_i*}(z)\mathcal{Z}_h^{n_j*}(z')$$
$$\times \int_R RJ_s(kR)\mathcal{R}_e^{l_k,m_k}(R)\mathcal{R}_e^{l_i,m_i*}(R)\,dR \int_R R'J_s(kR')\mathcal{R}_h^{l_l,m_l}(R')\mathcal{R}_h^{l_j,m_j*}(R')\,dR' \tag{3.9}$$

By replacing the single-particle states described in Chapter 2 in Eq. (3.9) and integrating over dR, dR', dz, dz', and dk, the Coulomb matrix elements are calculated. By adding the single-particle electron and hole energies to the diagonal elements of the Coulomb matrix, according to Eq. (2.13), the total Hamiltonian of the interacting electron and hole system is constructed. Then, the Hamiltonian is diagonalized. The eigenenergies of the Hamiltonian correspond to the exciton energies and the eigenstates are the exciton states in the basis of the single-particle configurations, such that the μth excitonic eigenstate is given by:

$$\Psi_{exc}^{\mu}(\boldsymbol{r}_e, \boldsymbol{r}_h) = \sum_{i,j} C_{ij}^{\mu}\Phi_e^i(\boldsymbol{r}_e)\Phi_h^j(\boldsymbol{r}_h), \tag{3.10}$$

here, C_{ij} are the elements of the μth eigenvector of the Hamiltonian matrix and i and j are indices summarizing the quantum numbers (nlm) of the single-particle electron and hole states, respectively.

3.2 Oscillator strength

Enhancement of the light-matter interaction is very important for many optical devices [96], such as semiconductor lasers, single-photon sources, detectors, light-emitting diodes, and also for quantum information processing devices. The relevant figure-of-merit in the dipole approximation is the exciton oscillator strength, which is a dimensionless quantity. The oscillator strength of

the excitonic transition is defined by [30]:

$$OS = \frac{2}{m_0 \hbar \omega_{exc}} \Big| \langle G| \, \mathbf{e} \cdot \hat{\mathbf{d}} \, |X\rangle \Big|^2 \tag{3.11}$$

Here, $|G\rangle$ stands for the ground state, $|X\rangle$ is the exciton state, $\mathbf{e}$ is the unit vector of the light polarization, $\hat{\mathbf{d}}$ is the dipole moment operator, and ω_{exc} is the exciton transition frequency. To evaluate the expression (3.11), we write the states in the electron picture rather than in the equivalent electron-hole picture. The ground-state is:

$$|G\rangle = \mathcal{A}\{ \, |u_v, \Phi_h^1\rangle \, , ..., |u_v, \Phi_h^n\rangle \, \} \tag{3.12}$$

where $\mathcal{A}$ is the anti-symmetrization operator. Each state vector in (3.12) contains two parts: the valence band Bloch function part u_v and the hole envelope function part Φ_h. There is also a spin part which we have dropped here, since it does not affect the result if we assume that the spin of the electron doesn't change when it moves from the valence band to the conduction band. In the ground state of the structure $|G\rangle$, the valance band is full of electrons. They occupy all allowed single-particle states of the hole. The conduction band is empty as there are no electrons there. If an electron is excited from the valence band to the conduction band, an exciton state will form. We write the μth exciton state of Eq. (3.10) in the electron picture as:

$$|X^\mu\rangle = \sum_{i,j} C_{ij}^\mu \mathcal{A}\{ \, |u_c, \Phi_e^i\rangle \prod_{k \neq j} \Big| u_v, \Phi_h^k \Big\rangle \, \} \tag{3.13}$$

This implies that, all the allowed single-particle states in the valence band are occupied by electrons, except one, which is moved to an allowed single-particle electron state in the conduction band. We drop the anti-symmetrization operator $\mathcal{A}$ henceforth for simplicity. Now, by substituting (3.13) and (3.12) in (3.11) we have:

$$\begin{aligned} OS^\mu &= \frac{2}{m_0 \hbar \omega_{ex}^\mu} \Big| \langle G| \, \mathbf{e} \cdot \hat{\mathbf{d}} \, |X^\mu\rangle \Big|^2 \\ &= \frac{2}{m_0 \hbar \omega_{ex}^\mu} \big| \langle u_v| \, \mathbf{e} \cdot \hat{\mathbf{d}} \, |u_c\rangle \big|^2 \Big| \int d\boldsymbol{r} \sum_{i,j} C_{ij}^\mu \Phi_h^{j*}(\boldsymbol{r}) \Phi_e^i(\boldsymbol{r}) \Big|^2 \end{aligned} \tag{3.14}$$

In Appendix C, we have derived how $\langle u_v, \Phi_h| \, \mathbf{e} \cdot \hat{\mathbf{d}} \, |u_c, \Phi_e\rangle$ reduces to $\langle u_v| \, \mathbf{e} \cdot \hat{\mathbf{d}} \, |u_c\rangle \, \langle \Phi_h|\Phi_e\rangle$ used in the above equation. $\langle u_v| \, \mathbf{e} \cdot \hat{\mathbf{d}} \, |u_c\rangle$ is measured from the

experiments and denoted by M [64], then Eq. (3.14) simplifies to:

$$OS^{\mu} = \frac{2|M|^2}{m_0 \hbar \omega_{exc}^{\mu}} \left| \int d\boldsymbol{r} \sum_{i,j} C_{ij}^{\mu} \Phi_h^{j*}(\boldsymbol{r}) \Phi_e^{i}(\boldsymbol{r}) \right|^2 \tag{3.15}$$

Thus, for calculating the OS of the μ^{th} exciton transition, we need to know the C^{μ} (the μ^{th} eigenvector of the Hamiltonian H), Φ_e and Φ_h the single-particle wavefunctions.

3.3 Convergence study of the configuration-interaction method

The Coulomb integral in (3.9) need to be evaluated numerically. The integrals over R, R', z and z' are straightforward. For the remaining one-dimensional integral over k, we need to first truncate the integral using a cut-off k_{cut} and subsequently discretizing it with a discretization step Δk. When introducing the truncation and the discretization, careful convergence studies are required. Typical convergence studies for the cut-off k_{cut} and the discretization step Δk are presented in Fig. 3.1. Here, we study the ground-state exciton energy which is the lowest eigenvalue of the Hamiltonian matrix and its normalized oscillator strength. Oscillator strength is calculated from (3.15), and the normalized exciton oscillator strength is defined as $OS_N = OS/OS_0$ where $OS_0 = 2|M|^2/m_0\hbar\omega_{exc}$. We have excluded the band gap energy in the figures such that we define $E_{ex} = \hbar\omega_{exc} - E_g$. As it can be seen in this figure considering $k_{cut} = 1$ nm^{-1} and discretization $\Delta k = 0.01$ nm^{-1} result in a good convergence for both the OS and the exciton energy in the considered geometry.

We need to truncate the Hilbert space of the single-particle electron and hole states in our calculation while ensuring that enough states are included to achieve convergence. For larger structures, the energy spacing of the single-particle states decreases, and an increasing number of higher-order single-particle electron and hole states are needed to correctly represent the ground-state exciton wave function and energy.

Fig. 3.2 shows the convergence study of the exciton oscillator strength and energy as a function of the number N_T which is equal to N_{Te} (N_{Th}) of the

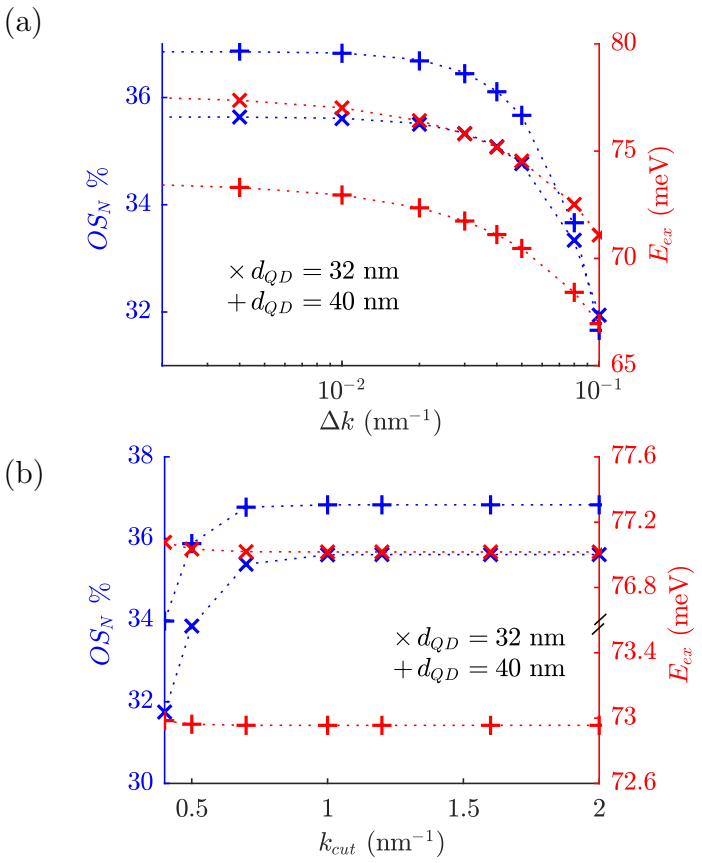

Figure 3.1: Convergence study of the ground-state exciton OS_N and E_{ex} as function of (a) Δk with $k_{cut} = 1$ nm^{-1} and as function of (b) k_{cut} with $\Delta k = 0.01$ nm^{-1}. The SQD nanowire geometrical parameters are $l_{NW} = 70$ nm and $h_{QD} = 4$ nm. We consider two cases with $d_{QD} = 32$ nm (crosses) and $d_{QD} = 40$ nm (plusses).

in-plane transverse electron (hole) single-particle states $\phi_T^{lm}(R, \theta)$ for two diameters $d_{QD} = 32$ nm and $d_{QD} = 40$ nm. The figure reveals that the ground-state exciton energy E_{ex} converges much faster than the OS_N: The variation of the exciton OS_N is around 200 % in the total interval considered, whereas the variation for the exciton energy is less than 2 %. As the QD diameter increases, the energy spacing between the single-particle electron and hole states in the transverse in-plane direction become comparable or smaller than the ground-state exciton binding energy and we need to include more in-plane single-particle states in the calculation: Closer inspection of Fig. 3.2 reveals convergence is slower for the $d_{QD} = 40$ nm diameter than for the $d_{QD} = 32$

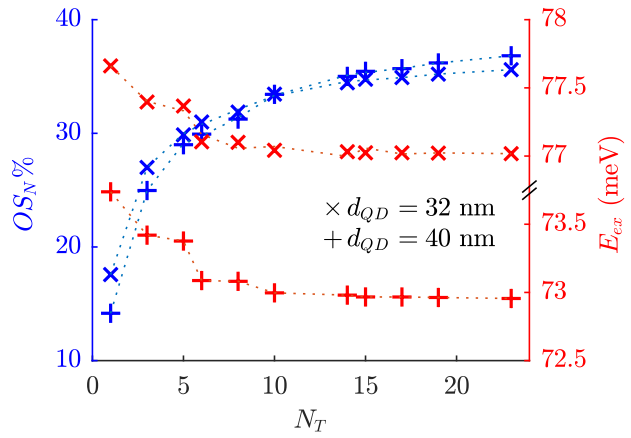

Figure 3.2: Convergence study of the ground-state exciton OS_N and E_{ex} as a function of the number $N_T = N_{Te} = N_{Th}$ which is the in-plane transverse single-particle electron (hole) states for two diameters $d_{QD} = 32$ nm (crosses) and $d_{QD} = 40$ nm (plusses). The SQD nanowire structure parameters are $l_{NW} = 70$ nm and $h_{QD} = 4$ nm. In this calculation we considered $N_{ze} = 1$ and $N_{zh} = 20$ for the single-particle electron and hole states along z axis, respectively, and we have $\Delta k = 0.01$ nm^{-1} and $k_{cut} = 1$ nm^{-1}.

nm case.

The same argument also applies for other geometrical parameters like the nanowire length. Since in the type-II structure the hole is spread all over the nanowire outside of the QD, as the nanowire length increases, the energy spacing of the single-particle hole states along the z axis is reduced and additional higher single-particle hole states contribute to the ground-state exciton wavefunction and energy. Then for longer nanowires we need to include more single-particle hole states to achieve convergence. The electron is confined inside the QD and increasing the length of the nanowire doesn't affect the number of the confined single-particle electron states. On the other hand, by increasing the QD height, the energy separation of the single-particle electron states is reduced and more single-particle electron states are needed in the calculation to obtain convergence.

3.4 Exciton states in type-II QDs in nanowires

The exciton properties of the type-II QDs are studied in this section. First, we present the results for the SQD configuration. The DQD exciton properties are

different from the SQD exciton properties. Because of the delocalized electron and hole states in the SQD, the exciton oscillator strength has a smalle value in this structure in comparison to that of the type-I SQD structure. We show by confining the hole part of the exciton between two QDs in a type-II DQD structure a large oscillator strength can be achieved.

3.4.1 Single-quantum-dot in a nanowire

The ground-state exciton probability density $|\Psi_{exc}(\boldsymbol{r}_h, \boldsymbol{r}_e)|^2$ at $R_e = R_h = 0$ for the SQD geometry is shown in Fig. 3.3 (a) and (b) in the presence and the absence of the Coulomb interaction, respectively. We observe that without Coulomb interaction, the hole part of the exciton wavefunction is spread all over the nanowire. In the presence of the Coulomb interaction, the hole is attracted to the electron leading to a hole confined to the surroundings of the QD. Fig. 3.3 (c) and (d) present the wavefunction $|\Psi_{exc}(\boldsymbol{r}_h, \boldsymbol{r}_e)|^2$ at $z_e = z_h = \theta_e = \theta_h = 0$ which corresponds to the radial distribution of the exciton wavefunction with and without the Coulomb interaction, respectively. The figures indicate that the Coulomb interaction has made the exciton state more confined toward the center of the nanowire which makes the exciton less affected by the unwanted surface potentials. Because the electron mass and the hole mass are not the equal, the radial wavefunction is not equally squeezed by the Coulomb effect along the hole and the electron radial coordinates, as it can also be seen in the Fig. 3.3 (c).

Fig. 3.4 (a) and (b) show the normalized oscillator strength OS_N versus the exciton energy E_{ex} in the case of including and neglecting the Coulomb interaction, respectively. A closer comparison of the figures reveals that the Coulomb interaction is important and should not be neglected: The notable effects are:

(1) The attractive Coulomb interaction causes a red shift of the exciton transition energies of around 10 meV, which is the exciton binding energy. The binding energy in the type-II QD has been enhanced in comparison to the exciton binding energy in the bulk InP which was calculated 5.4 (meV) in Sec. 3.1.

(2) The Coulomb interaction results in an increase of the ground-state

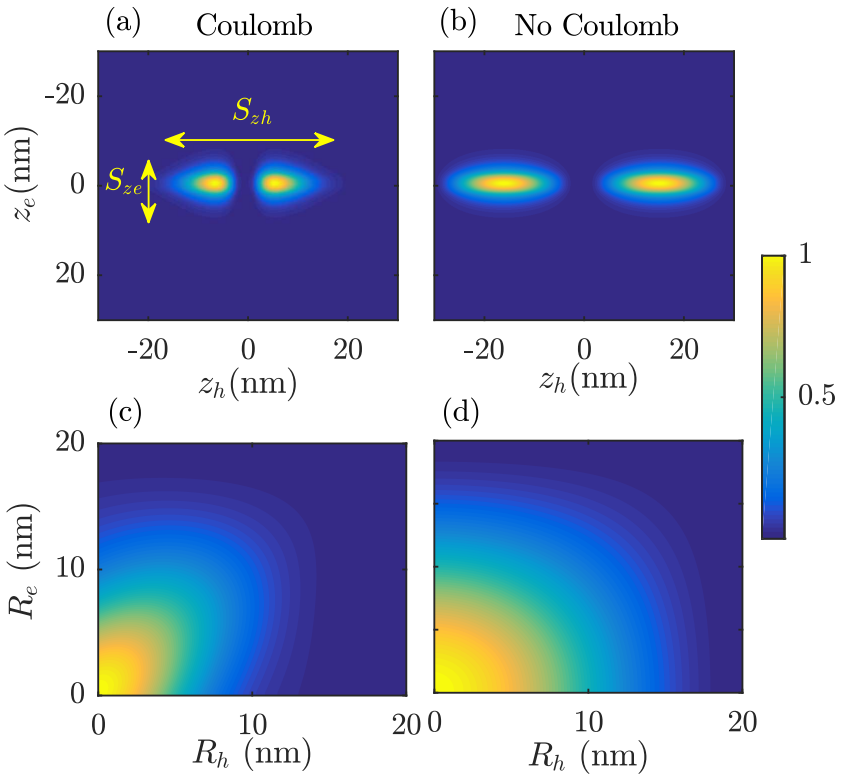

Figure 3.3: Ground-state exciton probability density $|\Psi_{exc}(\boldsymbol{r}_h, \boldsymbol{r}_e)|^2$ for $R_e = R_h = 0$ in the (a) presence and (b) absence of Coulomb interaction. Exciton probability for $z_e = z_h = \theta_e = \theta_h = 0$ in the (c) presence and (d) absence of Coulomb interaction. The geometrical parameters of the SQD nanowire are: $d_{QD} = 40$ nm, $h_{QD} = 4$ nm and $l_{NW} = 60$ nm.

exciton OS_N value of about a factor of 20 compared to the case without the Coulomb interaction.

(3) While the expansion of the ground-state exciton in the absence of the Coulomb interaction only includes the $\Phi_e^{100}, \Phi_h^{100}$ single-particle components, in the presence of the Coulomb interaction other components than the ground single-particle states are also contribute. For example Table. 3.1 shows some of the single-particle components which are contributing to the ground-state exciton oscillator strength. For quantifying this contribution, we define the parameter R as:

$$R_{ij} = \left| \frac{\int C_{ij} \Phi_e^i(\boldsymbol{r}_e) \Phi_h^j(\boldsymbol{r}_h) d\boldsymbol{r}}{\int \Sigma_{i,j} C_{ij} \Phi_e^i(\boldsymbol{r}_e) \Phi_h^j(\boldsymbol{r}_h) d\boldsymbol{r}} \right|^2 \tag{3.16}$$

which is the ratio of a specific single-particle electron and hole component in

the oscillator strength overlap integral to the total amount of the oscillator strength. In Table 3.1, we number the single-particle components from the lowest energy states such that N_0 corresponds to the single-particle electron and hole components which have the lowest total energy $(E_e + E_h)$. It can be seen, the contribution of the components $\Phi_e^{100}, \Phi_h^{200}$ and $\Phi_e^{100}, \Phi_h^{300}$ is more than $\Phi_e^{100}, \Phi_h^{100}$. Table. D.1 shows the forty lowest energy single-particle states contributing to the ground-state exciton oscillator strength which you can see for more detail about the single-particle components contributing to the oscillator strength.

(4) The energy difference between the ground exciton state and the first-excited exciton state considerably increases in the presence of Coulomb interaction. It is important because it means there will be less pure dephasing of the ground-state due to the virtual phonon decoherence processes [97].

I've brought more details about the exciton states in Appendix D. The exciton wavefunctions correspond to the exciton states of the Fig. 3.4 (a) are shown in Fig. D.1. Table. D.2 also provides the exact values of the oscillator strength and the energy of the exciton states.

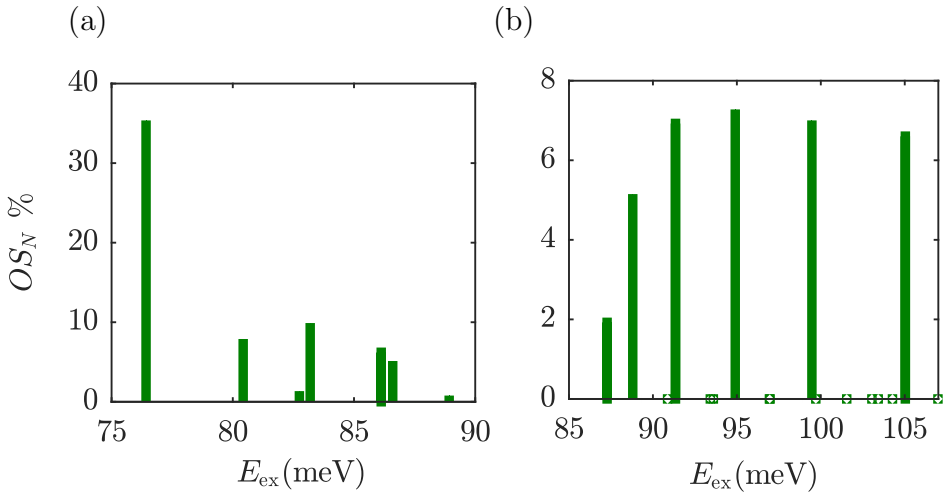

Figure 3.4: Normalized oscillator strength in the lowest-energy part (a) when including Coulomb interaction and (b) in the absence of Coulomb interaction. The SQD nanowire geometrical parameters are $d_{QD} = 36$ nm, $h_{QD} = 4$ nm and $l_{NW} = 70$ nm.

To investigate the influence of the nanowire boundaries on the excitonic properties, we vary the length of the nanowire and study the spatial extent of

	$i := (n,l,m)_e$	$j := (n,l,m)_h$	R %
N_0	1,0,0	1,0,0	13.1 %
N_1	1,0,0	2,0,0	23.76 %
N_6	1,0,0	3,0,0	18.26 %
N_{15}	1,0,0	4,0,0	10 %
N_{31}	1,0,0	5,0,0	4.91 %

Table 3.1: Some of the single-particle components which are contributing to the ground-state exciton oscillator strength. The geometrical parameters of the SQD in a nanowire are $l_{NW} = 70$ nm, $d_{QD} = 36$ nm, $h_{QD} = 4$ nm.

the electron and hole parts of the wavefunction. We define the exciton sizes S_{ze}/S_{zh} such that the electron/hole part of the exciton probability is 0.001 of its maximum value along the z_e/z_h axis when $R_e = R_h = 0$, see Fig. 3.3 (a). Fig. 3.5 (a) reveals that S_{zh} is increasing linearly with the nanowire length l_{NW} up to ≈ 60 nm after which the size assumes a constant value independent of the nanowire length. Whereas for smaller nanowires the hole confinement is defined by the nanowire boundary, for $l_{NW} > 60$ nm the confinement mechanism along the nanowire axis is thus dominated by Coulomb attraction to the localized electron. The dependence of the normalized oscillator strength OS_N and energy E_{ex} of the ground-state exciton as a function of the nanowire length is presented in Fig. 3.5 (b). We observe that these parameters also assume length-independent values for nanowire lengths above ≈ 60 nm similarly to the exciton size in Fig. 3.5 (a). We conclude that when the nanowire length is larger than the exciton hole size along the z axis, the exciton properties become independent of l_{NW}.

The dependence of the ground-state exciton OS_N as a function of the nanowire diameter is shown in Fig. 3.6. When increasing the QD diameter, the electron and the hole have more space to move around and the lateral extension of the exciton increases, which means that the overlap integral in (3.15) increases and, in turn, the oscillator strength. While a large diameter initially appears attractive, on the other hand, by increasing the QD diameter the energy separation ΔE between the ground-state exciton and first-excited state decreases, as is shown in Fig. 3.6. For a nanowire of diameter above ≈ 60 nm (with $h_{QD} = 4$ nm), the difference ΔE becomes smaller than 1 meV, which makes it more challenging to experimentally address the ground-state

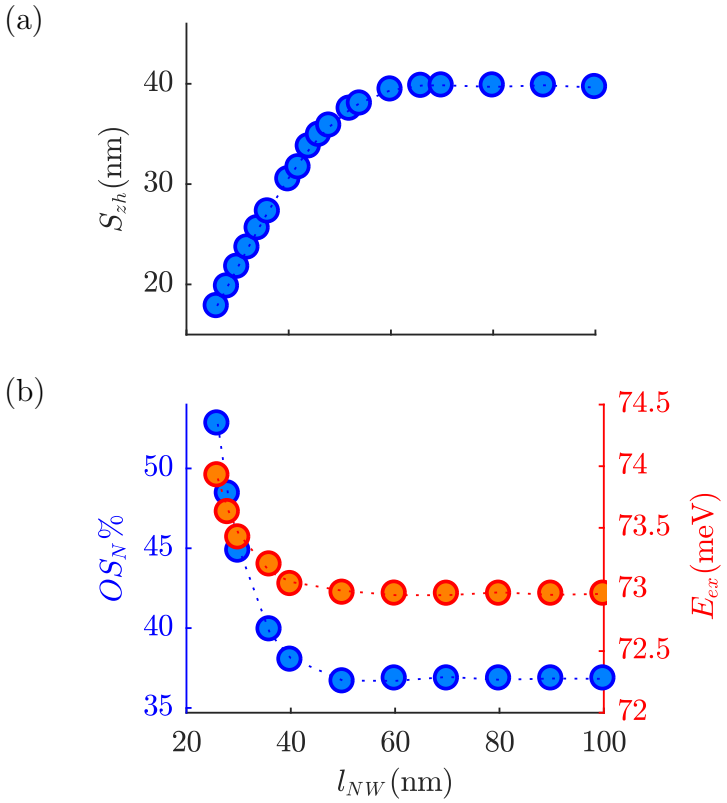

Figure 3.5: (a) Hole part of the exciton size S_{zh}, and (b) exciton energy E_{ex} and normalized oscillator strength OS_N as a function of the nanowire length l_{NW} for the ground-state exciton. The SQD nanowire geometrical parameters are $d_{QD} = 40$ nm and $h_{QD} = 4$ nm.

exciton . This is a first reason that we here are only considering nanowires with diameters up to 60 nm. Furthermore, for sufficiently large diameters, where the exciton size is no longer small compared to the optical wavelength, the dipole approximation breaks down leading to a stabilization of the oscillator strength for increasing diameter. [98]. However for the nanowires with $d_{QD} <$ 60 nm considered in this paper, the dipole approximation is valid and the oscillator strength increases with diameter as also observed in [98].

The dependence of the exciton sizes S_{ze} and S_{zh} along the electron and hole z axes as function of QD height h_{QD} is presented in Fig. 3.7 (a). When h_{QD} decreases, the electron is pushed out of the QD and the exciton electron size S_{ze} increases. In the limit when $h_{QD} \to 0$, the electron is strongly delocalized from the QD. This explains why, by decreasing h_{QD}, the exciton OS_N increases

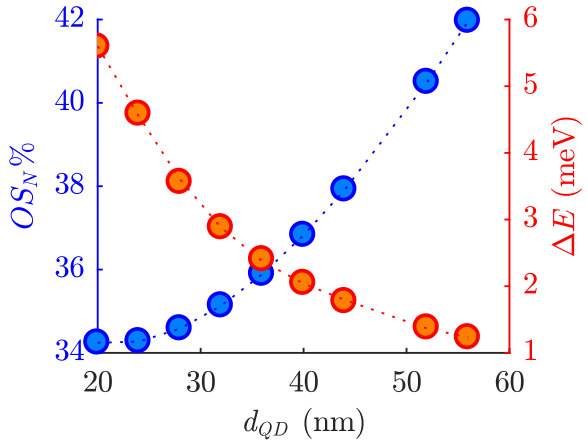

Figure 3.6: Ground-state exciton normalized oscillator strength OS_N and energy separation between the ground-state exciton and first-excited state ΔE as function of the QD diameter d_{QD}. The SQD nanowire geometrical parameters are $l_{NW} = 90$ nm and $h_{QD} = 4$ nm.

as observed in Fig. 3.7 (b): By decreasing h_{QD}, the probability of finding the electron and hole on the same site increases, leading to a larger overlap integral in Eq. (3.15) and, in turn, an improved oscillator strength.

While a large exciton oscillator strength can clearly be obtained using a large diameter d_{QD} or a small QD height h_{QD}, we note that in both cases a spatially large exciton is obtained with small energy separation to the first higher-order state. We thus conclude that the SQD geometry is not ideal for quantum gating applications. In the next section, I show that by engineering a DQD nanowire structure, it is possible to improve the exciton oscillator strength while maintaining a spatially well-confined profile.

Finally, while a symmetric nanowire geometry in which the QD is placed in the center of the nanowire was considered for all the SQD calculations presented in this section, for realistic SQD nanowires the QD may not be positioned exactly in the center. However, we have demonstrated that the exciton is confined by the Coulomb interaction for nanowire lengths above ≈ 60 nm. Thus, for a QD separated by more than 30 nm from the closest nanowire termination, the asymmetry is not expected to play any role.

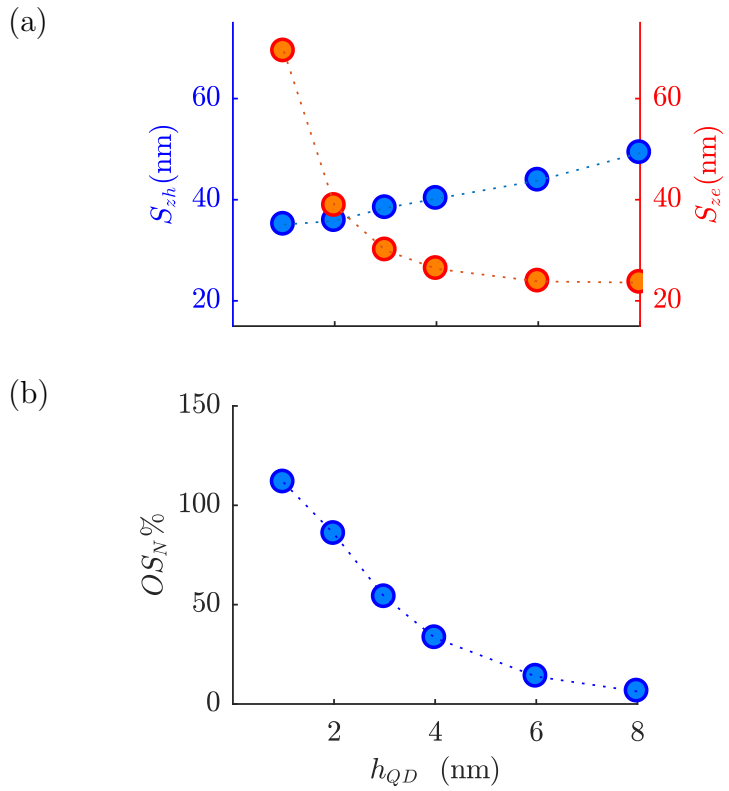

Figure 3.7: (a) Hole and electron part of the exciton sizes S_{zh} and S_{ze} and (b) normalized oscillator strength OS_N as a function of the QD height h_{QD} for the ground-state exciton. The SQD nanowire geometrical parameters are $l_{NW} = 90$ nm and $d_{QD} = 20$ nm.

3.4.2 Double-quantum-dot in a nanowire

While excitons in isolated QDs are generally limited to one or two qubit operations, the need for scalable qubit arrays has led to proposals of few-QD nanostructures like DQDs for physical realization of universal quantum logic gates [99, 100]. Additionally, pairs of vertically aligned type-I QDs for optically driven solid state quantum gates [101, 102, 103] have been suggested. We will now show that type-II DQDs in nanowires are also promising for implementing optically controlled quantum gates.

In the DQD nanowire structure shown in Fig. 3.8 (a), the single-particle electron states are confined to the QDs as for the SQD configuration. Fig. (3.9) shows the single-particle electron states in the z direction in a DQD structure. Fig. (3.10) shows the lowest energy single-particle hole states for a DQD

structure. As we can see in this figure, most single-particle hole states are predominantly localized in the outer nanowire regions surrounding the QDs. However, there are a few single-particle hole states which mainly are localized in the barrier region between two QDs, which we in the following refer to as bound-state holes. As we see in this figure, in all of the twelve lowest energy states, there is one single-particle hole state which is confined between the QDs whereas all other states are spread in the outside region of the DQD. Due to the strong localization of both the electron and the bound-state hole wavefunctions to the inner DQD region, it is possible in the DQD configuration to significantly improve the electron-hole overlap as compared to the SQD configuration.

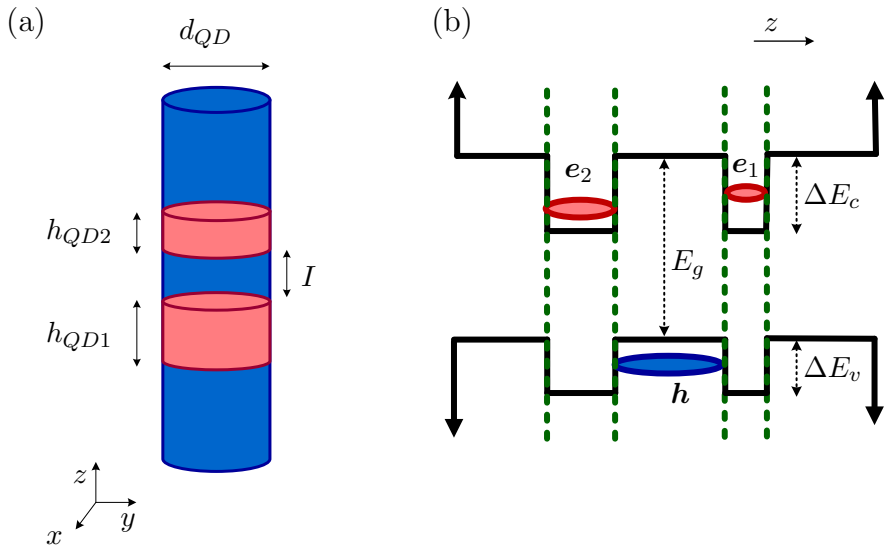

Figure 3.8: (a) A DQD in a nanowire. (b) The conduction and the valence band potential energy profiles along the z axis for the InP type-II DQD.

We first study the influence of the inner dot separation distance I on the exciton properties. The normalized oscillator strength of the lowest-energy bound-state exciton OS_N as function of I is presented in Fig. 3.11 (a). We observe an optimum value of I where the best trade-off between bound-hole leakage through the QD barriers and electron state penetration into the central barrier is obtained. Here, the OS_N value of the exciton transition is maximized and is more than 4 times larger than that of the ground-state exciton in a SQD nanowire for the same values of h_{QD} and d_{QD}. Fig. 3.11 (b) shows the exciton

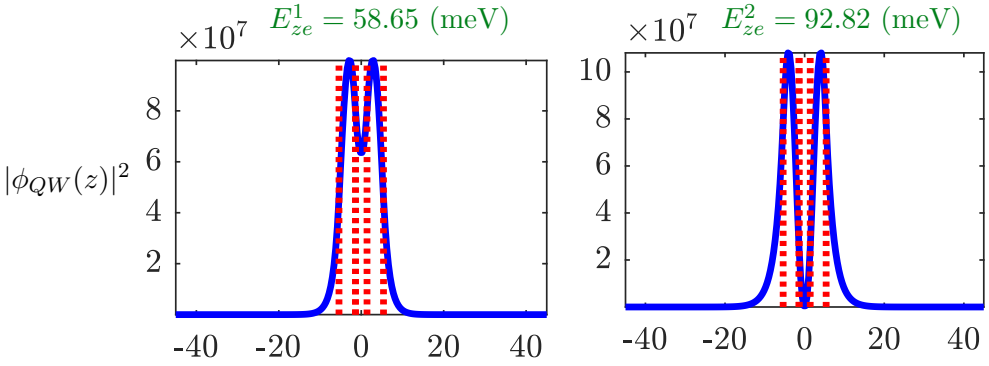

Figure 3.9: Probability density of the ground- and the first-excited states in the z direction $|\phi_{QW}(z)|^2$ of the electron in the conduction band of a type-II DQD nanowire. Geometrical parameters of the structure are $l_{NW} = 90$ nm, $I = 2.8$ nm, $h_{QD1} = h_{QD2} = 4$ nm.

electron and hole sizes along the z_e and z_h axes. We observe that the exciton is significantly more localized along the z_h axis compared to the SQD nanowire [cf. Fig. 3.7 (a)]. This feature of the DQD nanowire is a main asset making it highly suitable as a platform for optically controlled quantum gates.

The dependence of the bound exciton normalized oscillator strength OS_N and energy E_{ex} on the QD diameter d_{QD} is depicted in Fig. 3.12. As for the SQD geometry, we observe that OS_N increases with diameter within the dipole approximation. By choosing a DQD nanowire of ≈ 50 nm, we can achieve a large oscillator strength, which is a key parameter in quantum gates. Again, the diameter should be chosen as a trade-off between large oscillator stength and sufficient energy level difference between the exciton and the first higher order excitonic state as discussed in Sec. 3.4.1.

The exciton normalized oscillator strength in the lowest energy part for the DQD configuration is presented in Fig. 3.13. We observe a dominating peak at ≈ 78 meV, which corresponds to the lowest-energy bound-state exciton. The oscillator strength of the bound exciton is thus much stronger than other excitonic transitions in the lowest-energy part of the excitonic spectrum for the DQD structure. This feature makes selective excitation of the bound-state exciton feasible in experiments. Also since the real-space overlap between the interesting bound-state exciton and close-in-energy unbound-state excitons is small, phonon decay processes can be neglected [97].

Table (3.2) shows the most important components contributing to the OS

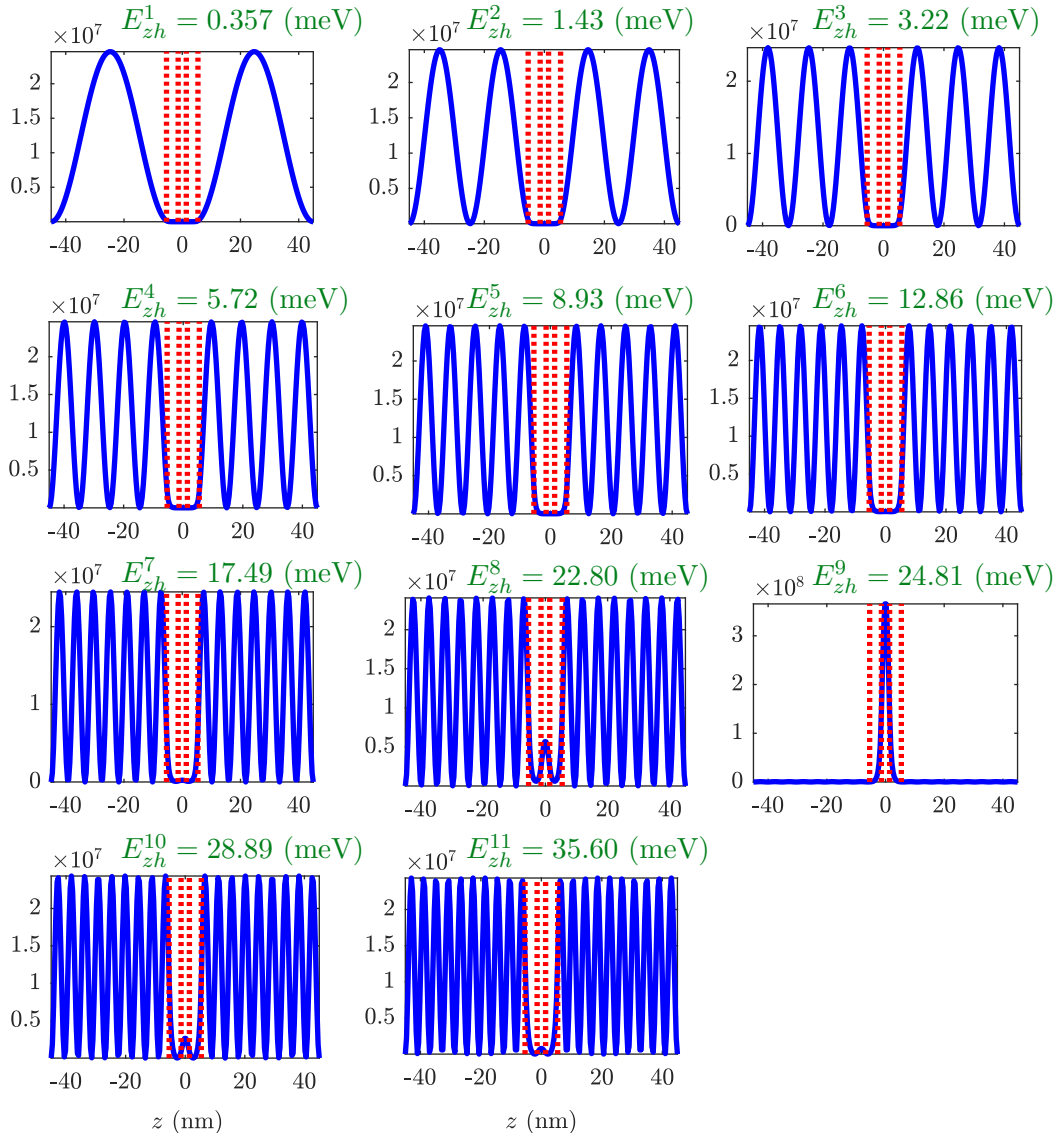

Figure 3.10: Probability density of the lowest-energy single-particle hole states in the z direction $|\phi_{QW}(z)|^2$ in the valence band of a type-II DQD nanowire. Geometrical parameters of the structure are $l_{NW} = 90$ nm, $I = 2.8$ nm, $h_{QD1} = h_{QD2} = 4$ nm.

of the bound-state exciton. We see that the bound single-particle hole state Φ_h^{900} is the most contributing hole component, i.e, more than 90% of the total amount. For this reason, we consider a simplified single-particle basis which only includes the bound Φ_h^{900} component for the single-particle hole state. Fig. (3.14) shows the calculated OS by using the simplified basis in comparison to the regular complete basis. As it can be seen in the figure

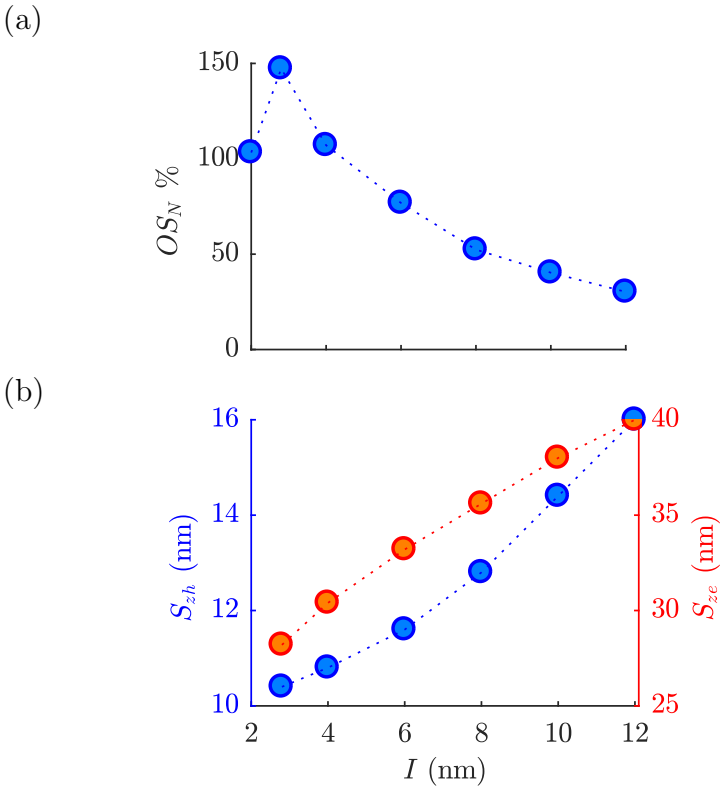

Figure 3.11: (a) Normalized oscillator strength OS_N for the lowest-energy bound-state exciton, and (b) size S_{zh} along the z_h axis and S_{ze} along the z_e axis as a function of inner dot separation I. The DQD nanowire geometrical parameters are $l_{NW} = 90$ nm, $d_{QD} = 52$ nm and $h_{QD1} = h_{QD2} = 4$ nm.

	$i := (n,l,m)_e$	$j := (n,l,m)_h$	R %
N_{123}	1,0,0	8,0,0	3.92 %
N_{132}	1,0,0	9,0,0	64.27 %
N_{398}	1,0,-1	9,0,1	10.1 %
N_{650}	1,0,1	9,0,1	10.1 %

Table 3.2: Some of the single-particle components which are contributing to the ground-state exciton oscillator strength. The geometrical parameters of the type-II DQD in a nanowire $l_{NW} = 90$ nm, $d_{QD} = 36$ nm, $h_{QD1} = h_{QD2} = 4$ nm, $I = 2.8$ nm.

there is a small difference between them while the computation time is quite different. While for the simplified basis the calculation is carried out in a few minutes using a typical personal computer, for the regular basis it takes 30 hours using ten paralleled cluster computers. Then using the simplified basis in the DQD configuration is a good approximation in the calculations.

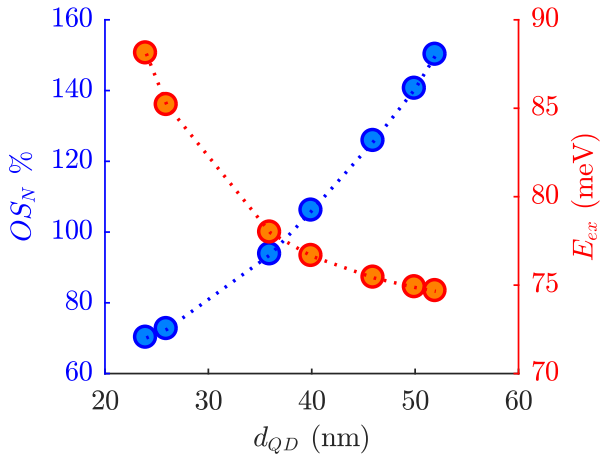

Figure 3.12: Normalized oscillator strength OS_N and energy E_{ex} as a function of the nanowire diameter d_{QD} for the lowest-energy bound-state exciton. The DQD nanowire geometrical parameters are $l_{NW} = 90$ nm, $h_{QD1} = h_{QD2} = 4$ nm and $I = 2.8$ nm.

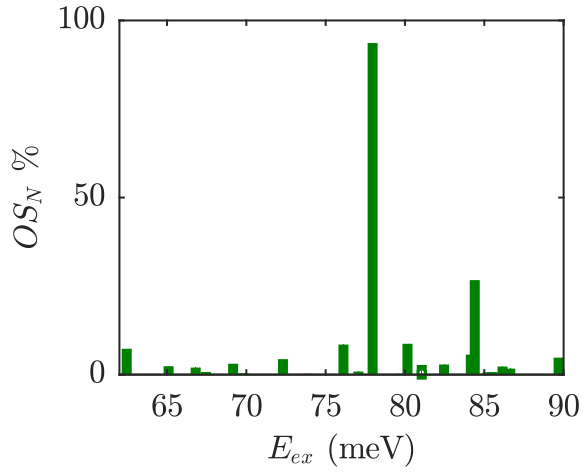

Figure 3.13: The exciton normalized oscillator strength in the lowest-energy part. The DQD nanowire geometrical parameters are $l_{NW} = 90$ nm, $h_{QD1} = h_{QD2} = 4$ nm, $I = 2.8$ nm and $d_{QD} = 36$ nm.

For realistic structures, asymmetry of the DQD geometry can occur due to a non-ideal fabrication process. We study in Fig. 3.15 the influence of the QDs height difference $\Delta h_{QD} = h_{QD2} - h_{QD1}$ on the oscillator strength of the lowest energy bound-state exciton for a fixed QD1 height of $h_{QD1} = 4$ nm. We observe that upon increasing the height of QD2 by 0.5 nm the

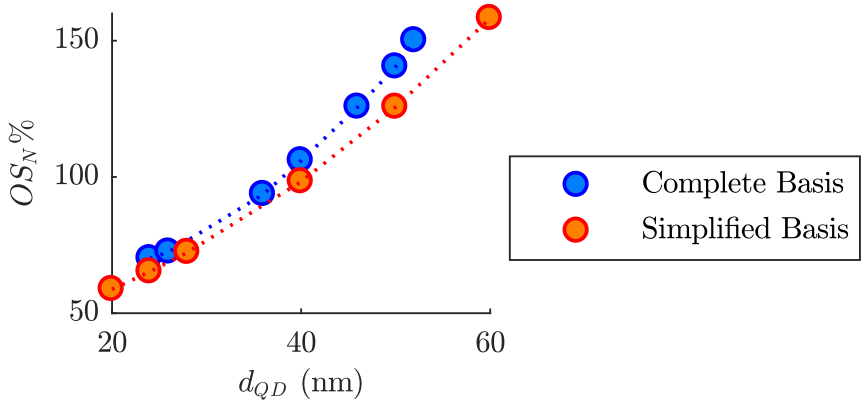

Figure 3.14: The bound-state exciton normalized oscillator strength OS_N as a function of the QD diameter d_{QD} when the regular complete basis (blue) and the simplified basis (red) are considered in the calculation. The DQD nanowire geometrical parameters are $l_{NW} = 90$ nm, $I = 2.8$ nm, and $h_{QD1} = h_{QD1} = 4$ nm.

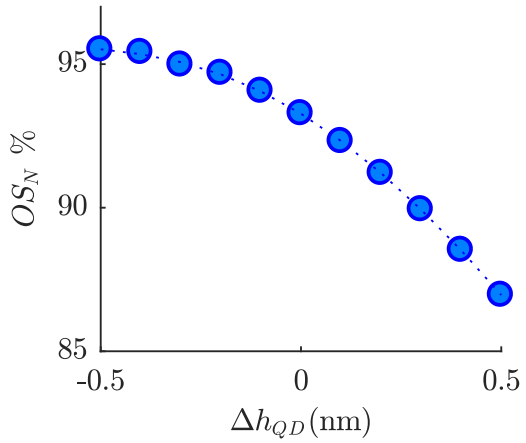

Figure 3.15: The bound-state exciton normalized oscillator strength OS_N as a function of the difference between the height of the two quantum dots in the DQD structure $\Delta h_{QD} = h_{QD2} - h_{QD1}$. The DQD nanowire geometrical parameters are $l_{NW} = 90$ nm, $I = 2.8$ nm, $d_{QD} = 36$ nm and $h_{QD1} = 4$ nm.

oscillator strength decreases by 6 %, while a height decrease by 0.5nm leads to an increase of the oscillator strength by 2 %.

Parameters	value
electron mass m_e^*	$0.067\, m_0$
heavy-hole mass m_h^*	$0.38\, m_0$
ΔE_c	400 meV
ΔE_v	215 meV
ϵ	12.9
E_g of GaAs	1.42 eV
electron in-plane parabolic potential $\hbar\omega_e$ for a nanowire of 80 nm diameter	20 meV
hole in-plane parabolic potential $\hbar\omega_h$ for a nanowire of 80 nm diameter	3.5 meV

Table 3.3: Type-I GaAs/AlGaAs QD material parameters [32].

3.5 Exciton states in type-I QDs in nanowires

Here, we consider type-I QDs in a nanowire. Computation is less demanding in this configuration in comparison to the type-II structure where there are many single-particle hole states in the valance band close in the energy which are contributing to the excitonic effects. In type-I QDs there are few single-particle electron and hole states confined inside the QD in the conduction and the valence band, respectively. We consider GaAs/AlGaAs type-I QDs in the calculation for which the material properties are listed in the Table. 3.3.

Figure 3.16 shows the OS_N versus the QD height. If we compare this figure to Fig. 3.7, we see significantly larger oscillator strength can be achieved in type-I SQD in comparison to the type-II SQD. We showed in Sec. 3.4.2 large oscillator strength comparable to the type-I structure can be achieved by engineering a type-II DQD nanowire.

As it is shown in Fig. 3.16, by increasing the QD height both the electron and the hole become more confined inside the dot and the wavefunctions' overlap becomes bigger and subsequently the OS will increase. On the other hand, by reducing the QD height, the electron and the hole wavefunction penetrate outside of the QD where the wavefunctions exponentially decreases and the overlap of the wavefunctions becomes smaller and as a result the oscillator strength reduces.

By increasing the QD height, the electron and the hole will get more space

to move around and get less attracted to each other. For this reason the binding energy (E_B) of the exciton as is shown in the Fig. 3.16 (b) reduces by increasing the QD height. When the QD height is much bigger then the exciton size in the z direction, the exciton is like an bulk exciton and its binding energy will be similar to the bulk exciton binding energy. Then in the limit where the QD height is big enough, we expect the binding energy reduces to the bulk exciton binding energy which is around 5 (meV) for the bulk GaAS exciton. Fig. (3.16) also shows that the E_B is reducing by increasing the QD height.

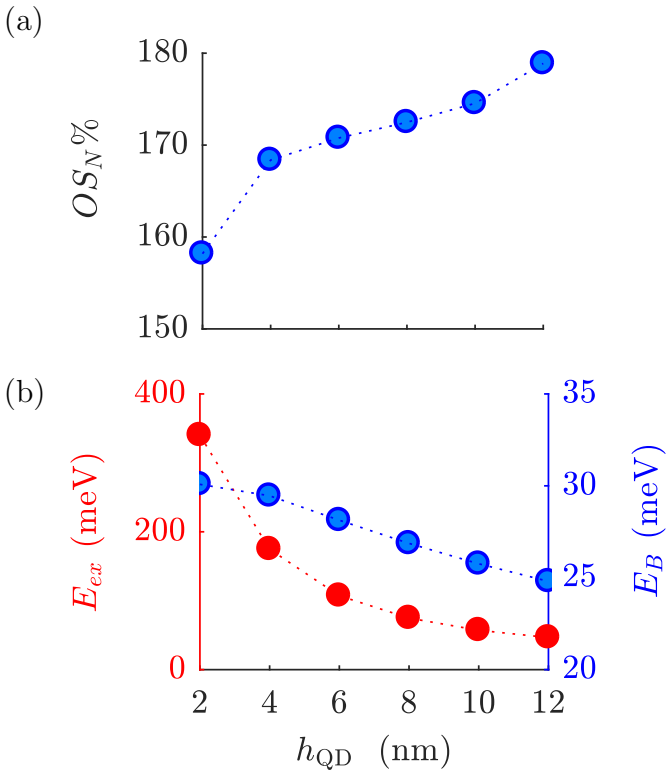

Figure 3.16: (a) Normalize ground-state exciton oscillator strength OS_N, (b) exciton energy E_{ex} and binding energy E_B as a function of the QD height h_{QD}. The geometrical parameters of the type-I SQD in a nanowire are: $l_{NW} = 60$ nm, $d_{QD} = 20$ nm.

Changing the length of the nanowire doesn't change the exciton properties of the type-I QD structure since it doesn't affect the single-particle electron and hole states which both are confined inside of the QD. The behavior of the exciton properties in type-I structure by increasing the QD diameter is similar

to the type-II QDs. By increasing the QD diameter, the exciton size increases in both cases, then the overlap integral in Eq. (3.15) has bigger value which results in a larger OS.

Fig. (3.17) shows the normalized oscillator strength OS_N in the lowest energy part in the presence and absence of the Coulomb interaction. As it can be seen, the Coulomb interaction has increased the ground-state exciton OS_N more than two times form 89.6% to 215%. As it was expected, this difference is not as big as the type-II configuration case which was discussed in Sec. 3.4.1, since the electron and the hole in the type-I configuration are confined also by the band structure potential profile and the Coulomb attraction makes them more confined. While in the type-II configuration the Coulomb attraction is the only potential which attaches the hole to the electron and it has more profound affect in this configuration in comparison to the type-I configuration. Including Coulomb interaction has also increased the energy difference between the ground-state exciton and the first excited-state exciton. Table 3.4 shows the important single-particle elements responsible for the ground-state exciton oscillator strength. We see unlike type-II QDs, here the ground-state exciton oscillator strength is mainly comes from the lowest-energy single-particle electron and hole states Φ_e^{100} and Φ_h^{100}. Table D.3 presents the forty lowest contributing single-particle elements which you can see for more detail about the single-particle components responsible for the ground-state exciton oscillator strength.

We also investigate the Coulomb effect in the type-I DQD nanowire. The exciton state in this structure depends on the I the distance between the QDs. The left column of the Fig. 3.18 shows the wavefunction of the ground-state uncorrelated electron-hole pair in the type-I DQD structure for four different values of I. We see in the all cases there is the same probability to find **(1)** both the electron and the hole in the right QD, **(2)** both the electron and the hole in the left QD, **(3)** the electron in the left QD and the hole in the right dot, and **(4)** the electron in the right QD and the hole in the left QD. The right column of the Fig. 3.18 shows the results when we have included the Coulomb interaction to calculate the ground-state exciton. We observe its more probable to find the correlated electron-hole pair (exciton) both in either the left QD or in the right QD (called direct exciton) than the electron

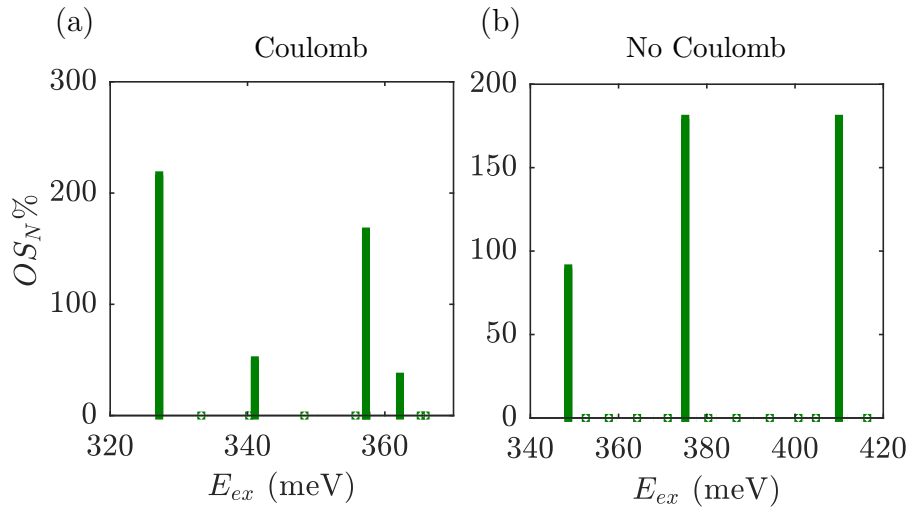

Figure 3.17: Normalized oscillator strength OS_N in the lowest-energy part (a) when the Coulomb interaction is been included and (b) in the absence of the Coulomb interaction. Type-I SQD in nanowire geometrical parameters are $l_{NW} = 60$ nm, $d_{QD} = 30$ nm, $h_{QD} = 2$ nm. After including CI: $E_{ex1} - E_{ex0} = 6.12$ (meV), before including CI: $E_{ex1} - E_{ex0} = 3.97$ (meV).

	$i := (n,l,m)_e$	$j := (n,l,m)_h$	R %
N_0	1,0,0	1,0,0	60.1 %
N_{17}	1,0,-1	1,0,1	10.1 %
N_{31}	1,0,1	1,0,-1	10.1 %
N_{49}	1,0,-2	1,0,2	2.9 %
N_{63}	1,0,2	1,0,-2	2.9 %

Table 3.4: Some of the single-particle states which are contributing to the ground-state exciton oscillator strength of a type-I SQD nanowire. The geometrical parameters of the structure are $l_{NW} = 60$ nm, $d_{QD} = 30$ nm, $h_{QD} = 2$ nm.

part of the exciton in the left QD and the hole part of the exciton in the right QD (called indirect exciton) or the other way around. It can also be seen in the Fig. 3.18, this probability increases by increasing the distance between the QDs such that in the last raw of the figure for which $I = 4$ (nm) the probability of finding indirect exciton is almost zero.

3.6 Validation of the results

There are very limited available theoretical and experimental works on type-II crystal-phase InP QDs [38, 28, 29]. Hence, our ability to validate our method

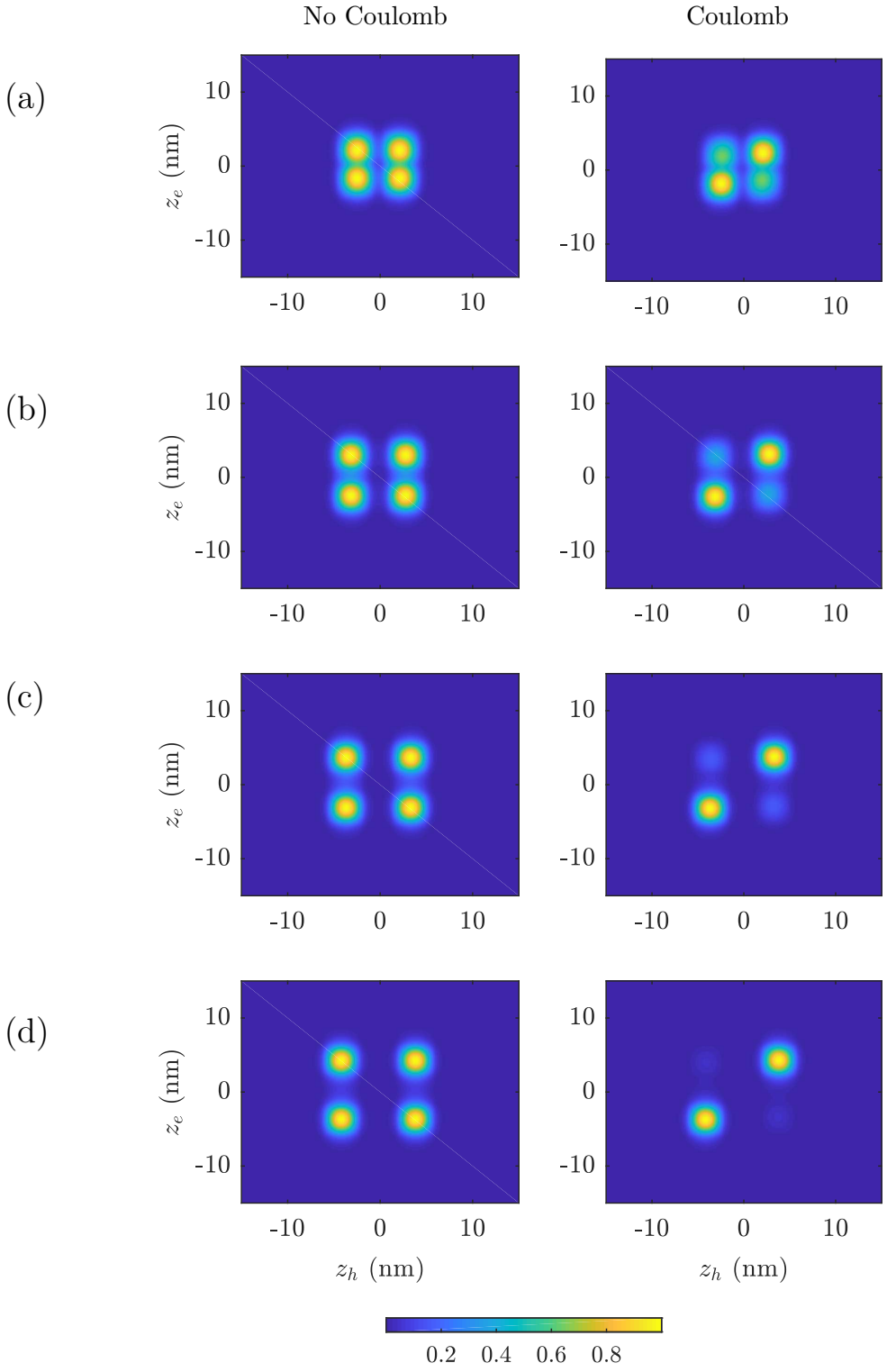

Figure 3.18: Ground-state exciton probability densities $|\Psi(\boldsymbol{r_e}, \boldsymbol{r_h})|^2$ when $R_e = R_h = 0$ in a type-I GaAs/AlGaAs DQD nanowire. The geometerical parameters of the DQD are: $d_{QD} = 20$ nm, $h_{QD1} = h_{QD2} = 4$ nm and (a) $I = 1$ nm, (b) $I = 2$ nm, (c) $I = 3$ nm, (d) $I = 4$ nm.

by comparison with available data is very limited. To overcome this problem, we have developed a formalization that can be used to verify some of our simulated results. Let us rewrite the exciton Hamiltonian:

$$H = \sum_{k=e,h} \Big(\frac{p_k^2}{2m_k^*} + \frac{1}{2} m_k \omega_k^2 R_k^2 + V_k(z) \Big) - \frac{e^2}{\epsilon \sqrt{(R_e - R_h)^2 + (z_e - z_h)^2}} \quad (3.17)$$

As discussed in Sec. 2.3, the first part of the right-hand side of Eq. (3.17) corresponds to the single-particle electron and hole Hamiltonian and the last term is the Coulomb Hamiltonian. Here, we consider the parabolic transverse potential as in Eq. (2.5). To simplify the above Hamiltonian, we use the center of mass and the relative motion coordinates as:

$$R = \frac{m_e^* R_e + m_h^* R_h}{M} \ , \quad \rho = R_e - R_h \quad (3.18)$$

where $M = m_e^* + m_h^*$ is the total mass of the exciton, and $\mu = m_e^* m_h^* / M$ the exciton reduced mass. Now, we define the relative momentum and the center of mass momentum as:

$$p = \frac{\hbar}{i} \nabla_\rho \ , \quad P = \frac{\hbar}{i} \nabla_R \quad (3.19)$$

by replacing (3.18) in (3.19) we have:

$$p_e = p + P \frac{m_e}{M} \ \ p_h = -p + P \frac{m_h}{M} \quad (3.20)$$

By substituting (3.20) and (3.18) in (3.17) and by considering $\omega_h = \alpha \omega_e$ (α is constant):

$$\begin{aligned} H = {} & \frac{P^2}{2M} + \frac{1}{2}(m_e + \alpha^2 m_h)\omega_e^2 R^2 + \frac{p^2}{2\mu} + \frac{1}{2}\frac{\mu(m_h + \alpha^2 m_e)}{M}\omega_e^2 \rho^2 \\ & + 2\mu(1 - \alpha^2)\omega_e^2 \rho R + \frac{p_{z_e}^2}{2m_e} + \frac{p_{z_h}^2}{2m_h} + V_e(z_e) + V_h(z_h) - \frac{e^2}{\epsilon \sqrt{\rho^2 + (z_e - z_h)^2}} \end{aligned} \quad (3.21)$$

We assume that $\alpha = 1$ in the above equation which means $\omega_h = \omega_e = \omega$. This is a rough approximation as ω_e is a few times bigger than the ω_h [32]. However, this assumption is adopted here to find a solution to (3.21). It's the main reason that why this method is not a general method to solve the exciton problem. By this assumption, the above Hamiltonian simplifies to:

$$H = \frac{P^2}{2M} + \frac{1}{2} M \omega^2 R^2 + \frac{p^2}{2\mu} + \frac{1}{2}\mu\omega^2 \rho^2 + \frac{p_{z_e}^2}{2m_e} + \frac{p_{z_h}^2}{2m_h} + V_e(z_e) + V_h(z_h) - \frac{e^2}{\epsilon \sqrt{\rho^2 + (z_e - z_h)^2}} \quad (3.22)$$

Now, the center of mass part and electron-hole relative motion part are separable such that $H = H_R + H_{z_e,z_h,\rho}$ and the exciton wavefunction can be written as:

$$\Psi(z_e, z_h, R, \rho) = \phi(R)\phi(z_e, z_h, \rho) \tag{3.23}$$

where $\phi(R)$ is the wavefunction of a harmonic oscillator of Hamiltonian

$$H_R = \frac{P^2}{2M} + \frac{1}{2}M\omega^2 R^2 \tag{3.24}$$

with eigenenergies of $E_R = \hbar\omega(n + \frac{1}{2})$. $\phi(z_e, z_h, \rho)$ in (3.23) is the eigenstate of the Hamiltonian

$$H_{z_e,z_h,\rho} = \frac{p^2}{2\mu} + \frac{1}{2}\mu\omega^2\rho^2 + \frac{p_{z_e}^2}{2m_e} + \frac{p_{z_h}^2}{2m_h} + V_e(z_e) + +V_h(z_h) - \frac{e^2}{\epsilon\sqrt{\rho^2 + (z_e - z_h)^2}} \tag{3.25}$$

This three-variable partial differential equation can be solved with different tools. We used COMSOL finite-element-method. By solving this equation we find the exciton energy and wavefunction in SQD and DQD type-I and type-II structures.

In this method of solving Schrödinger equation, we assumed a parabolic potential in the transverse direction but, as we discussed in Sec. 2.2.1, it is not a realistic assumption, whereas the infinite potential well is a more realistic description of the structures. However, we cannot solve the Hamiltonian (3.17) by considering an infinite well in the transverse direction. For this reason, the method developed here is restricted to the parabolic transverse potential, which limits the practicability of this method for calculating the exciton state.

For a type-II InP crystal-phase SQD nanowire, we calculate the ground-state exciton energy corresponding to the relative motion of the electron-hole pair to be 119.2 meV which is the lowest eigenvalue of the Hamiltonian (3.25). By adding the center of mass energy of 60 meV, corresponding to the lowest eigenvalue of (3.24), the total energy of the exciton (excluding band gap energy) is 179 meV which perfectly matches the result obtained by using the configuration-interaction method. In both methods, we considered the equal in-plane parabolic potentials for the electron and hole as $\hbar\omega_e = \hbar\omega_h = \hbar\omega =$ 60 meV. Figs. 3.19 (a) and (b) show the exciton wavefunction in the z and in the relative motion ρ coordinates, respectively. Here, we observe the same effect of the Coulomb interaction which we had seen previously by using the

configuration-interaction method. The Coulomb interaction makes the hole state attached to the electron around the QD.

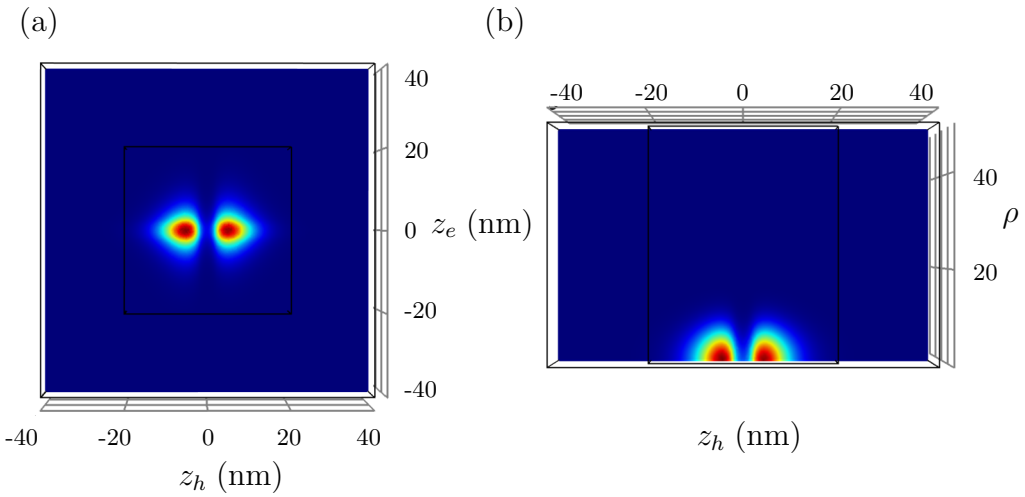

Figure 3.19: Ground-state exciton wave function in a type-II InP crystal-phase QD nanowire when (a) $\rho = 0$ and (b) $z_e = 0$. The geometrical parameters of the structure are: $h_{QD} = 4$ nm, $l_{NW} = 80$ nm, $d_{QD} = 50$ nm. In this calculation we considered a parabolic transverse potential with $\hbar\omega_e = \hbar\omega_h = 60$ meV.

3.7 Summary

By using an efficient method based on the configuration-interaction description of the exciton state, we analyzed the main properties of excitons in type-I and type-II single and double quantum dots in nanowires.

First, we examined the convergence of the method. For calculating the 5-variable Coulomb integral, we need to discretize the variables which should be done very carefully. Also, the exciton state is expanded on the single-particle states. We need to consider enough single-particle states to represent exciton state with a good accuracy. This depends on the QD and the nanowire size. We calculated and analyzed the energy spectra, oscillator strengths, and electron and hole exciton sizes as a function of the all relevant geometrical parameters. In type-II SQD nanowire, we showed the Coulomb interaction is sufficient to bind the hole part of the exciton to the QD in a single-quantum dot geometry, such that the exciton properties become insensitive to the length for nanowire lengths larger than the exciton size. However, in the single-quantum

dot geometry the oscillator strength of the ground-state exciton is significantly reduced compared to a type-I system. While the oscillator strength of the exciton transition in a single-quantum dot in the limit of infinitely small QD height increases, the exciton is not spatially confined to the QD and thus not suitable for quantum gate applications. We have then proposed a double-quantum dot structure for which the exciton oscillator strength can be increased to more than four times its value compared to that of a single-quantum dot nanowire while the exciton remains well-confined to the double-quantum dot region. This structure featuring a combination of separated electron and hole localization and a large exciton oscillator strength represents a promising platform for implementing two-qubit quantum gates.

Although the type-I QDs are studied extensively, but there is still some interesting new features which we brought in this chapter.

In the last section, we validated the calculation results of the configuration-interaction method. By assuming an equal transverse parabolic potential for the electron and the hole, we could reduce the 6-dimensional exciton Schrödinger equation to a 3-dimensional equation. Then, we solved the 3-dimensional partial differential equation by using finite-element-method in COMSOL. The result was perfectly matching with the results from the configuration-interaction method.

CHAPTER 4

Quantum gates

Troiani et al. [19] proposed to use the spin of an excess electron in a type-I DQD as a qubit realization. In their laterally arranged DQD array, qubits are manipulated by means of the all-optical STIRAP technique. As I explained in Chapter 2, STIRAP is an efficient method for transferring populations adiabatically between two discrete quantum states by coupling them using two radiation fields via an intermediate state which is usually a radiatively decaying state [81, 80]. When the adiabatic condition is fully satisfied, the evolution of the system is robust with respect to control parameter variations such as the laser intensity, the pulse timing and the pulse shape. This property has made STIRAP a popular tool in optical quantum information processing [104, 105, 106]. The coupling can be optically turned on and off, so that single- and two-qubit operations can be selectively chosen as required in a scalable quantum computation scheme [1]. However, the charged exciton state of the type-I DQD, used as the intermediate state in the proposed scheme in Ref. [19], does not allow for good overlap between the hole and both electron wave functions simultaneously. This simultaneous coupling is essential for implementing high-fidelity quantum gates by means of the STIRAP gating technique.

On the other hand, the type-II band structure allows for the possibility of good overlap between electrons of neighboring QDs with a common hole state. We showed in the previous chapter that the otherwise weak transition

strength of the exciton of a crystal-phase type-II QD in an InP nanowire can be increased by implementing a DQD structure leading to an improved overlap between the electron and hole parts confined inside the QD and the barrier, respectively.

The single-qubit rotation by using STIRAP technique [107] (briefly presented in Sec. 4.2) was developed in 2002. Type-I DQD configurations to implement single- and two- qubit rotations by using STIRAP have also been introduced before [19]. Our contribution here is that we show how to overcome the limitations of the scheme in Ref. [19] by using the novel type-II DQD-in-a-nanowire system instead of the conventional type-I configuration. By calculating the transition dipole moments, we quantitatively illustrate type-II QDs are significantly better than type-I QDs for quantum gating by STIRAP. By developing a multiband formalism we show that a charged-exciton featuring a *mixed-hole* part acting as an intermediate state provides essential coupling with three ground-states of a DQD to perform qubit rotations by STIRAP. We then introduce a system consisting of two neighboring DQDs in a nanowire each encoding one qubit. By using the configuration-interaction method, we show that the strong Coulomb interaction between the charges, which causes a significant shift of the STIRAP transition frequencies, can be exploited to efficiently perform high fidelity conditional two-qubit CNOT operation on the two qubits. Importantly, we also show that the implementation is robust against the decoherence posed by spin and charge fluctuations in the environment.

The chapter is organized as follows. First, we compare the STIRAP gating in a three-level system of a type-I DQD with a type-II DQD. The basic theory of the single-qubit rotation is presented. Then, we show how to provide a four-level scheme in a type-II DQD necessary for single-qubit rotations. Next, we illustrate the scheme for implementing CNOT gate in a two-DQD system. We calculate the fidelity of the single- and two-qubit gates and evaluate their robustness against the charge and spin noises.

4.1 Physical implementation of the three-state STIRAP in type-II double-quantum-dot

We consider ultra-clean crystal-phase type-II DQD nanowire shown schematically in Fig. 3.8 (a) as a platform for the optical quantum gating scheme. As we explained in the previous chapter, in these structures, the single-particle electron states reside inside the QDs. We consider the QDs with different heights such that $h_{QD1} \neq h_{QD1}$ to have two localized electron states in the QDs with different energy levels, as it is shown in Fig. 4.1. The spatial overlap of the electron ground-states of the individual QDs must be negligible to suppress tunneling between electron states during gate operations. I also described in Chapter 3, most single-particle hole states are predominantly localized in the outer nanowire regions surrounding the DQD. However, there are a few single-particle hole states which are mainly localized inside the barrier region between two QDs [cf. Fig. 3.10]. We are particularly interested in this hole state confined inside the barrier since the corresponding exciton has promising features for application in quantum computing by means of the STIRAP process.

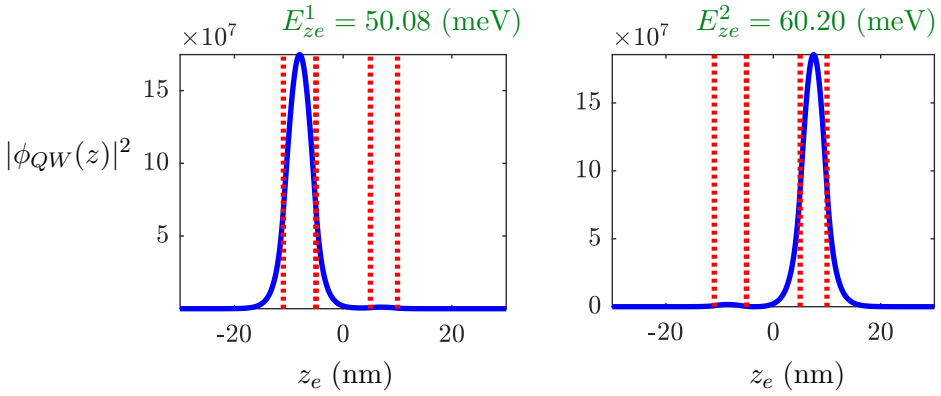

Figure 4.1: Single-particle electron probability densities $|\phi_{QW}(z)|^2$ in an asymmetric type-II DQD nanowire. The geometrical parameters of the structure are: $h_{QD1} = 6$ nm, $h_{QD2} = 5$ nm, $l_{NW} = 60$ nm, $d_{QD} = 20$ nm and $I = 10$ nm.

Figure 4.2 shows the STIRAP scheme between two electron states $|e_1\rangle$ and $|e_2\rangle$ of a DQD in a type-I and in a type-II configurations. The interconnecting state in both cases is a charged exciton state $|X^-\rangle$, i.e., an electron-hole

complex consisting of one electron in each QD and a single hole. Initially, the entire population is in the single-electron ground-state $|e_1\rangle$ of QD_1. The pump pulse induces the transition between the states $|e_1\rangle$ and $|X^-\rangle$, and the Stokes pulse enables the transition between the states $|X^-\rangle$ and $|e_2\rangle$, where $|e_2\rangle$ is the single-electron ground-state of QD_2. The coupling strengths of the pump P and Stokes S transitions are defined by the Rabi frequencies $\Omega_P(t) = d_P\mathcal{E}_P(t)/\hbar$ and $\Omega_S(t) = d_S\mathcal{E}_S(t)/\hbar$ with transition dipole moments $d_{P,S}$ and electric field of the lasers $\mathcal{E}_{P,S}(t)$.

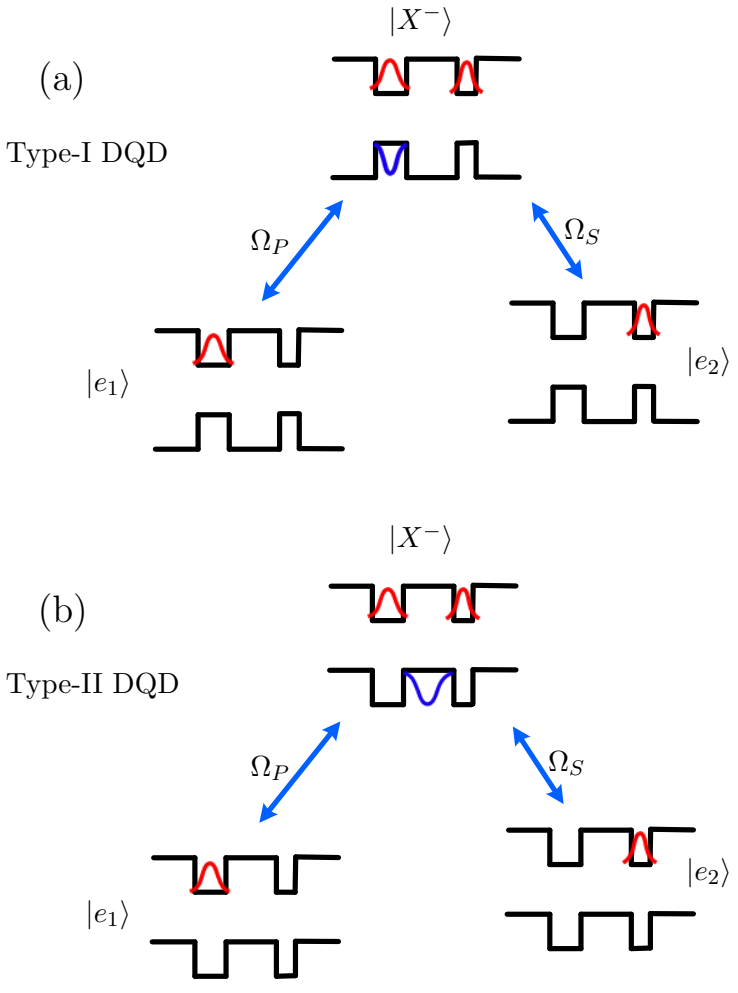

Figure 4.2: The STIRAP level scheme and electron/hole wave functions in (a) type-I and (b) type-II DQDs.

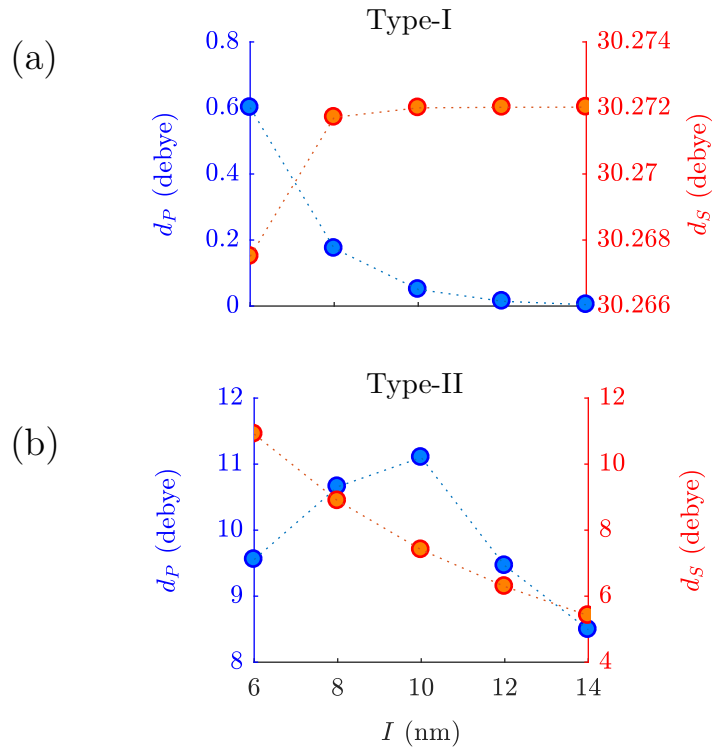

Figure 4.3: Transition dipole mements d_P and d_S in (a) type-I GaAs/AlGaAs DQD in a nanowire (b) type-II crystal-phase InP DQD in a nanowire. Geometerical parameters of the structure: $h_{QD1} = 5$ nm, $h_{QD2} = 3$ nm, $d_{QD} = 40$ nm, and $l_{NW} = 70$ nm..

As illustrated in the Fig. 4.2 (a), while the overlap between the hole and electron wave functions in the left dot is large in the type-I configuration, the overlap between the electron in the right dot and the hole in the left dot is very small. Figure 4.3 (a) shows the calculated d_P and d_S for a type-I GaAs/AlGaAs DQD in a nanowire as a function of I the distance between the QDs [cf. Fig 3.8 (a)]. The dipole moments calculation detail is presented later in this chapter and the material parameters used in the calculation are listed in Table 3.3. As we observe in this figure, the dipole moment d_P which is proportional to the overlap between $|e_1\rangle$ and $|X^-\rangle$ is nearly zero and the intermediate state $|X^-\rangle$ couples very weakly to $|e_1\rangle$. For this reason, the STIRAP gating scheme in the type-I DQD configuration is highly inefficient. On the other hand, as shown in Fig. 4.2 (b), the hole in the type-II configuration

is localized in the barrier region between the QDs and thus overlaps with the electrons of both QDs. Figure 4.3 (b) shows the calculated d_P and d_S in a type-II crystal-phase InP DQD in a nanowire as a function of the distance between the QDs I. As we see in this figure, while the dipole moment d_S is not as large as that of the type-I configuration, the magnitudes of the overlaps between the hole and the right electron proportional to d_P and the hole and the left electron proportional to d_S are similar. This property leads to Rabi frequencies Ω_P and Ω_S of similar magnitudes and represents a major asset of the type-II configuration.

4.2 Single-qubit rotation by stimulated Raman adiabatic passage

Here, we shortly present the basic theory of the single-qubit rotation. This is developed by Z. Kis, and F. Renzoni [107] in 2002. They showed in a four-level system shown in Fig. 4.4 any arbitrary rotation with the axis and angle of the rotation being uniquely defined by the parameters of the laser pulses is possible. In their scheme three ground-states $|1\rangle$, $|2\rangle$, and $|3\rangle$ are coupled via a single excited-state $|e\rangle$ by different laser fields. Each laser field drives only one transition, due to their polarizations and/or frequencies. The ground-states $|1\rangle$ and $|2\rangle$ define the qubit, while the state $|3\rangle$ is an auxiliary state that will be occupied only in the intermediate phase of the rotation procedure. In [107], it has been assumed that the detunings of the three laser fields are the same, i.e. the system is in a multi-photon resonance such that $\Delta_0 = \Delta_1 = \Delta_2 = 0$. They have also assumed $d_0 = d_1 = d_2 = 1$, and the pump pulses $\mathcal{E}_0(t) = \mathcal{E}_P(t)\cos\chi$ and $\mathcal{E}_1(t) = \mathcal{E}_P(t)\sin\chi\exp(i\eta)$, couple $|0\rangle$ and $|1\rangle$ to $|e\rangle$, respectively. Here, $\mathcal{E}_P(t) = A_P\exp(-t/\tau)^2$ and χ and η are phase factors defined by the desired gate operation. The Stokes pulse $\mathcal{E}_2(t) = A_2\exp(-(t+\Delta T)/\tau)^2$ couples $|2\rangle$ to $|e\rangle$. $\mathcal{E}_P(t)$ and $\mathcal{E}_2(t)$ are Gaussian shaped laser pulse envelops with ΔT time separation between the maxima of the pulses and the pulse width of $\tau/\sqrt{2}$.

The Hamiltonian $H(t)$ of this four-state system in the rotating-wave ap-

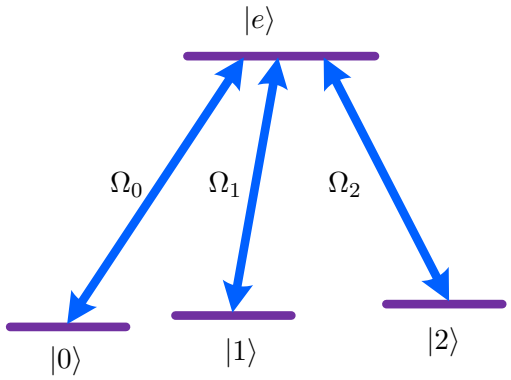

Figure 4.4: Interaction scheme for the rotation of a qubit by STIRAP. The three ground-states $|0\rangle$, $|1\rangle$, and $|2\rangle$ are coupled to the excited state $|e\rangle$ by three different laser fields. The qubit is defined by the ground states $|0\rangle$ and $|1\rangle$. State $|2\rangle$ is an auxiliary state occupied only in the intermediate phase of the rotation procedure.

proximation RWA is given by:

$$H(t) = \hbar\Delta \left|e\right\rangle \left\langle e\right| + \frac{\hbar}{2}\Big(\Omega_0(t) \left|0\right\rangle \left\langle e\right| + \Omega_1(t) \left|1\right\rangle \left\langle e\right| + \Omega_2(t) \left|2\right\rangle \left\langle e\right| + H.c.\Big) \tag{4.1}$$

The qubit rotation procedure in this four-level system is implemented by using two STIRAP process as follows:

Step1 In the first STIRAP, the fields 0 and 1 are the pump fields, whereas the field 2 plays the role of the Stokes field. The pulses are applied in the counter-intuitive order, i.e., the Stokes pulse arrives before the pump ones. The pump fields 0 and 1 define a dark (or non-coupled) state:

$$\left|D\right\rangle = -\sin\chi \left|0\right\rangle + e^{i\eta}\cos\chi \left|1\right\rangle \tag{4.2}$$

in the subspace spanned by the states $|0\rangle$, $|1\rangle$. The orthogonal state (the coupled or bright state) $|C\rangle$ is:

$$\left|C\right\rangle = \cos\chi \left|0\right\rangle + e^{-i\eta}\sin\chi \left|1\right\rangle \tag{4.3}$$

from which the population can be transferred to the state $|2\rangle$ if all the three fields are on. By decomposing the initial superposition $|i\rangle$ onto $|D\rangle$ and $|C\rangle$:

$$\left|i\right\rangle = \left\langle D|i\right\rangle \left|D\right\rangle + \left\langle C|i\right\rangle \left|C\right\rangle \tag{4.4}$$

with

$$\begin{aligned} \langle D|i\rangle &= -\alpha \sin\chi + \beta e^{-i\eta}\cos\chi \\ \langle C|i\rangle &= \alpha \cos\chi + \beta e^{-i\eta}\sin\chi \end{aligned} \tag{4.5}$$

The Hamiltonian operator of Eq. (4.1) is written as:

$$\hat{H}(t) = \hbar\Delta \left|e\right\rangle \left\langle e\right| + \frac{\hbar}{2}\Big(\Omega_P(t) \left|C\right\rangle \left\langle e\right| + \Omega_2(t) \left|2\right\rangle \left\langle e\right| + H.c.\Big) \tag{4.6}$$

In fact the Hamiltonian (4.6) describes an ordinary STIRAP process in a three-level system. It can be easily shown that in the adiabatic limit the system is left, after the first pulse sequence, in the superposition of the three ground-states:

$$|\psi\rangle = \langle D|i\rangle \left|D\right\rangle - \langle C|i\rangle \left|2\right\rangle \tag{4.7}$$

without populating the excited state during the evolution. We recognize in Eq. (4.7) that the component of $|i\rangle$ along the noncoupled state $|D\rangle$ is untouched, whereas the orthogonal bright component is transferred to the target state $|2\rangle$.

Step2 The second step of the rotation procedure is a reverse STIRAP process that maps the state $|2\rangle$ back to the qubit subspace. The phase of the field 2 is shifted by ζ in comparison to the field 2 in the first STIRAP. The pulses are applied in the reverse order with respect to the first step of the rotation procedure: the pulses 0 and 1 which play now the role of the Stokes pulses! arrive before the pulse 2 the pump. The fields 0 and 1 have the same Rabi frequencies and the same phases as in the first step of the procedure. In this way, the state $|\psi\rangle$ prepared by the first STIRAP process, Eq. (4.7), is initially a dark state for the three laser pulses because: (1) the state $|2\rangle$ is initially not coupled (counter-intuitive pulse order); (2) the state $|\psi\rangle$ has no component along $|C\rangle$, therefore it is decoupled from the fields 0 and 1. The darkness of $|\psi\rangle$ allows the implementation of the second STIRAP process although all the ground-states are initially populated. In this process, the state $|2\rangle$ is transferred back to the qubit subspace. More precisely, it will be mapped on the coupled state $|C\rangle$ because the state $|D\rangle$ is a decoupled state also in this second STIRAP process. The component of the initial qubit $|i\rangle$ along the non-coupled state $|D\rangle$ and the new component obtained by mapping

back the state $|2\rangle$ will differ by a phase of ζ. Clearly, for $\zeta = 0$ the system goes back to the initial state $|i\rangle$. In a similar calculation that yielded Eq. (4.7), it can be shown that in the adiabatic limit the component of $|\psi\rangle$ along $|2\rangle$ is mapped back onto the input subspace such that:

$$\langle 2|\psi\rangle\,|2\rangle \rightarrow e^{-i\zeta}\langle 2|\psi\rangle\,|C\rangle \tag{4.8}$$

so the final state becomes:

$$|f\rangle = \langle D|i\rangle\,|D\rangle + e^{-i\zeta}\langle C|i\rangle\,|C\rangle \tag{4.9}$$

By substituting the expressions (4.5) for the coefficients in Eq. (4.9) we obtain the single-qubit rotation around the $\mathbf{n} = (\sin 2\chi \cos\eta, \sin 2\chi \sin\eta, \cos 2\chi)$ axis by an angle ζ:

$$|f\rangle = e^{-i\zeta/2} R_{\mathbf{n}}(\zeta)\,|i\rangle\,, \tag{4.10}$$

where $R_{\mathbf{n}} = e^{-i\frac{\zeta}{2}\boldsymbol{n}.\hat{\boldsymbol{\sigma}}}$ is the rotation operator and $\hat{\boldsymbol{\sigma}} = (\sigma_x, \sigma_y, \sigma_z)$ are the Pauli operators. In the single-qubit rotation (4.10), $-\zeta/2$ appears in the output as a global phase which may be incorporated into the algorithm being implemented on the quantum computer [107].

Fig. 4.5 shows the time evolution of the laser fields and the populations of the four-level states of the STIRAP scheme for implementing a single-qubit NOT operation around the x axis which mathematically is a rotation around $\boldsymbol{n} = (1, 0, 0)$ axis by an angle π. Here, the initial state of the system is $0.5\,|0\rangle + 0.866\,|1\rangle$, as an example. By choosing appropriate values for χ, η, and ζ which control the pump and the Stokes laser pulses relative amplitude and phase, any arbitrary single-qubit rotation can be performed. Other STIRAP parameters ΔT, τ, and $\mathcal{E}_{\mathcal{P},\mathcal{S}}$ are chosen such that the adiabatic condition Eq. (2.34) is met. Also, in this example I chose laser pulses of a few hundreds of GHz amplitude to perform the operation in a few tenths of nanosecond. The operation time can be reduced or increased by respectively increasing and decreasing the laser pulses intensity.

In the next section, we explain our proposed type-II DQD nanowire as a hardware to implement the single-qubit rotation discussed in this section.

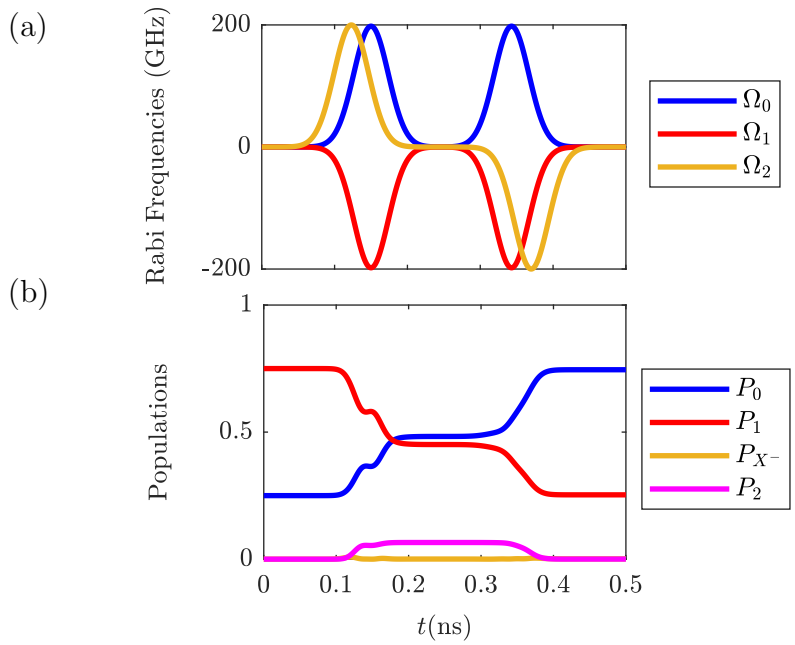

Figure 4.5: The time evolution of the (a) laser fields and (b) the four-level states' population in a single-qubit NOT operation around the x axis. The initial state is $0.5\,|0\rangle + 0.866\,|1\rangle$ and the parameters used in this calculation: $\chi = -\pi/4$, $\eta = 0$, $\zeta = \pi$, $\tau = 33.5$ ps, $\Delta T = 27$ ps, $\Delta_0 = \Delta_1 = \Delta_2 = 0$, $d_P = d_S = 1$, $A_P = 282$ and $A_2 = 200$ GHz.

4.2.1 Physical implementation of the four-state system in a type-II double-quantum-dot

We initially consider a single electron in QD_1 of the DQD structure. By applying a uniform magnetic field B in the Voigt configuration along the x axis, the electron spin states $\left|S_x = \pm\frac{1}{2}\right\rangle$ are split by $\mu_B g_e B$ the Zeeman effect as shown in Fig. 4.6. Here, μ_B is the Bohr magneton and g_e is the electron spin g factor. The electron eigenstates used to encode the logical qubit of the DQD are then direct products of the electron position and the spin degrees of freedom given by:

$$|0\rangle = |f_{e1}\rangle \otimes \left|S_x = +\frac{1}{2}\right\rangle, \quad |1\rangle = |f_{e1}\rangle \otimes \left|S_x = -\frac{1}{2}\right\rangle, \tag{4.11}$$

where $|f_{e1}\rangle$ is the ground-state electron envelope function in QD_1.

As it was discussed in the previous section, in a system featuring three ground-states coupled to an excited-state, an arbitrary single-qubit rotation

can be performed using two STIRAP processes. In the DQD configuration, we use the state $|2\rangle$ defined as:

$$|2\rangle = |f_{e2}\rangle \otimes \left| S_x = -\frac{1}{2} \right\rangle, \tag{4.12}$$

together with the states $|0\rangle$ and $|1\rangle$ defined in Eq. (4.11) as the three ground-states of the single-qubit rotation scheme. $|f_{e2}\rangle$ in Eq. (4.12) is the ground-state electron envelope function in QD_2 of the DQD.

The excited state allowing optical coupling between the input space $\alpha|0\rangle + \beta|1\rangle$ and the state $|2\rangle$ is a negatively charged-exciton state $|X^-\rangle$ as shown in Fig. 4.6. Band mixing is heavy in QDs and the effective $\mathbf{k}$ point is located at a finite Γ point, substantially away from the Γ point, such that the charged exciton's hole part is a mixed-state. Due to this mixing, as we show in the next section, the charged exciton state couples with all the electron states $|0\rangle$ and $|1\rangle$ in QD_1 and $|2\rangle$ in QD_2. The coupling strength of the charged exciton state to $|0\rangle$, $|1\rangle$, $|2\rangle$ depends on the bulk transition matrix elements M and the overlap of the envelope functions as explained in Sec. 3.2.

The differences between the laser frequencies and the corresponding transition frequencies, we denote by Δ_0, Δ_1 and Δ_2, then defining the single-photon detuning as $\Delta \equiv \Delta_0$ and two-photon detunings as $\delta_1 \equiv \Delta_1 - \Delta_0$, $\delta_2 \equiv \Delta_2 - \Delta_0$ [cf. Fig. 4.6]. The Hamiltonian describing the coupling of the four states $\{|0\rangle, |1\rangle, |X^-\rangle, |2\rangle\}$ using three coherent radiation fields within the rotating wave approximation is then given by:

$$H(t) = \frac{\hbar}{2} \begin{bmatrix} 0 & 0 & \Omega_0 & 0 \\ 0 & 2\delta_1 & \Omega_1 & 0 \\ \Omega_0^* & \Omega_1^* & 2\Delta & \Omega_2^* \\ 0 & 0 & \Omega_2 & 2\delta_2 \end{bmatrix}, \tag{4.13}$$

The derivation of this Hamiltonian is similar to the Hamiltonian in Eq. (2.19) explained in Appendix B. As discussed in the Sec. 2.4.3, the STIRAP transfer efficiency depends differently on δ_1, δ_2 and Δ: STIRAP in a four-level system is sensitive to the magnitude of the two-photon detunings δ_1 and δ_2 as the formation of the dark state requires two-photon resonances $\delta_1 = \delta_2 = 0$. On the other hand, the formation of the dark state is not prevented by a non-zero single-photon detuning Δ.

One of the interesting aspects of the STIRAP in the four-level scheme of the Fig. 4.6 is that with a specific choice of the laser parameters ($\chi = -\pi/2$ and $\eta = 0$), the information stored in the electron spin is mapped to the position degree of the freedom. Fig. 4.7 shows that the initial spin qubit $1/\sqrt{2}\{|0\rangle + |1\rangle\}$ is mapped to the position qubit $1/\sqrt{2}\{|0\rangle + |2\rangle\}$ at the end of the first STIRAP ($t = 0.25$ ns). By considering $\zeta = 0$ and the same values as the first STIRAP for the χ and η the position qubit maps back to the spin qubit at the end of the second STIRAP ($t = 0.5$ ns) as we see in Fig. 4.7.

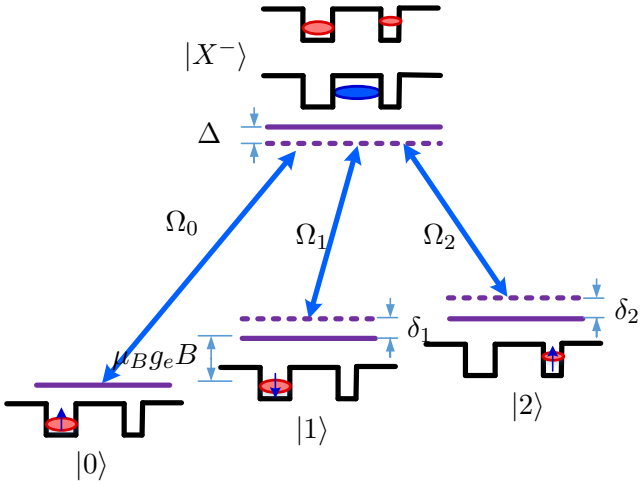

Figure 4.6: The interaction scheme for manipulating the spin of an electron by STIRAP in the DQD structure. The qubit is defined by the ground states $|0\rangle$ and $|1\rangle$. The states $|2\rangle$ and $|X^-\rangle$ are auxiliary states occupied only in the intermediate phase of the gating procedure. Ω_0, Ω_1, and Ω_2 are the Rabi frequencies of the transitions, Δ and $\delta_{1,2}$ are respectively single- and two-photon detunings defined in the main text.

4.2.2 Charged-exciton state

Here, to evaluate the transitions dipole moment of the charged-exciton state to the ground states, we introduce a full multi-band formalism taking into account band-mixing effects. This formalism is compatible with methods such as **k.p** theory, empirical tight-binding, and ab-initio which allow for accurate modeling of the many-particle states in QDs by taking into account detailed electronic band structures.

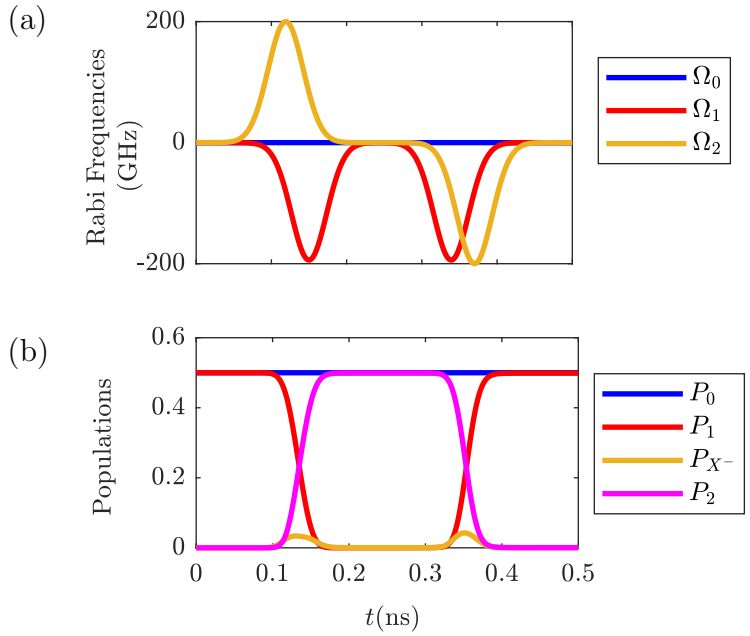

Figure 4.7: Time evolution of the (a) pulse sequences and the (b) four-level Λ system populations during two STIRAPs. The first STIRAP maps the spin qubit to the position qubit. The second STIRAP maps the position qubit back to the spin qubit. In this calculation, I considered $\chi = -\pi/2$, $\eta = 0$, $\zeta = 0$, $\Delta = 10$ GHz, $\delta_1 = \delta_2 = 0$, $d_P = d_S = 1$, $A_P = 194$ GHz, $A_2 = 200$ GHz, $\Delta T = 31$ ps, $\tau = 33$ ps.

First we write the charged-exciton state $|X^-\rangle$ which couples the input state $\alpha|0\rangle + \beta|1\rangle$ to $|2\rangle$ in the electron picture as a Slater determinant of a set of single-particle wave functions:

$$\begin{aligned} |X^-\rangle = \mathcal{A}\{\alpha|\uparrow, u_s, f_{e1}\rangle + \beta|\downarrow, u_s, f_{e1}\rangle, |\uparrow, u_s, f_{e2}\rangle, \\ |\psi_{v1}\rangle, ..., |\psi_{v(m-1)}\rangle, |\psi_{v(m+1)}\rangle, ..., |\psi_{vn}\rangle\}, \end{aligned} \tag{4.14}$$

where $|\alpha|^2 + |\beta|^2 = 1$ and $\mathcal{A}$ is the anti-symmetrization operator which we drop henceforth for simplicity. Each state vector in (4.14) contains three parts: a spin part, a Bloch function part and an envelope function part. The conduction band envelope function is denoted by f_e. Since the conduction band has a s-like atomic function symmetry, its Bloch function is denoted by u_s. $|\psi_{vi}\rangle$ is the ith valence subband; where $i = 1, .., n$ with $n \neq m$ such that the valence band is occupied by all electron states except the m^{th} state. The three upper valence bands are written as a linear combination of Bloch

functions u_x, u_y, u_z of the atomic p-like symmetry x, y and z, respectively [52]. A general valence state $|\psi_v\rangle$ can then be written as

$$\begin{aligned}|\psi_v\rangle = C_1\left|\uparrow, u_x, f_h^1\right\rangle + C_2\left|\downarrow, u_x, f_h^2\right\rangle + C_3\left|\uparrow, u_y, f_h^3\right\rangle \\ +C_4\left|\downarrow, u_y, f_h^4\right\rangle + C_5\left|\uparrow, u_z, f_h^5\right\rangle + C_6\left|\downarrow, u_z, f_h^6\right\rangle,\end{aligned} \tag{4.15}$$

where C_i are the expansion coefficients and f_h^i with $i = 1, .., 6$ are the hole envelope functions which form a complete orthonormal set and can be considered approximately constant over a unit cell. The states $|0\rangle$, $|1\rangle$ and $|2\rangle$ of the STIRAP scheme in the electron picture are written as

$$\begin{aligned}|0\rangle &= |\uparrow, u_s, f_{e1}\rangle, |\psi_{v1}\rangle, |\psi_{v2}\rangle, ..., |\psi_{vn}\rangle \\ |1\rangle &= |\downarrow, u_s, f_{e1}\rangle, |\psi_{v1}\rangle, |\psi_{v2}\rangle, ..., |\psi_{vn}\rangle \\ |2\rangle &= |\uparrow, u_s, f_{e2}\rangle, |\psi_{v1}\rangle, |\psi_{v2}\rangle, ..., |\psi_{vn}\rangle,\end{aligned} \tag{4.16}$$

where the valence band is fully occupied by electrons. The transition matrix element between the input state $\alpha|0\rangle + \beta|1\rangle$ and $|X^-\rangle$ is now given by:

$$\begin{aligned}\left(\alpha\langle 0| + \beta\langle 1|\right)\mathbf{e}\cdot\hat{\mathbf{d}}\left|X^-\right\rangle = \langle\psi_{vm}|\,\mathbf{e}\cdot\hat{\mathbf{d}}\,|\uparrow, u_s, f_{e2}\rangle \\ = C_1 e_x M_x\langle f_h^1|f_{e2}\rangle + C_3 e_y M_y\langle f_h^3|f_{e2}\rangle + C_5 e_z M_z\langle f_h^5|f_{e2}\rangle,\end{aligned} \tag{4.17}$$

where $M_i = \langle u_i|\,\hat{d}_i\,|u_s\rangle\,; (i = x, y, z)$ is the bulk matrix element, $\mathbf{e} = (e_x, e_y, e_z)$ is the unit vector of the laser light and $\hat{\mathbf{d}}$ is the momentum operator. In the ZB region $\langle u_x|\,\hat{d}_x\,|u_s\rangle = \langle u_y|\,\hat{d}_y\,|u_s\rangle = \langle u_z|\,\hat{d}_z\,|u_s\rangle$ and in the WZ region $\langle u_x|\,\hat{d}_x\,|u_s\rangle = \langle u_y|\,\hat{d}_y\,|u_s\rangle \neq \langle u_z|\,\hat{d}_z\,|u_s\rangle$. Since the electron and hole states spread over the ZB and the WZ region we write

$$\begin{aligned}M_i\langle f_h|f_e\rangle = M_i^{ZB}\langle f_h|f_e\rangle^{ZB} + M_i^{WZ}\langle f_h|f_e\rangle^{WZ} \\ (i = x, y, z).\end{aligned} \tag{4.18}$$

By considering (4.18) and assuming that the light propagates along the z axis, i.e. along the nanowire with a polarization vector normal to the nanowire axis such that $e_z = 0$, Eq. (4.17) is written as

$$\begin{aligned}\left(\alpha\langle 0| + \beta\langle 1|\right)\mathbf{e}\cdot\hat{\mathbf{d}}\left|X^-\right\rangle \\ = M^{ZB}\left\{C_1 e_x\langle f_h^1|f_{e2}\rangle + C_3 e_y\langle f_h^3|f_{e2}\rangle\right\}^{ZB} \\ +M^{WZ}\left\{C_1 e_x\langle f_h^1|f_{e2}\rangle + C_3 e_y\langle f_h^3|f_{e2}\rangle\right\}^{WZ}.\end{aligned} \tag{4.19}$$

Furthermore, the matrix element of the momentum operator between $|2\rangle$ and $|X^-\rangle$ is calculated as

$$\begin{aligned}
\langle 2|\,\mathbf{e}\cdot\hat{\mathbf{d}}\,|X^-\rangle &= \langle\psi_{vm}|\,\mathbf{e}\cdot\hat{\mathbf{d}}\,|\alpha\uparrow+\beta\downarrow,u_s,f_{e1}\rangle \\
&= \alpha\big\{C_1e_xM_x\langle f_h^1|f_{e1}\rangle + C_3e_yM_y\langle f_h^3|f_{e1}\rangle\big\} \\
&\quad +\beta\big\{C_2e_xM_x\langle f_h^2|f_{e1}\rangle + C_4e_yM_y\langle f_h^4|f_{e1}\rangle\big\} \\
&= M^{ZB}\big\{\alpha\big(C_1e_x\langle f_h^1|f_{e1}\rangle + C_3e_y\langle f_h^3|f_{e1}\rangle\big)+ \\
&\qquad \beta\big(C_2e_x\langle f_h^2|f_{e1}\rangle + C_4e_y\langle f_h^4|f_{e1}\rangle\big)\big\}^{ZB} \\
&\quad +M^{WZ}\big\{\alpha\big(C_1e_x\langle f_h^1|f_{e1}\rangle + C_3e_y\langle f_h^3|f_{e1}\rangle\big)+ \\
&\qquad \beta\big(C_2e_x\langle f_h^2|f_{e1}\rangle + C_4e_y\langle f_h^4|f_{e1}\rangle\big)\big\}^{WZ}.
\end{aligned} \tag{4.20}$$

Eqs. (4.19) and (4.20) show that the charged-exciton with a mixed-hole part couples simultaneously to both the input spin qubits in QD_1 as well as to the electron state in QD_2. In the following, we consider some pure states and show that they cannot provide the simultaneous coupling between ground states $|0\rangle$, $|1\rangle$, and $|2\rangle$ and the charged exciton state $|X^-\rangle$:

- By considering a charged-exciton with a spin-up heavy-hole for which $C_2 = C_4 = 0$ then (4.20) will be:

$$\begin{aligned}
&\langle 2|\,\mathbf{e}\cdot\hat{\mathbf{d}}\,|X^-\rangle \\
&\qquad = \alpha M^{ZB}\big\{C_1e_x\langle f_h^2|f_{e1}\rangle + C_3e_y\langle f_h^4|f_{e1}\rangle\big\}^{ZB} \\
&\qquad + \alpha M^{WZ}\big\{C_1e_x\langle f_h^2|f_{e1}\rangle + C_3e_y\langle f_h^4|f_{e1}\rangle\big\}^{WZ}
\end{aligned} \tag{4.21}$$

  for $\alpha = 0$ then $\langle 2|\,\mathbf{e}\cdot\hat{\mathbf{d}}\,|X^-\rangle = 0$.

- By considering a charged-exciton with a spin-down heavy-hole for which $C_1 = C_3 = 0$, then (4.19) will be:

$$\big(\alpha\,\langle 0| + \beta\,\langle 1|\,\big)\mathbf{e}\cdot\hat{\mathbf{d}}\,\big|X^-\big\rangle = 0 \tag{4.22}$$

We summarized these cases in the Fig. 4.8. As we see, for a charged-exciton with pure spin hole state in Fig. 4.8 (a) and (b), the simultaneous coupling to all three ground-states is not provided. Eq. (4.20) shows that the dipole moment of the transition $|2\rangle$ to $|X^-\rangle$ depends on the input coefficients α and β. This might be seen as a problem at the first glance, but fortunately as

long as the adiabatic condition Eq. (2.34) is satisfied, this uncertainty does not affect the STIRAP efficiency.

For the numerical calculation, we do not perform a detailed bandstructure calculation, we simply assume the envelope functions f_h^i with $i = 1...6$ are the same in the valence subbands with equal expansion coefficients C_i. For example, in calculating d_P and d_S shown in Fig. 4.3, we have assumed equal C_i coefficients and equal f_i envelops. Since the calculation for this figure are for a three-level STIRAP scheme, we put $\alpha = 1,\ \beta = 0$ such that $d_P = \langle 0|\, \mathbf{e}\cdot\hat{\mathbf{d}}\, |X^-\rangle$ and $d_S = \langle 2|\, \mathbf{e}\cdot\hat{\mathbf{d}}\, |X^-\rangle$. We also assumed a circular polarization light with $e_x = e_y = 1/\sqrt{2}$ and also $M = M^{ZB} = M^{WZ}$. We point to that the general conclusions are the same for other combinations of C_i values. Evaluation of the precise values of these quantities requires a more detailed bandstructure calculation, e.g. in the framework of a multiband **k.p** model or using atomistic methods [24, 108, 63].

In fact, our assumption that C_i coefficients and f_i envelops to be equal, is not actually a significant limitation, since the dipole moments for unqual quantities of C_i and f_i (subject to the requirements $\sum_i |C_i|^2 = 1$ and $\langle\psi_v|\psi_v\rangle = 1$) can always be maximized by rotating the polarization of the laser light according to (4.19) and (4.20) by adjusting e_x and e_y. Thus, we don't expect the dipole moments to be drastically affected by this choice.

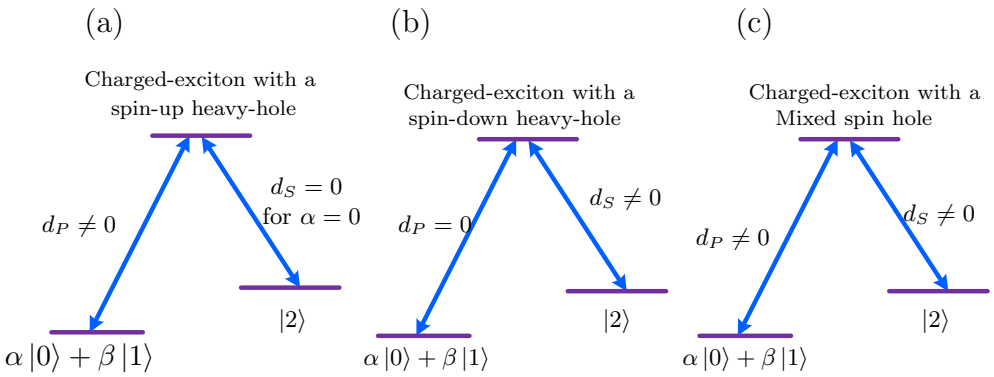

Figure 4.8: Coupling of the charged-exciton to the ground-states in the STIRAP scheme with a (a) pure state spin-up heavy-hole part; (b) pure state spin-down heavy-hole part and (c) mixed-spin hole part.

4.3 Two-qubit gate

To demonstrate two-qubit operations, we will implement a CNOT gate based on two-DQD in a nanowire as shown in Fig. 4.9, where the control and target qubits are encoded on DQD_c and DQD_t, respectively. In each DQD, the height of the QDs and their separation should be chosen as a trade-off between a good confinement of the electron states and a good overlap with the charged-exciton state featuring a hole inside the barrier. By making the height of the QDs smaller, the confinement of the single-particle electron states decreases and they diffuse more inside the barrier. This results in a bigger overlap with the hole inside the barrier which in turn increases the transition dipole moment. On the other hand, as the height of the QDs decreases below 2 nm [cf. Fig 3.7], the electron states will have a significant overlap with each other and the tunneling probability of the electron states which is not desirable will increase. The same argument also applies to the distance between the QDs. The diameter of the QD should also be chosen as a trade-off between a large dipole moment and sufficient energy level difference between the ground-state charged-exciton and the first higher order charged-exciton [109].

In the following, we consider a specific two-DQD with geometrical parameters mentioned in the caption of Fig. 4.9. Fig. 4.10 shows the single-particle electron ground-states and the lowest-energy bound-state hole in DQD_c and DQD_t. The barrier between the QDs of DQD_c is smaller in comparison to that of DQD_t, while the QDs heights in DQD_c are bigger than that of DQD_t. In fact, we cannot reduce both the barrier width and the heights of the QDs at the same time, because it makes the electron wavefunctions to overlap significantly.

The initial configuration consists of an electron in QD_1 in each DQD of the full system as illustrated in Fig. 4.11 (a). The details of the initialization of this configuration using a sequence of STIRAP processes are presented in Sec. 4.4.2. The conditional two-qubit CNOT operation then takes place as follows:

Step 1: The first STIRAP process acts on the control qubit in DQD_c and maps the initial spin qubit $\alpha\,|0\rangle + \beta\,|1\rangle$ to the position degree of freedom $\alpha\,|0\rangle + \beta\,|2\rangle$ as depicted in Fig. 4.11 (b). This is accomplished by choosing the

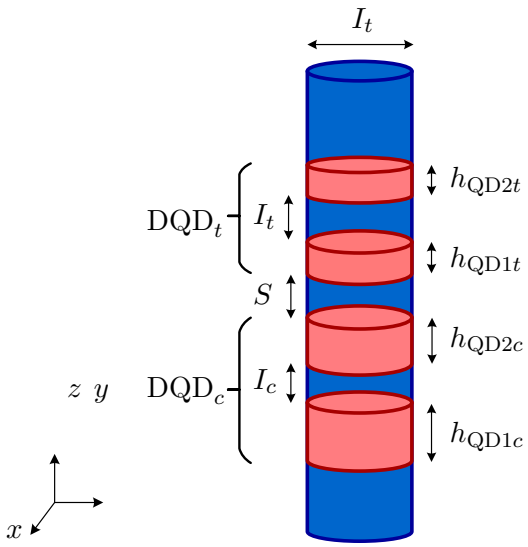

Figure 4.9: Two DQDs in a nanowire. The geometrical parameters of DQD_c are $h_{QD1c} = 11$ nm, $h_{QD2c} = 10$ nm, $I_c = 8$ nm, and the parameters of DQD_t are $h_{QD1t} = 5$ nm, $h_{QD2t} = 3$ nm, $I_t = 10$ nm. The nanowire diameter is $d_{NW} = 40$ nm.

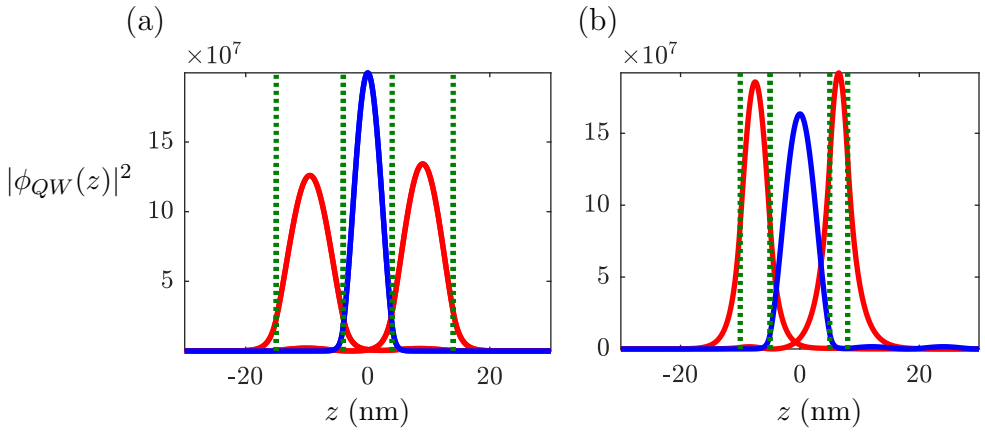

Figure 4.10: Normalized single-particle electrons (red) and hole (blue) probability densities $|\phi_{QW}(z)|^2$ in the (a) DQD_c and (b) DQD_t of the two-DQD system of Fig. 4.9. The single-particle energies of DQD_c are: $E_{e1} = 31.7$ meV, $E_{e2} = 35.1$ meV, $E_h = 6.8$ meV and DQD_t are $E_{e1} = 68.2$ meV, $E_{e2} = 96.6$ meV, $E_h = 5$ meV.

STIRAP parameters $\chi = -\pi/2$ and $\eta = 0$ as it was discussed in the previous section.

The transfer of an electron from the $|1\rangle$ to the $|2\rangle$ state leads to a new

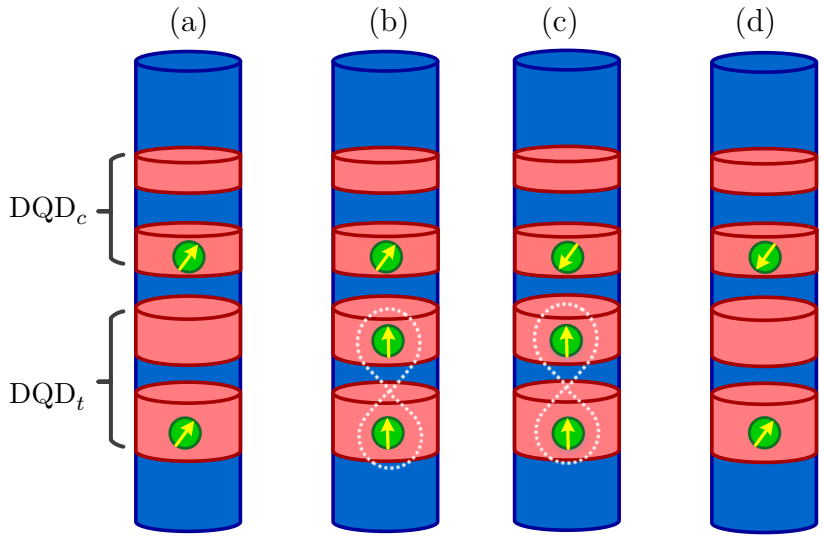

Figure 4.11: Illustration of the CNOT gate operation for a nanowire containing two DQDs. (a) The initial state of the structure which includes the control qubit in DQD$_c$ and target qubit in DQD$_t$. (b) The first STIRAP process maps the spin state of the control qubit in DQD$_c$ to the position state. (c) The second and third STIRAP processes act on the target qubit and flip its spin depending on the control qubit state. (d) The fourth STIRAP process returns the control qubit to its initial spin state.

charge distribution of DQD$_c$ which via the Coulomb interaction exerts a potential change on the target qubit in DQD$_t$ leading to modified DQD$_t$ transition frequencies. The laser fields detunings Δ_0, Δ_1, and Δ_2 of the STIRAP in DQD$_t$ is written as:

$$\begin{aligned} \Delta_0 &= E_{X^-} - E_{e_0} - \omega_0 \\ \Delta_1 &= E_{X^-} - E_{e_1} - \omega_1 \\ \Delta_2 &= E_{X^-} - E_{e_2} - \omega_2 \end{aligned} \tag{4.23}$$

where E_{X^-} is the charged-exciton energy; E_{e_0} and E_{e_1} are the single-particle energies of the spin-up and down electron in QD$_1$; E_{e_2} is the single-particle energy of the spin-up electron in QD$_2$; ω_0, ω_1 and ω_2 are respectively the laser fields 0, 1 and 2 frequencies. After the first STIRAP which affects the charge distribution of the DQD$_c$, the laser field detunings of the STIRAP in DQD$_t$

are changed to:

$$\begin{aligned}\Delta'_0 &= E'_{X^-} - E'_0 - \omega_0 \\ \Delta'_1 &= E'_{X^-} - E'_1 - \omega_1 \\ \Delta'_2 &= E'_{X^-} - E'_2 - \omega_2\end{aligned} \tag{4.24}$$

Now, from (4.24), we calculate the new two-photon detunings of the STIRAP in DQD_t as:

$$\delta'_2 = \Delta'_2 - \Delta'_0 = -E'_2 + E'_0 - \omega_2 + \omega_0 \tag{4.25}$$

From (4.23), we write

$$\delta_2 = \Delta_2 - \Delta_0 = -E_2 + E_0 - \omega_2 + \omega_0 \tag{4.26}$$

Then, by substracting (4.26) from (4.25):

$$\delta'_2 - \delta_2 = \Delta E_0 - \Delta E_2 \tag{4.27}$$

Here, $\Delta E_0 = E'_0 - E_0$ and $\Delta E_2 = E'_2 - E_2$ are respectively the target qubit e_1 and e_2 energy changes due to the relocation of the electron in DQD_c (control qubit) form QD_{1c} to QD_{2c}. In a same way we obtain the following expression for $\delta'_1 - \delta_1$:

$$\delta'_1 - \delta_1 = \Delta E_0 - \Delta E_1 \tag{4.28}$$

We calculate E_0, E_1, E_2, E'_0, E'_1, and E'_2 using the configuration interaction method discussed in Chapter 3. Our system is a two-DQD shown in Fig. 4.9 with two electrons in each DQD. We calculate the single-particle electron states by solving the non-interacting Schrödinger equation (2.2). Then, expanding the Hamiltonian on the basis of the single-particle electron states, the eigenvalues of the Hamiltonian specify the energies E_0, E_1, E_2, E'_0, E'_1, and E'_2.

Fig. 4.12 shows δ'_2 for DQD_t as function of the separation distance S between the two DQDs. Without loss of generality, we chose $\delta_2 = 0$ since it can be adjusted by laser lights to the corresponding transitions in DQD_t. We consider a separation S between the DQDs of at least 8 nm in order to prevent single-particle tunneling and at the same time to allow for significant Coulomb

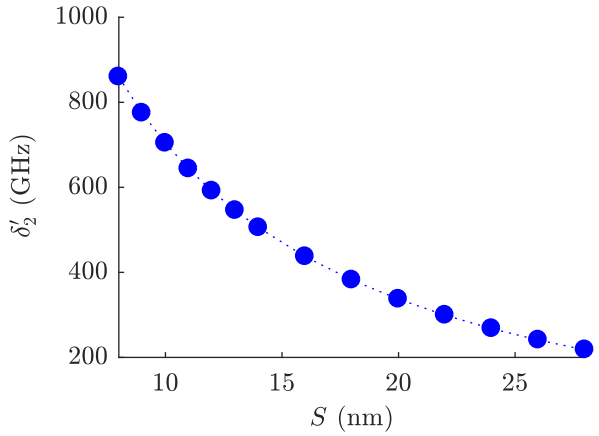

Figure 4.12: Shift in two-photon detuning, δ_2', in DQD_t as a function of the separation, S, between DQD_c and DQD_t after step 1 for a control qubit initially in the state $|1\rangle_c$.

coupling. Even for fairly large separations $S > 8$ nm between the two DQDs, we observe that the strong Coulomb interaction leads to the detuning δ_2' of several hundreds of GHz. The two-photon detuning δ_1' of the STIRAP in DQD_t will change less than 1 GHz for a magnetic field B of a few Tesla [110] which is much smaller in comparison to the changes of the δ_2'.

Step 2: A second and third STIRAP process act on the target qubit in DQD_t performing a single-qubit NOT gate with $\chi = -\pi/4$, $\eta = 0$ and $\zeta = \pi$ as shown in Fig. 4.11 (c) discussed in the previous section. The effect of this single-qubit rotation is strongly dependent on the charge state of the control qubit due to the influence of the Coulomb interaction, which affect δ_2'.

Step 3: The final STIRAP process with $\chi = -\pi/2$, $\eta = 0$ and $\zeta = 0$ acts on the control qubit in DQD_c by mapping back the position degree of freedom to the spin qubit as shown in Fig. 4.11 (d) thus returning DQD_c to its initial state.

The final result of the STIRAP processes is the rotation of the target qubit alone conditional on the state of the control qubit as required for the two-qubit CNOT operation.

4.4 Fidelity

The unitary evolution within the four-level single-DQD Hilbert space generated by the Hamiltonian, $H(t)$, in Eq. (4.13), over an entire operation, can formally be written as the map $U = \mathcal{T}\exp\left[-i\int_{-\infty}^{\infty} \mathrm{d}t'\, H(t')\right]$, where $\mathcal{T}$ is the time-ordering operator. In practice, we construct the map through numerical solutions of the time-dependent Schrödinger equations described in Sec. 2.4.1 in Eq. (2.22). More specifically, given a set of physical parameters, $\mathcal{P}$, we can calculate the evolution of the two linearly independent initial states $|0\rangle$ and $|1\rangle$,

$$U(\mathcal{P})\,|0\rangle = \sum_i u_{i0}(\mathcal{P})\,|i\rangle\,, \tag{4.29}$$

$$U(\mathcal{P})\,|1\rangle = \sum_i u_{i1}(\mathcal{P})\,|i\rangle\,, \tag{4.30}$$

where the argument $\mathcal{P}$ signifies that the map is a function of the parameters. These two evolved states can be used for constructing a 2×2 matrix representation, $\mathbb{U}(\mathcal{P})$, of $U(\mathcal{P})$ within the qubit subspace, $\mathcal{H}_q = \mathrm{span}(|0\rangle, |1\rangle)$, of the DQD, such that $\mathbb{U}_{ij}(\mathcal{P}) := u_{ij}(\mathcal{P})$, with $i,j \in \{0,1\}$. For single qubit operation, we consider a reference qubit-gate operator, G, with 2×2 matrix representation $\mathbb{G}$, which is normalized such that $\mathrm{Tr}\left[\mathbb{G}^2\right] = 1$. The fidelity of the operation with respect to the reference gate is then calculated as

$$\mathcal{F}[U(\mathcal{P}), G] = |\mathrm{Tr}[\mathbb{U}(\mathcal{P})\mathbb{G}]|^2. \tag{4.31}$$

As an example, we can calculate the fidelity of the evolution with respect to the NOT-gate, X, which is represented by the normalized gate matrix

$$\mathbb{X} = \frac{1}{\sqrt{2}}\begin{bmatrix} 0 & 1 \\ 1 & 0 \end{bmatrix}. \tag{4.32}$$

This fidelity is plotted as a function of the detunings δ_1 and δ_2 in Fig. 4.13. To evaluate the two-qubit gate fidelity, we take a mean-field approach, where the influence of the control DQD is a change of the effective parameters seen by the target DQD. In particular, the target DQD will see a set of parameters $\mathcal{P}_i$ when the control qubit is in state $|i\rangle_c$, where we take the only change in parameters to be the two-photon detuning, δ_2, induced by the shift in

the effective Coulomb potential seen by DQD_t [see Fig. 4.12]. We write the effective two-qubit evolution operator, $U^{(2)}$, in the control-target qubit Hilbert space, $\mathcal{H}_c \otimes \mathcal{H}_t$, as

$$U^{(2)}(\mathcal{P}_0, \mathcal{P}_1) = \frac{1}{\sqrt{2}}(|0\rangle\langle 0| \otimes U(\mathcal{P}_0) + |1\rangle\langle 1| \otimes U(\mathcal{P}_1)), \tag{4.33}$$

To calculate the performance of the system as a CNOT gate, we use the reference gate, J,

$$J = \frac{1}{2}(|0\rangle\langle 0| \otimes X + |1\rangle\langle 1| \otimes I), \tag{4.34}$$

where I is the normalized identity operator with matrix representation

$$\mathbb{I} = \frac{1}{\sqrt{2}}\begin{bmatrix} 1 & 0 \\ 0 & 1 \end{bmatrix}. \tag{4.35}$$

The fidelity of $U^{(2)}$ with respect to J is then

$$\begin{aligned} \mathcal{F}[U^{(2)}(\mathcal{P}_0, \mathcal{P}_1), J] &= \left|\mathrm{Tr}\left[U^{(2)}(\mathcal{P}_0, \mathcal{P}_1)J\right]\right|^2 \\ &= \frac{1}{4}|\mathrm{Tr}[\mathbb{U}(\mathcal{P}_0)\mathbb{X}] + \mathrm{Tr}[\mathbb{U}(\mathcal{P}_1)\mathbb{I}]|^2 \end{aligned} \tag{4.36}$$

This two-qubit gate fidelity is plotted in Fig. 4.14, showing that high fidelities can be reached either by inducing a sufficiently large Coulomb shift above $\sim 400\,\mathrm{GHz}$, corresponding to a DQD separation of less than $\sim 16\,\mathrm{nm}$, or by hitting one of the interference fringes appearing around $\delta_2 = 100\,\mathrm{GHz}$.

4.4.1 Effects of decoherence

A quantum system is always surrounded by an environment that is a source of decoherence. Here we review the detrimental effects of various types of decoherence on STIRAP. STIRAP is robust against some causes of decoherence, e.g., irreversible population loss from the middle state and spontaneous emission within the system. It is more sensitive to others, such as decoherence.

Of primary concern is the slow fluctuations of the charge environment and the nuclear spins of the host material. Such noise sources influence the system by driving fluctuations of the various energy levels. The time scale of the fluctuations is typically longer than microseconds and the magnitude is on the order of a few GHz [111, 112]. In order for the gate operations to be

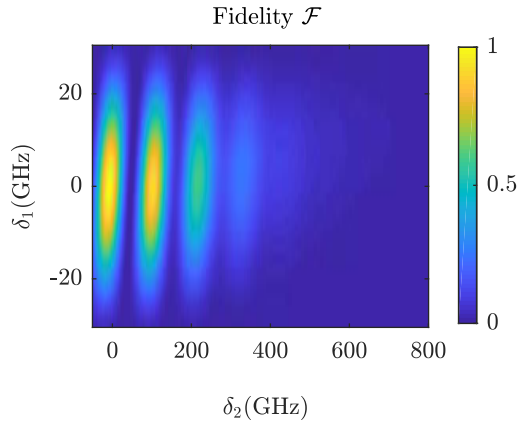

Figure 4.13: The fidelity of the single-qubit NOT gate as a function of two-photon detunings δ_1 and δ_2. The STIRAP parameters in this calculation are: $\chi = -\pi/2$, $\eta = 0$, $\tau = 9$ ps, $\Delta T = 5$ ps, $\Delta = 20$ GHz, and the peak amplitude of Ω_0, Ω_1 and Ω_2 are considered 282, 282 and 400 GHz, respectively.

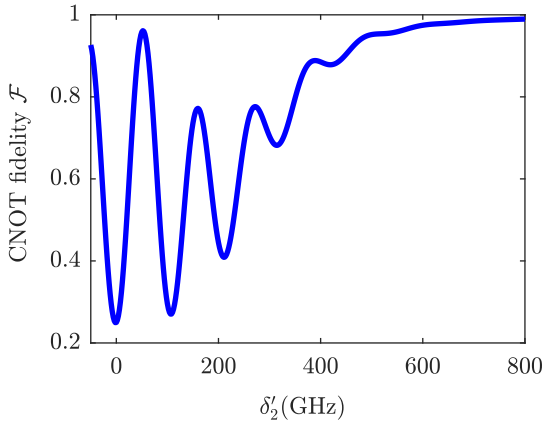

Figure 4.14: The fidelity of the two-qubit CNOT gate as a function of the shift in two-photon detuning δ_2'. Calculation parameters are the same as Fig. 4.13, with $\delta_1 = \delta_2 = 0$.

robust against these noise sources, we must ensure that the bandwidth of the STIRAP processes is larger than the magnitude of the fluctuations, ensuring a high gate fidelity [113]. Furthermore, the time scale of the STIRAP processes should be shorter than the T_2^* decoherence times to allow for the application of dynamical decoupling schemes to protect the coherence of the qubit [112]. The bandwidth of the two-photon resonances used in the STIRAP-induced gates

depends on the power and duration of the applied laser fields, the overlap time between the two optical pulses, the transition dipole moments and the ground state Zeeman splitting. We choose these parameters within a realistic range such that the NOT gate fidelity is more than 0.94 when two-photon detunings δ_1 and δ_2 are varied over ranges of 10 and 5 GHz, respectively, as is shown in Fig. 4.13, thus ensuring robustness against variations in the detunings posed by the environment. With these parameters, the STIRAP rotations can be implemented on a time scale of tens of picoseconds, which is much longer than the typical electron T_2^* coherence time of a few nanoseconds [114, 115, 116].

The time required to execute a gate by a conventional STIRAP process considered in this work is inversely proportional to the Rabi frequencies. Thus, for faster operations we need to increase the input power. However, several strategies have been proposed to speed up the adiabatic passage, and these can straightforwardly be combined with the proposed scheme to achieve higher gate fidelities in a shorter time scale without increasing the laser lights intensity [117, 118, 119]. Reducing the gate operation time also results in a wider bandwidth over δ_1 and δ_2 in comparison to what we achieved in the Figs. 4.13 and 4.14 by a conventional STIRAP.

In this work, we used the electron spin states in ZB QDs in a WZ nanowire for the qubit realization as shown in Fig. 4.15 (a). However, by controlling the crystallographic phase of the InP nanowire during the fabrication process it is also possible to fabricate WZ QDs in a ZB nanowire [120]. In this case the spin of the hole confined in the WZ QDs is used as the spin qubit, and a charged exciton state composed of two holes and one electron acts as the intermediate state as shown in Fig. 4.15 (b) . Because of the p-like symmetry of the hole state at the atomic scale, the hyperfine interaction with the nuclear spins is suppressed, and the hole spin has a longer coherence time in comparison to the electron spin [121]. While the long coherence time of this scheme is attractive, the electron is not a mixed spin state, and thus the charged exciton state cannot couple efficiently to all of the three lowest energy hole states of the DQD [cf. Sec 4.2.2] as required for single-qubit operations.

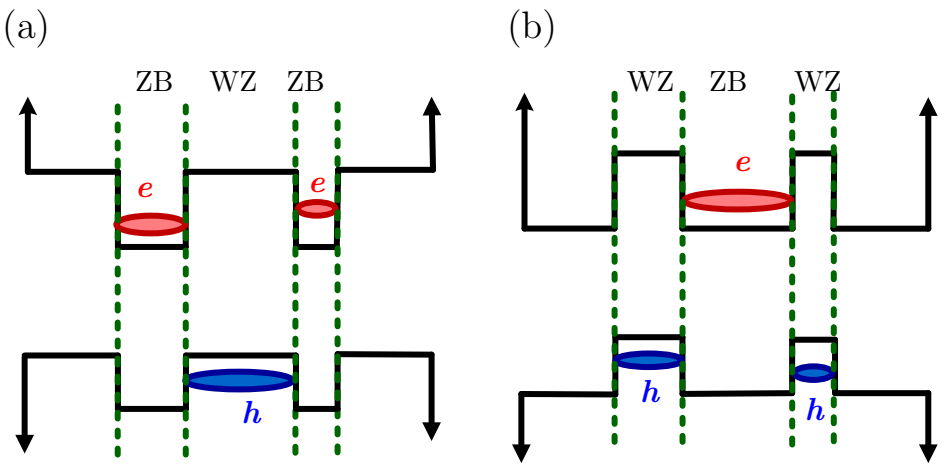

Figure 4.15: (a) ZB QDs inside a WZ nanowire (b) WZ QDs inside a ZB nanowire.

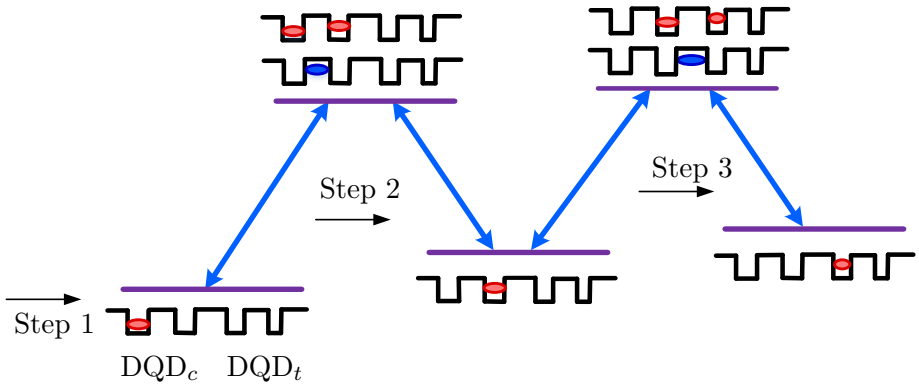

Figure 4.16: Scheme for initializing the electrons in a two-DQD. The electron is transferred from QD$_1$ of DQD$_c$ to QD$_1$ of DQD$_t$ using two STIRAP processes.

4.4.2 Initializing electrons in DQDs in a nanowire

The two-electron configuration illustrated in the Fig. 4.11 (a) can be initialized using the procedure schematically illustrated in Fig. 4.16.

Step 1: By applying an external electric field in the z direction, an electron from the nearby reservoir is transferred to QD$_1$ of DQD$_c$. Further charging is suppressed because of the Coulomb blockade.

Step 2: This electron is moved to QD$_2$ of DQD$_c$ using one STIRAP operation as shown in Fig. 4.16.

Step 3: The electron is transferred to the QD_1 of DQD_t using another STIRAP operation as shown in Fig. 4.16.

Now that QD_1 of DQD_c is empty, another electron from the reservoir is transferred to it.

The spin of these electrons are initialized by applying a magnetic field.

4.5 Summary

We have proposed a novel scheme for all-optical quantum gating based on qubits encoded in ultraclean crystal-phase type-II double QDs (DQDs) in a nanowire, which are manipulated using stimulated Raman adiabatic passage (STIRAP). The key feature of the scheme is the exploitation of a charged exciton state with a mixed hole which couples with three lowest electron states of the double-quantum-dot in the type II configuration without involving additional external fields. This coupling is essential for high-fidelity qubit rotations by means of the STIRAP process. The high-fidelity two-qubit CNOT operation is performed using Coulomb coupling to cause a shift of the target DQD transition frequencies leading to a conditional violation of the STIRAP two-photon resonance condition in the target DQD. The two DQD structure and also STIRAP parameters are designed such that the CNOT gate is robust against the charge and spin noises. This robustness is largely attributed to the flexibility of the scheme with respect to bandwidths and dynamical time scales ensured by using STIRAP for rapid control operations.

CHAPTER 5

Conclusion and outlook

5.1 Summary

The main goal of this work was to understand the physics of the novel type-II QDs. This understanding guides us to design universal, scalable, and addressable quantum gates for quantum information.

To model the exciton properties of the QDs in a nanowire, a numerical tool based on the configuration-interaction method, to solve the Schrödinger equation governing the system, has been implemented. The exciton Hamiltonian in this method is expanded on the single-particle electron and hole states. We studied the convergence of this numerical method. Since the single-particle hole in the type-II QD is not confined inside the QD, and it's spread all over the nanowire, then there are many single-particle hole states close in the energy in this structure which contribute to the exciton states and need to be included in the calculation. For this reason the computation of the exciton states is more demanding in type-II QDs in comparison to that in the type-I QDs. For example in GaAs/AlGaAs type-I QDs both the electron and the hole are confined inside the QD and there are very few bound single-particle states which are contributing to the exciton state. As the structure size increases, the energy spacing of the single-particle states decreases. Consequently, a larger number of single-particle states needs to be included in the expansion of the exciton Hamiltonian. We used the configuration-interaction method to

calculate the exciton states in both small and large geometries. For instance, structures ranging from 10 to 60 nm in diameter and 40 to 100 nm in length. For calculation of the exciton states in large structures we needed to use 10 paralleled cluster computers working for 30 hours. We observed that, while the method converges very fast when calculating the exciton energy, more computational effort is needed to achieve convergence of the oscillator strength. In fact, in order to calculate the exciton oscillator strength with a 95% accuracy, more single-particle states need to be considered, compared to the amount needed to calculate the exciton energy with the same accuracy. To calculate the charged-exciton state and multi-exciton state which are consist of more than two particles, the computational effort is remarkably larger in type-II QDs in comparison to the exciton state in these structures. Consequently, we have discarded the use of the configuration-interaction method for calculating these states in type-II QDs.

We observed that, in the both type-I and type-II QDs, the emission intensity quantified by the oscillator strength increases when the diameter of the structure becomes larger. We calculated the oscillator strength in structures with diameters up to 60 nm. While a large diameter initially appears attractive, on the other hand, by increasing the QD diameter, the energy separation between the ground-state and first-excited exciton state decreases. This makes more challenging to experimentally address the ground-state exciton. Furthermore, for sufficiently large diameters, where the exciton size is no longer small compared to the optical wavelength, the dipole approximation breaks down leading to a stabilization of the oscillator strength for increasing diameter.

For a nanowire with a short length, the exciton size is affected by the nanowire boundaries. While it increases linearly with the nanowire length up to 60 nm, after that the size assumes a constant value independent of the nanowire length such that the exciton properties become independent of the nanowire length.

We showed a large exciton oscillator strength can clearly be obtained using a large diameter d_{QD} or a small QD height h_{QD}. We also observed that, in both cases, a spatially large exciton is obtained with small energy separation to the first higher-order state. We thus concluded that the single-quantum-

dot geometry is not ideal for quantum gating applications. We showed that, by engineering a double-quantum-dot nanowire structure, it is possible to improve the exciton oscillator strength while maintaining a spatially well-confined profile. The type-II single-quantum-dot has much smaller oscillator strength in comparison to that in type-I single-quantum-dot. However, oscillator strengths close to those of a type-I QD can be achieved in type-II structures by using a double-quantum-dot, instead of a single-quantum-dot.

Including the Coulomb interaction is very important in calculating the exciton properties in the type-II single-quantum-dots such that in some geometries, the ground-state exciton oscillator strength becomes at least 20 times bigger by including Coulomb interaction and obviously it cannot be neglected. On the other hand, the Coulomb interaction is not the dominant effect for the exciton properties of the bound-exciton states in the double-quantum-dot structures because the hole is confined by the band structure potential profile.

We used the electron spin in a type-II double-quantum-dots as a qubit for the quantum computation. For optical manipulation of the qubits we used the STIRAP technique which is robust against the laser lights parameters [81, 122, 123]. Combination of the electron spin and position degrees of freedom can provide a four-level scheme in a double-quantum-dot, necessary for single-qubit rotation in STIRAP gating. A charged-exciton state is used to couple three-ground electron states. The novelty showed here is that this coupling is significantly more efficient in the type-II QDs in comparison to what is calculated in the type-I QDs.

For calculating the charged-exciton featuring a hole confined between two QDs, we did not include the Coulomb interaction because its negligable compared to the band edge confinement effect. Unlike most papers in the field (e.g., [124] and [125]) presenting phenomenological models with hand-picked parameters, we considered a specific type-II system, the crystal-phase InP nanowire, with specific realistic geometrical parameters, and we compared its performance with a realistic type-I GaAs/AlGaAs system.

We also showed that a charged-exciton with a pure spin hole part cannot provide simultaneous coupling to all three ground states in the STIRAP scheme. Conversely, a mixed hole configuration allows for efficient coupling of the full two-dimensional spin-qubit space localized in one of the QDs of the

DQD structure to an electron state in the other QD as required for single-qubit gate operations. To show this coupling we developed a multi-band formalism compatible with sophisticated methods for calculating the semiconductor bandstructure, such as **k.p** theory, tight-binding, or DFT (density functional theory). However, for design and optimization purposes, in order to achieve a lower computational cost, we have thus chosen to perform the calculations of the dipole moments using a single-band model. We stress that our objective is not to calculate exact dipole moments but simply show that the performance of the type-II system is superior to that of the type-I system. While we acknowledge that more advanced calculation methods may produce different values of the dipole moments, we believe that our conclusion, that the type-II system performs significantly better than the type-I system, will not be altered by repeating the calculations using such advanced method.

We deigned a CNOT gate in a two-double-quantum-dot in a nanowire. We used two electrons in the system, one in each double-quantum-dot, to encode the target and control spin qubit. The position of the control qubit in the double-quantum-dot determines the conditional operation on the target qubit. We showed that the Coulomb interaction, which is in an order of a few hundreds of GHz, is strong enough to induce a shift in the STIRAP frequencies of the target qubit in the neighboring double-quantum-dots. We showed that the operation is robust against the spin and charge noises.

5.2 Future work

In this section, we list several possible extensions and outlooks of this work, and we believe this list can be extended.

- We studied the exciton properties of the type-II QDs in this work. However, for extracting the optical properties of these quantum dots, the charged-exciton state and multi-exciton states are also needed to be calculated. This has not been done, yet, to the best of our knowledge. Due to the computational complexity of the configuration-interaction method, we did not use it for calculating charged-exciton and multi-exciton states. Therefore, developing a fast and efficient numerical tool

to calculate many-particle states in type-II quantum-dots is seen as the next step for developing a complete tool to study these structures.

- We calculated the exciton states by including the Coulomb interaction. We did not consider other details of the electronic band structure such as the strain and polarization fields. There are already some works which have studied single-particle states by including these effects in crystal-phase type-II QDs[62, 63]. However, those works do not consider the Coulomb interaction. Developing a comprehensive numerical tool to calculate exciton states with involving all of the aforementioned effects (Coulomb interaction, strain, polarization fields) will help to model the structure more accurately.

- From the experimental point of view, only a few crystal-phase type-II QDs in a nanowire are fabricated, mainly for demonstrating the ground-state exciton emission intensity. However, many of the interesting phenomena introduced in this thesis have not been observed experimentally, yet. Therefore, fabrication and measurement of the proposed devices are essential for validating the theory provided here, such as the large oscillator strength of the double-quantum-dot configuration and single- and two-qubit gates based on these structures by using stimulated Raman adiabatic passage.

- We are using the spin of the electron for storing information and the position of the electron for quantum gating. Spin qubit is widely used for storing the information due to its long coherence time in comparison to the charge qubit which always has been subjected to the electric field fluctuations from impurities and defects in the semiconductor environment leading to very short coherence times. Nevertheless, in recently fabricated ultra-clean quantum dots, it has been shown that the charge noise has been significantly reduced, reaching levels close to dephasing-free qubit operations [111]. For this reason, designing a STIRAP scheme in which the position or charge degree of freedom is used to encode the qubit instead of the spin degree of freedom simplifies the experimental setup since there is no need to use a magnetic field to apply to the

structure for defining the initial spin state of the qubits. Since the electron can be moved through a type-II QD-chain by applying sequences of the STIRAP, initializing the qubits could be done optically without using the external electric or magnetic fields. Therefore, designing STIRAP gating scheme based on the position qubits is seen as a possible improvement to the scheme designed in this work.

APPENDIX A

Single-particle solutions

In this Appendix, we solve the Schrödinger equation for the single-particle electron and the hole in a QD in a nanowire. In Sec. 2.2.1, we showed that the wavefunction in this structure can be separated in z direction and in transverse plane as:

$$\Phi(R,\theta,z) = \phi_T(R,\theta)\phi_{QW}(z) \tag{A.1}$$

By replacing (A.1) in the Schrödinger equation $\hat{H}\Psi = E\Psi$:

$$\Big[-\frac{\hbar^2}{2m}\nabla^2 + V_{QW}(z) + V_T(R,\theta)\Big]\phi_T(R,\theta)\phi_{QW}(z) = E\phi_T(R,\theta)\phi_{QW}(z) \tag{A.2}$$

where the confinement potential also is been written as $V = V_T(R,\theta)+V_{QW}(z)$ according to (2.3) and ∇^2 is the Laplacian operator in three dimension which can be written as: $\nabla^2 = \nabla_T^2 + \nabla_z^2$. By dividing the both sides of the above equation by $\phi_T(R,\theta)\phi_{QW}(z)$:

$$-\frac{\hbar^2}{2m}\frac{1}{\phi_T(R,\theta)}\nabla_T^2\phi_T(R,\theta) - \frac{\hbar^2}{2m}\frac{1}{\phi_{QW}(z)}\frac{\partial^2\phi_{QW}(z)}{\partial z^2} + V_{QW}(z) + V_T(R,\theta) = E \tag{A.3}$$

The variables in the transverse and in the z directions are separated as:

$$-\frac{\hbar^2}{2m}\frac{1}{\phi_{QW}(z)}\frac{d^2\phi_{QW}(z)}{dz^2} + V_z(z) = E + \frac{\hbar^2}{2m}\frac{1}{\phi_T(R,\theta)}\nabla_T^2\phi_T(R,\theta) - V_T(R,\theta) \tag{A.4}$$

Then, we have two equations which can be solved independently.

A.1 Solution in the z-direction

The equation (A.4) must be equal to a constant we call it E_z. The reasoning for this will be clear that:

$$-\frac{\hbar^2}{2m}\frac{1}{\phi_{QW}(z)}\frac{d^2\phi_{QW}(z)}{dz^2}+V_{QW}(z)=E_z \tag{A.5}$$

By solving this equation for electrons in the conduction band of a type-I GaAs/AlGaAs SQD in a nanowire we find:

$$\phi_{QW}(z)=\begin{cases} Ae^{kz} & z\leq -h_{QD}/2 \\ Be^{-ilz}+Ce^{ilz} & -h_{QD}/2\leq z\leq h_{QD}/2 \\ De^{-kz} & z\geq h_{QD}/2 \end{cases} \tag{A.6}$$

Where $k=\sqrt{2m_e(\Delta E_c-E_z)}/\hbar$ and $l=\sqrt{2m_eE_z}/\hbar$. Boundary conditions is used for determining A, B, C, and D such that the wavefunction $\phi_{QW}(z)$ and its derivative should be continuous everywhere. By applying this condition at $z=-h_{QD}/2$ and $z=+h_{QD}/2$ we have a homogeneous system of four linear equations with a zero determinant $A=0$ which gives us infinite number of non-trivial solutions. But we have another restriction such that the wavefunction need to be normalized $\int_{-\infty}^{+\infty}|\phi_{QW}(z)|^2dz=1$. By applying this condition we find a finite number of the non-trivial solutions of the problem.

A.2 Solution in the transverse direction

By assuming parabolic potential in the transverse direction as in Eq. (2.5), Eq. (A.4) is written as:

$$-\frac{\hbar^2}{2m}\nabla_T^2\phi_T(R,\theta)+\frac{1}{2}m\omega^2(x^2+y^2)\phi_T(R,\theta)=(E-E_z)\phi_T(R,\theta) \tag{A.7}$$

For solving this equation, we introduce the dimensionless scaling factors:

$$b=\big(\frac{\hbar}{m\omega}\big)^2 \qquad W=\frac{E-E_z}{\hbar\omega} \tag{A.8}$$

and

$$x=bR\cos(\theta) \qquad y=bR\sin(\theta) \tag{A.9}$$

By this definition, then the relation between Cartesian and cylindrical coordinates is:

$$R = \frac{\sqrt{x^2+y^2}}{b} \quad \theta = \cos^{-1}\frac{x}{\sqrt{x^2+y^2}} \; or \quad \theta = \sin^{-1}\frac{y}{\sqrt{x^2+y^2}} \tag{A.10}$$

By some mathematical calculation it can be shown that:

$$\nabla_T^2 = \frac{d^2}{dx^2} + \frac{d^2}{dy^2} = \frac{1}{b^2}\frac{d^2}{dR^2} + \frac{1}{b^2 R}\frac{d}{dR} + \frac{1}{b^2 R^2}\frac{d^2}{d\theta^2} \tag{A.11}$$

By replacing (A.11) in (A.7):

$$\Big(\frac{d^2}{dR^2} + \frac{1}{R}\frac{d}{dR} + \frac{1}{R^2}\frac{d^2}{d\theta^2}\Big)\phi_T(R,\theta) + \Big(2W - R^2\Big)\phi_T(R,\theta) = 0 \tag{A.12}$$

where $W = (E - E_z)/\hbar\omega$. By variable separation method $\phi_T(R,\theta) = \phi_R(R)\phi_\Theta(\theta)$ we obtain:

$$\phi_\Theta(\theta) = e^{im\theta} \tag{A.13}$$

where $m = 0, \pm 1, \pm 2, ...$ is the angular quantum number. And for the radial part we have:

$$\frac{d^2}{dR^2}\phi_R(R) + \frac{1}{R}\frac{d}{dR}\phi_R(R) + \Big(2W - \frac{m^2}{R^2} - R^2\Big) = 0 \tag{A.14}$$

This type of equation is already solved in Schrödinger's article, and the solution is also found in Abramowitz and Stegun [126]. The eigen function is given by:

$$\phi_T^{lm}(R,\theta) = R^{|m|} e^{\left(\frac{-R^2}{2}\right)} \mathcal{L}_l^{|m|}(R^2) e^{im\theta} \tag{A.15}$$

where $\mathcal{L}$ is the Laguerre polynomial. The eigenvalues correspond to these eigenfunctions are also can be found from Eq. (A.14) as $W = 2l + |m| + 1$ or:

$$2l + |m| + 1 = \frac{E - E_z}{\hbar\omega} \tag{A.16}$$

where $l = 0, 1, 2, ...$ is the radial quantum number. Now by substituting $\phi_{QW}(z)$ from Eq. (A.6) and $\phi_T(R,\theta)$ from Eq. (A.15), the three-dimensional wavefunction of the single-particle electron in the conduction band or the single-particle hole in the valence band is written as:

$$\Phi^{nlm}(R,\theta,z) = \phi_{QW}^n(z)\phi_T^{lm}(R,\theta) \tag{A.17}$$

By assuming hard-wall potential in the surface of the nanowire as in the Eq. (2.4), the transverse part of the Eq. (A.4) in the nanowire is:

$$-\frac{\hbar^2}{2m}\frac{1}{\phi_T(R,\theta)}\nabla_T^2\phi_T(R,\theta) = (E - E_z)\phi_T(R,\theta) \tag{A.18}$$

The transverse Laplace operator is given by:

$$\nabla_T^2 = \frac{d}{dR^2} + \frac{1}{R}\frac{d}{dR} + \frac{1}{R^2}\frac{d}{d^2\theta^2} \tag{A.19}$$

Since the potential is assumed to be rotationally symmetric, we can write the wavefunction as $\phi_T(R,\theta) = \phi_R(R)e^{im\theta}$ and thus the separated equation will be:

$$-\frac{\hbar^2}{2m}\Big(\frac{d^2}{dR^2}\phi_R(R)+\frac{1}{R}\frac{d}{dR}\phi_R(R)+\frac{\phi_R(R)}{R^2}\frac{d}{d^2\theta^2}\Big)-(E-E_z)\phi_R(R) = 0 \tag{A.20}$$

which simplifies to:

$$R^2\frac{d^2}{dR^2}\phi_R(R)+R\frac{d}{dR}\phi_R(R)+\Big(\frac{2m}{\hbar^2}(E-E_z)R^2\phi_R(R)-m^2\phi_R(R)\Big) = 0 \tag{A.21}$$

The solution of this equation can be found in [126] and gives the following solution:

$$\phi_R(R) = J_m(\lambda R) + Y_m(\lambda R) + H_m^{(1)}(\lambda R) + H_m^{(2)}(\lambda R) \tag{A.22}$$

Since $Y_n(x)$, $H_n^{(1)}(x)$, and $H_n^{(2)}(x) \to \infty$ when $x \to 0$ we are left with Bessel function $J_n(x)$, so the solution ends up being:

$$\phi_R(R) = J_m(\lambda R) \tag{A.23}$$

where λ is given by:

$$\lambda = \sqrt{\frac{2m}{\hbar^2}(E - E_z)} \tag{A.24}$$

$E_T = E - E_z$ is the single-particle energy in the transverse direction. λ is determined from the boundary condition such that the transverse wave function should be zero at the boundary of the nanowire because of the infinite potential at the surface of the nanowire:

$$\phi_T^{lm}(R = \tfrac{d_{QD}}{2}) = J_m(\lambda\tfrac{d_{QD}}{2}) = 0 \tag{A.25}$$

The Bessel function is equal to zero for arguments which are determined numerically. The lowest energy is at the first Bessel function zero for $J_0(x)$

when $x = 2.4048$, then the ground state energy can be found from solving the Eq. (A.24):

$$2.4048 = \sqrt{\frac{2m}{\hbar^2}(E - E_z)}\frac{d_{QD}}{2} \tag{A.26}$$

The first excited energy can be found from the first zero of the function $J_1(x)$ and so on. Then, the transverse eigenfunctions are written as:

$$\phi_T^{lm}(R, \theta) = J_m(\lambda_l R)e^{im\theta} \tag{A.27}$$

APPENDIX B

Basic differential equations of the STIRAP

STIRAP is an efficient method for transferring populations adiabatically between two discrete quantum states by coupling them using radiation fields via an intermediate state which is usually a radiatively decaying state. Before describing the STIRAP scheme which is a three-level system interaction with two laser lights, we first briefly describe a two-level system interaction with a laser light to review some concepts which we need in illustration of the STIRAP scheme.

B.1 Interaction of a two-state system with a classical field

We want to calculate the time evolution of the two-level system when it interacts with light, so the problem we need to solve is the Schrödinger equation where the Hamiltonian of the combined system-light is given by the sum of the bare Hamiltonian $\hat{H}_0$ and the Hamiltonian due to the interaction with the light field $\hat{H}_{int}$:

$$\hat{H} = \hat{H}_0 + \hat{H}_{int} \tag{B.1}$$

$\hat{H}_0$ in the energy representation can be written as:

$$\hat{H}_0 = E_1 \left|\psi_1\right\rangle \left\langle\psi_1\right| + E_2 \left|\psi_2\right\rangle \left\langle\psi_2\right| \tag{B.2}$$

The eigenvalues E_1 and E_2 are the observable energies of the undisturbed system and $|\psi_1\rangle$ and $|\psi_2\rangle$ are the corresponding eigenvectors. Thus, by construction, the matrix H_0 is diagonal, in the basis of the physical states $|\psi_1\rangle$ and $|\psi_2\rangle$, and the diagonal elements of H_0 are E_1 and E_2. In the dipole approximation, the interaction of a two-level system with the laser light is the projection of the electric dipole moment $\hat{\mathbf{d}}$ onto the light electric field $\mathbf{E}$:

$$\hat{H}_{int}(t) = -\hat{\mathbf{d}}.\mathbf{E}(t) \tag{B.3}$$

For a single laser beam, a traveling-wave with the linear polarization, the electric field at a fixed point is written as $\mathbf{E}(t) = \mathbf{e}\,\mathcal{E}_0(t)\cos(\omega t - \psi)$, where $\mathbf{e}$ is the unit polarization vector, ω is the light frequency and $\mathcal{E}_0$ is the time-varying amplitude of the laser light. By replacing this field in (B.3), the interaction Hamiltonian will be:

$$\hat{H}_{int}(t) = \hat{V}_0\, \mathcal{E}_0(t)\, \cos(\omega t - \psi) \tag{B.4}$$

Where $\hat{V}_0 = -\hat{\mathbf{d}}.\mathbf{e}$. For a two-state system of:

$$\left|\Psi(t)\right\rangle = C_1(t)\left|\psi_1\right\rangle + C_2(t)\left|\psi_2\right\rangle \tag{B.5}$$

The system does not have a dipole moment when it is in an energy eigenstate, so $\langle\psi_1|\hat{V}_0|\psi_1\rangle = \langle\psi_2|\hat{V}_0|\psi_2\rangle = 0$. This means that by defining $V_0 = \langle\psi_1|\hat{V}_0|\psi_2\rangle$, the dipole operator can be written as

$$\hat{V}_0 = -\hat{\mathbf{d}}.\mathbf{e} = V_0 \left|\psi_1\right\rangle \left\langle\psi_2\right| + V_0^* \left|\psi_2\right\rangle \left\langle\psi_1\right| \tag{B.6}$$

By substitution of (B.5) and (B.6) in the Schrödinger equation:

$$\frac{d}{dt}\left|\Psi(t)\right\rangle = -\frac{i}{\hbar}\hat{H}(t)\left|\Psi(t)\right\rangle \tag{B.7}$$

The resulting pair of the coupled ordinary differential equations (ODEs) read, in the vector and matrix form as:

$$\begin{bmatrix}\dot{C}_1(t)\\ \dot{C}_2(t)\end{bmatrix} = -i\begin{bmatrix}\omega_1 & \Omega(t)\cos(\omega t - \psi)\\ \Omega^*(t)\cos(\omega t - \psi) & \omega_2\end{bmatrix}\begin{bmatrix}C_1(t)\\ C_2(t)\end{bmatrix} \tag{B.8}$$

where $\Omega(t) = V_0\mathcal{E}_0(t)/\hbar$ is the so-called Rabi frequency and $\omega_i = E_i/\hbar$ ($i = 1, 2$). To eliminate the relatively uninteresting small variations at the carrier frequency ω induced by the incoming laser light, we introduce a rotating Hilbert-space coordinate,

$$\left|\psi_2'(t)\right\rangle = e^{-i\omega t}\left|\psi_2\right\rangle \tag{B.9}$$

Then the state vector of the system is:

$$\left|\Psi(t)\right\rangle = C_1(t)\left|\psi_1\right\rangle + C_2(t)\left|\psi_2'(t)\right\rangle \tag{B.10}$$

By replacing (B.9), (B.10) and (B.6) in the Schrödinger equation (B.7), the ODEs of Eq. (B.8) will change to:

$$\begin{bmatrix}\dot{C}_1(t)\\ \dot{C}_2(t)\end{bmatrix} = -i\begin{bmatrix}\omega_1 & \Omega(t)e^{-i\omega t}\cos(\omega t-\psi)\\ \Omega^*(t)e^{i\omega t}\cos(\omega t-\psi) & \omega_2-\omega\end{bmatrix}\begin{bmatrix}C_1(t)\\ C_2(t)\end{bmatrix} \tag{B.11}$$

Rotating wave approximation (RWA)

For optical radiation of commonly used laser pulses, the peak value of the Rabi frequency Ω is typically 4 or 5 orders of magnitude smaller than the carrier frequency ω. That is, the photon energy $\hbar\omega$ is much larger than the interaction energy $\hbar\Omega$. Therefore the small carrier-frequency oscillations hold no interest; we are instead concerned with activity that takes place only over many optical cycles. We therefore consider probability amplitudes that are averaged over many optical cycles:

$$\cos(\omega t-\psi)e^{-i\omega t} = \frac{1}{2}\left(e^{-i\psi} + e^{-2i\omega t+i\psi}\right) \to \frac{1}{2}e^{-i\psi} \tag{B.12}$$

By setting $E_1 = 0$ as the ground state of the system without loss of generality, the two-state RWA Schrödinger equation (B.11) will be:

$$\begin{bmatrix}\dot{C}_1(t)\\ \dot{C}_2(t)\end{bmatrix} = -i\begin{bmatrix}0 & \frac{1}{2}\Omega(t)e^{-i\psi}\\ \frac{1}{2}\Omega^*(t)e^{i\psi} & \Delta\end{bmatrix}\begin{bmatrix}C_1(t)\\ C_2(t)\end{bmatrix} \tag{B.13}$$

where

$$\hbar\Delta = \omega_2 - \omega_1 - \hbar\omega \tag{B.14}$$

Then the basic controls appearing here are the time-dependent Rabi frequency $\Omega(t)$ and the detuning Δ. It is through manipulation of these quantities that we control the time evolution of the statevector.

Written more compactly in matrix form, the Schrödinger equation reads

$$\frac{d}{dt}\mathrm{C}(t) = -\frac{i}{\hbar}\mathrm{H}(t)\mathrm{C}(t) \tag{B.15}$$

where $H(t)$ is the RWA Hamiltonian in frequency units,

$$\mathrm{C}(t) = \begin{bmatrix} C_1(t) \\ C_2(t) \end{bmatrix}, \ \mathrm{H}(t) = \hbar \begin{bmatrix} 0 & \frac{1}{2}\Omega(t)e^{-i\psi} \\ \frac{1}{2}\Omega^*(t)e^{i\psi} & \Delta \end{bmatrix} \tag{B.16}$$

B.2 Interaction of a three-state system with a classical field

In three-state Λ system shown in Fig. 2.8 (a) the carrier frequencies of the two fields are each assumed to be close to resonance with one of the transitions, so that each field can be uniquely identified with a particular transition. The pump field P is (near) resonant only with the 1-e transition, while the Stokes field S is (near) resonant only with the e-2 transition. Thus the nonzero interactions, for linearly polarized fields, are:

$$\hat{H}_{intP} = \hat{V_P}\mathcal{E}_P(t)\cos(\omega_P t - \psi_P) \tag{B.17}$$

$$\hat{H}_{intS} = \hat{V_S}\mathcal{E}_S(t)\cos(\omega_S t - \psi_S) \tag{B.18}$$

where $V_P = \langle 1|\,\hat{V}_P\,|e\rangle$ and $V_S = \langle 2|\,\hat{V}_S\,|e\rangle$.

We write the state vector of the three-level system as:

$$|\Psi(t)\rangle = C_1(t)\,|\psi_1'(t)\rangle + C_e(t)\,|\psi_e'(t)\rangle + C_2(t)\,|\psi_2'(t)\rangle \tag{B.19}$$

where, anticipating the removal of the Hamiltonian matrix elements that vary at the carrier frequencies, we choose the rotating coordinates to be:

$$|\psi_1'(t)\rangle = |\psi_1\rangle \tag{B.20}$$

$$|\psi_e'(t)\rangle = e^{-i\omega_P t}\,|\psi_e\rangle \tag{B.21}$$

$$|\psi_2'(t)\rangle = e^{-i(\omega_P-\omega_S)t}\,|\psi_2\rangle \tag{B.22}$$

By replacing the state-vector (B.19) in the Schrödinger equation (B.15), the ODEs governing the three-level system within RWA will be:

$$\begin{bmatrix} \dot{C}_1(t) \\ \dot{C}_e(t) \\ \dot{C}_2(t) \end{bmatrix} = -i \begin{bmatrix} 0 & \frac{1}{2}\Omega_P e^{i\psi_P} & 0 \\ \frac{1}{2}\Omega_P^* e^{i\psi_P} & \Delta_P & \frac{1}{2}\Omega_S e^{i\psi_S} \\ 0 & \frac{1}{2}\Omega_S^* e^{i\psi_S} & \Delta_P - \Delta_S \end{bmatrix} \begin{bmatrix} C_1(t) \\ C_e(t) \\ C_2(t) \end{bmatrix} \tag{B.23}$$

where

$$\Omega_P(t) = V_P \mathcal{E}_P(t)/\hbar\,, \quad \Omega_S(t) = V_S \mathcal{E}_S(t)/\hbar \tag{B.24}$$

The coupling strength between the states is determined by the Rabi frequencies $\Omega_S(t)$ and $\Omega_P(t)$, while the detuning from the intermediate state or from the two-photon resonance appears as the elements on the diagonal: $\hbar\Delta_P = E_e - E_1 - \hbar\omega_P$ is the detuning (energy) of the pump laser from resonance with the $|1\rangle$-$|e\rangle$ transition and $\hbar\Delta_S = E_e - E_2 - \hbar\omega_S$ is the detuning of the Stokes laser from the $|e\rangle$-$|2\rangle$ transition. We define the single-photon detuning as $\Delta \equiv \Delta_P$ and two-photon detuning as $\delta \equiv \Delta_P - \Delta_S$.

APPENDIX C

Dipole moment in a periodic potential

Here, we show that how the expression $\boldsymbol{D} = \langle u_v, \Phi_h | \, \boldsymbol{e} \cdot \boldsymbol{d} \, | u_c, \Phi_e \rangle$ reduces to $\langle u_v | \, \boldsymbol{e} \cdot \boldsymbol{d} \, | u_c \rangle \, \langle \Phi_h | \Phi_e \rangle$. First, we replace the dipole moment operator by $q\,\mathbf{r}$, where q is the electric charge.

$$\boldsymbol{D} = q \, \langle u_v, \Phi_h | \, \mathbf{e} \cdot \boldsymbol{r} \, | u_c, \Phi_e \rangle = q \, \boldsymbol{e} \cdot \langle u_v, \Phi_h | \, \boldsymbol{r} \, | u_c, \Phi_e \rangle \tag{C.1}$$

The Bloch function u is periodic and fulfills $u(\boldsymbol{r} + \boldsymbol{R}) = u(\boldsymbol{r})$, here $\boldsymbol{R}$ is an arbitrary lattice vector. We write $\langle u_v, \Phi_h | \, \boldsymbol{r} \, | u_c, \Phi_e \rangle$ as:

$$\boldsymbol{D}_1 = \langle u_v, \Phi_h | \, \boldsymbol{r} \, | u_c, \Phi_e \rangle = \int u_v^*(\boldsymbol{r}) \Phi_h^*(\boldsymbol{r}) \, \boldsymbol{r} \, u_c(\boldsymbol{r}) \Phi_e(\boldsymbol{r}) \, d\boldsymbol{r} \tag{C.2}$$

We now split the integral (C.2) into a sum of integrals over the various atomic unit cells of index i and we assume that the envelop function $\Phi(\boldsymbol{r})$ varies slowly, so that it may be approximated to a constant Φ_i within the atomic unit cell i. This leads to:

$$\boldsymbol{D}_1 = \sum_i \Phi_{h,i}^* \Phi_{e,i} \int\limits_{\text{unit cell}i} u_v^*(\boldsymbol{r}) \, \boldsymbol{r} \, u_c(\boldsymbol{r}) \, d\boldsymbol{r} \tag{C.3}$$

where the integration is performed within the unit cell i. Defining $\boldsymbol{r}'$ as an arbitrary lattice vector within the unit cell we have $\boldsymbol{r} = \boldsymbol{r}_i + \boldsymbol{r}'$. Thus by

changing variables (C.3) is split into two separate terms:

$$\begin{aligned}\boldsymbol{D}_1 = \sum_i \Phi^*_{h,i}\Phi_{e,i}\,\boldsymbol{r}_i \int\limits_{\text{unit cell}i} u^*_v(\boldsymbol{r}_i+\boldsymbol{r}')\; u_c(\boldsymbol{r}_i+\boldsymbol{r}')\,d\boldsymbol{r}' + \\ \sum_i \Phi^*_{h,i}\Phi_{e,i} \int\limits_{\text{unit cell}i} u^*_v(\boldsymbol{r}_i+\boldsymbol{r}')\,\boldsymbol{r}'\,u_c(\boldsymbol{r}_i+\boldsymbol{r}')\,d\boldsymbol{r}'\end{aligned} \tag{C.4}$$

Since the Bloch function is periodic, we have $u(\boldsymbol{r}_i+\boldsymbol{r}') = u(\boldsymbol{r}')$ and the integrals are thus identical for all the unit cells. Then we can put them outside the sums and we obtain:

$$\begin{aligned}\boldsymbol{D}_1 = \frac{1}{V_{uc}} \int\limits_{\text{unit cell}i} u^*_v(\boldsymbol{r}')\; u_c(\boldsymbol{r}')\,d\boldsymbol{r}' \sum_i \Phi^*_{h,i}\Phi_{e,i}\,\boldsymbol{r}_i\,V_{uc} + \\ \frac{1}{V_{uc}} \int\limits_{\text{unit cell}i} u^*_v(\boldsymbol{r}')\,\boldsymbol{r}'\,u_c(\boldsymbol{r}')\,d\boldsymbol{r}' \sum_i \Phi^*_{h,i}\Phi_{e,i}\,V_{uc} \\ \cong \langle u_v|u_c\rangle \int \Phi^*_v(\boldsymbol{r})\Phi_c(\boldsymbol{r})\boldsymbol{r}d\boldsymbol{r} + \langle u_v|\boldsymbol{r}'|u_c\rangle \int \Phi^*_v(\boldsymbol{r})\Phi_c(\boldsymbol{r})d\boldsymbol{r}\end{aligned} \tag{C.5}$$

where we also converted the Riemann sums for the envelop functions to integrals. In a transition between the conduction band and the valence band which is called an interband transition even without knowledge of the exact form of the Bloch function, the following relation hold due to symmetry arguments

$$\langle u_v|u_c\rangle = 0 \quad \text{Interband} \tag{C.6}$$

Then, for interband transition, the dipole moment becomes

$$\boldsymbol{D}_1 = \langle u_v|\boldsymbol{r}|u_c\rangle \int \Phi^*_h(\boldsymbol{r})\Phi_e(\boldsymbol{r})\,\boldsymbol{r}\,d\boldsymbol{r} \tag{C.7}$$

Then we can write:

$$\boldsymbol{D} = q\,\boldsymbol{e}\cdot\boldsymbol{D}_1 = \langle u_v|\,\boldsymbol{e}\cdot\boldsymbol{d}\,|u_c\rangle\,\langle\Phi_h|\Phi_e\rangle \tag{C.8}$$

APPENDIX D

Complementary results on exciton states

In this chapter, we bring some results which provide more detail about the exciton states. we have considered a crystal-phase type-II QD in a nanowire with geometrical parameters as: $l_{NW} = 90$ nm, $h_{QD} = 4$ nm, and $d_{QD} = 36$ nm. For calculating the exciton states in this structure, we first calculated the single-particle states. There is one single-particle electron bound state in the z direction ($n_e = 1$) and there are many single-particle hole states in the valence band in the z direction. We considered ten lowest-energy hole states in the calculation ($n_h = 1...10$). There are also many single-particle electron and hole states in the transverse plane, we consider 19 lowest-energy single-particle states in the transverse plane for both the electron and hole as: $(l\ m)_{e/h} = (0\ 0), (0\ 1), (0\ -1), (0\ 2), (0\ -2), (1\ 0), (0\ 3), (0\ -3), (1\ 1), (1\ -1), (0\ 4), (0\ -4), (1\ 2), (1\ -2), (2\ 0), (0\ 5), (0\ -5), (1\ 3), (1\ -3)$. By this consideration the Coulomb matrix has **13,032,100** elements but we don't need to calculate all of them. Since the Hamiltonian is Hermitian and it is equal to its own conjugate transpose $H_{ij} = \overline{H_{ji}}$. Then, we just need to calculate the diagonal elements and either the elements above the diagonal or below the diagonal. By considering this fact, we need to calculate **6,517,855** matrix elements. The condition in (3.8) also computationally simplifies the calculation such that we just calculate elements which meet this condition.

By considering this, the number of elements which we need to calculate will be **600,896** which is less than 5% of the initial number. The main exciton properties of the mentioned structure has been discussed in Chapter 3. Here, we bring some complementary results. Table. D.1 shows the lowest-energy contributing single-particle elements to the ground-state exciton. Figure D.1 shows $|\Psi_{exc}(\boldsymbol{r}_e, \boldsymbol{r}_h)|^2$ the lowest energy exciton states probability density calculated from Eq. (3.10). Table. D.2 provides the oscillator strength and the energy correspond to these exciton states.

	$i := (n,l,m)_e$	$j := (n,l,m)_h$	R %		$i := (n,l,m)_e$	$j := (n,l,m)_h$	R %
N_0	1,0,0	1,0,0	13.1	N_{21}	1,0,0	2,0,3	0
N_1	1,0,0	2,0,0	23.76	N_{22}	1,0,0	4,0,-1	0
N_2	1,0,0	1,0,-1	0	N_{23}	1,0,0	4,0,1	0
N_3	1,0,0	1,0,1	0	N_{24}	1,0,0	3,1,0	0
N_4	1,0,0	2,0,-1	0	N_{25}	1,0,0	1,1,-1	0
N_5	1,0,0	2,0,1	0	N_{26}	1,0,0	1,1,1	0
N_6	1,0,0	3,0,0	18.26	N_{27}	1,0,0	2,1,-1	0
N_7	1,0,0	1,0,-2	0	N_{28}	1,0,0	2,1,1	0
N_8	1,0,0	1,0,2	0	N_{29}	1,0,0	1,0,-4	0
N_9	1,0,0	1,1,0	0	N_{30}	1,0,0	1,0,4	0
N_{10}	1,0,0	3,0,-1	0	N_{31}	1,0,0	5,0,0	4.91
N_{11}	1,0,0	3,0,1	0	N_{32}	1,0,0	3,0,-3	0
N_{12}	1,0,0	2,0,-2	0	N_{33}	1,0,0	3,0,3	0
N_{13}	1,0,0	2,0,2	0	N_{34}	1,0,0	4,0,-2	0
N_{14}	1,0,0	2,1,0	0	N_{35}	1,0,0	4,0,2	0
N_{15}	1,0,0	4,0,0	10	N_{36}	1,0,0	4,1,0	0
N_{16}	1,0,0	1,0,-3	0	N_{37}	1,0,1	2,0,-4	0
N_{17}	1,0,0	1,0,3	0	N_{38}	1,0,0	2,0,4	0
N_{18}	1,0,0	3,0,-2	0	N_{39}	1,0,0	3,1,-1	0
N_{19}	1,0,0	3,0,2	0	N_{40}	1,0,0	3,1,1	0
N_{20}	1,0,0	2,0,-3	0	N_{41}	1,0,0	5,0,-1	0

Table D.1: The lowest-energy single-particle components which are contributing to the ground-state exciton oscillator strength of a type-II SQD in a nanowire with geometrical parameters of $l_{NW} = 70$ nm, $d_{QD} = 36$ nm, $h_{QD} = 4$ nm.

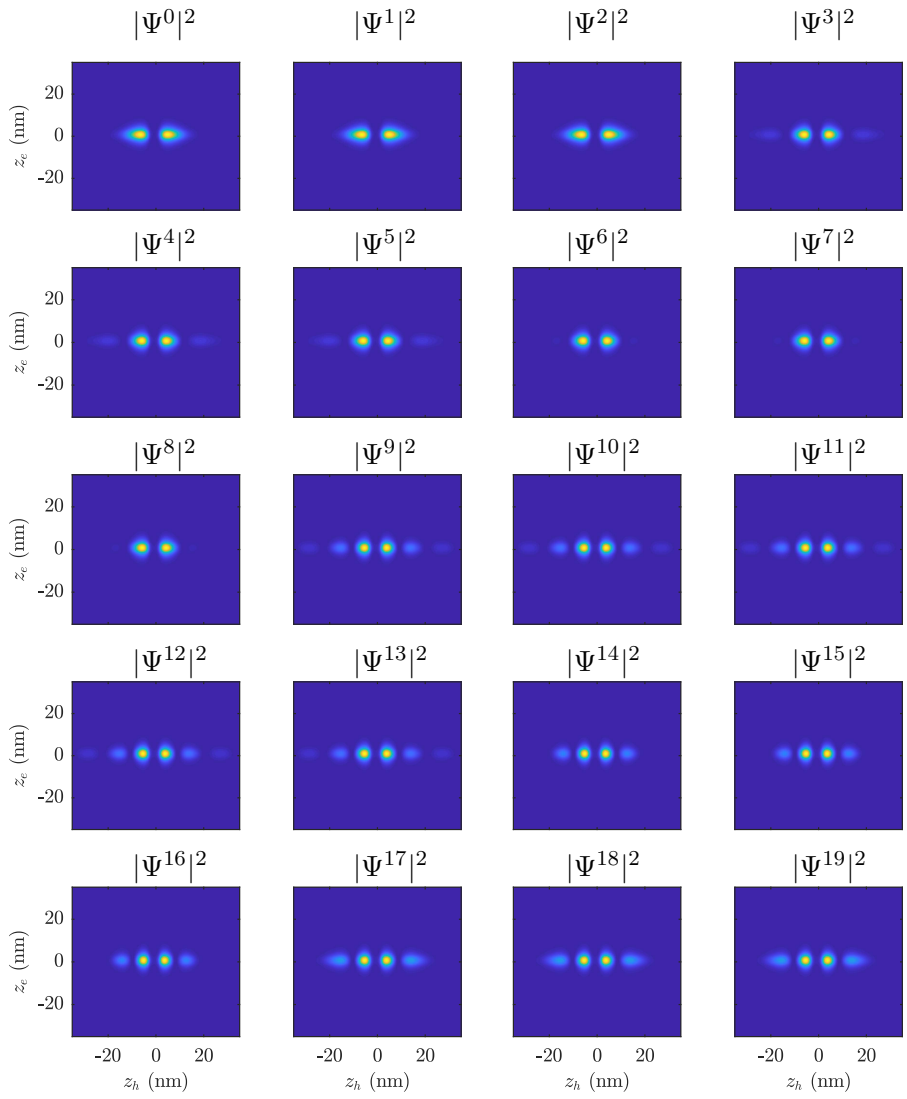

Figure D.1: The lowest-energy exciton states probability densities $|\Psi_{exc}(\boldsymbol{r}_h, \boldsymbol{r}_e)|^2$ for $R_e = R_h = 0$ in a type-II SQD with geometrical parameters: $l_{NW} = 70$ nm, $h_{QD} = 4$ nm, $d_{QD} = 36$ nm.

Exciton state	E_{ex} (meV)	OS_N%
Ψ^0	77.02	35.82
Ψ^1	79.92	0
Ψ^2	79.92	0
Ψ^3	81.03	7.89
Ψ^4	83.15	0
Ψ^5	83.15	0
Ψ^6	83.35	1.34
Ψ^7	83.44	0
Ψ^8	83.44	0
Ψ^9	83.79	9.89
Ψ^{10}	85.84	0
Ψ^{11}	85.84	0
Ψ^{12}	86.37	0
Ψ^{13}	86.37	0
Ψ^{14}	86.72	6.22
Ψ^{15}	86.84	0
Ψ^{16}	86.84	0
Ψ^{17}	87.20	5.12
Ψ^{18}	88.10	0
Ψ^{19}	88.10	0

Table D.2: The exciton states oscillator strength and energy of a type-II SQD in a nanowire with geometrical parameters of $l_{NW} = 70$ nm, $d_{QD} = 36$ nm, $h_{QD} = 4$ nm.

	$i :=$ $(n,l,m)_e$	$j :=$ $(n,l,m)_h$	R %		$i :=$ $(n,l,m)_e$	$j :=$ $(n,l,m)_h$	R %
N_0	1,0,0	1,0,0	60.1 %	N_{21}	1,0,-1	1,0,-3	0 %
N_1	1,0,0	1,0,-1	0 %	N_{22}	1,0,-1	1,0,3	0 %
N_2	1,0,0	1,0,1	0 %	N_{23}	1,0,-1	1,1,-1	0 %
N_3	1,0,0	1,0,-2	0 %	N_{24}	1,0,-1	1,1,1	0 %
N_4	1,0,0	1,0,2	0 %	N_{25}	1,0,-1	1,0,-4	0 %
N_5	1,0,0	1,1,0	0 %	N_{26}	1,0,-1	1,0,4	0 %
N_6	1,0,0	1,0,-3	0 %	N_{27}	1,0,-1	1,1,-2	0 %
N_7	1,0,0	1,0,3	0 %	N_{28}	1,0,-1	1,1,2	0 %
N_8	1,0,0	1,1,-1	0 %	N_{29}	1,0,-1	1,2,0	0 %
N_9	1,0,0	1,1,1	0 %	N_{30}	1,0,1	1,0,0	0 %
N_{10}	1,0,0	1,1,1	0 %	N_{31}	1,0,1	1,0,-1	10.1 %
N_{11}	1,0,0	1,0,-4	0 %	N_{32}	1,0,1	1,0,1	0 %
N_{12}	1,0,0	1,0,4	0 %	N_{33}	1,0,1	1,0,-2	0 %
N_{13}	1,0,0	1,1,-2	0 %	N_{34}	1,0,1	1,0,2	0 %
N_{14}	1,0,0	1,2,0	0 %	N_{35}	1,0,1	1,1,0	0 %
N_{15}	1,0,-1	1,0,0	0 %	N_{36}	1,0,1	1,0,-3	0 %
N_{16}	1,0,-1	1,0,-1	0 %	N_{37}	1,0,1	1,0,3	0 %
N_{17}	1,0,-1	1,0,1	10.1 %	N_{38}	1,0,1	1,1,-1	0 %
N_{18}	1,0,-1	1,0,-2	0 %	N_{39}	1,0,1	1,1,1	0 %
N_{19}	1,0,-1	1,0,2	0 %	N_{40}	1,0,1	1,0,-4	0 %
N_{20}	1,0,-1	1,1,0	0 %	N_{41}	1,0,1	1,0,4	0 %

Table D.3: The lowest-energy single-particle components which are contributing to the ground-state exciton oscillator strength of a type-I SQD in a nanowire with geometrical parameters of $l_{NW} = 60$ nm, $d_{QD} = 30$ nm, $h_{QD} = 2$ nm.

Bibliography

[1] D. P. DiVincenzo, "The physical implementation of quantum computation," *Fortschritte der Physik*, vol. 48, no. 9-11, pp. 771–783, 2000.

[2] A. K. Ekert, "Quantum cryptography based on Bell's theorem," *Physical Review Letters*, vol. 67, no. 6, pp. 661–663, 1991.

[3] M. A. Nielsen and I. L. Chuang, *Quantum Computation and Quantum Information*, 2010.

[4] A. M. Steane, "Efficient fault-tolerant quantum computing," *Nature*, vol. 399, no. 6732, p. 21, 1998.

[5] E. Knill, R. Laflamm, and W. H. Zurek, "Resilient quantum computation: Error models and thresholds," *Proceedings of the Royal Society A: Mathematical, Physical and Engineering Sciences*, vol. 454, no. 1969, pp. 365–384, 1998.

[6] D. J. Wineland, M. Barrett, J. Britton, J. Chiaverini, B. DeMarco, W. M. Itano, B. Jelenkovic, C. Langer, D. Leibfried, V. Meyer, T. Rosenband, and T. S. Z, "Quantum information processing with trapped ions," *The royal society*, vol. 361, pp. 1349–1361, 2003.

[7] Q. A. Turchette, C. J. Hood, W. Lange, H. Mabuchi, and H. J. Kimble, "Measurement of conditional phase shifts for quantum logic," vol. 75, no. 25, pp. 4710–4713, 1995.

[8] M. Atature, J. Dreiser, A. Badolato, A. Hogele, K. Karrai, and A. Imamoglu, "Quantum-dot spin-state preparation with near-unity fidelity," vol. 312, pp. 551–554, 2006.

[9] D. Hite, Y. Colombe, A. Wilson, D. Allcock, D. Leibfried, D. Wineland, and D. Pappas, "Surface science for improved ion traps," *MRS Bulletin*, vol. 38, no. 10, pp. 826–833, 2013.

[10] L. Gordon, J. R. Weber, J. B. Varley, A. Janotti, D. D. Awschalom, and C. G. V. de Walle, "Quantum computing with defects," *MRS Bulletin*, vol. 38, no. 10, pp. 802–808, 2013.

[11] D. Loss and D. P. DiVincenzo, "Quantum computation with quantum dots," *Physical Review A*, vol. 57, no. 1, pp. 120–126, 1998.

[12] M. Kroutvar, Y. Ducommun, D. Heiss, M. Bichler, D. Schuh, G. Abstreiter, and J. J. Finley, "Optically programmable electron spin memory using semiconductor quantum dots," *Nature*, vol. 432, pp. 81–84, 2004.

[13] W. D. Oliver and P. B. Welander, "Materials in superconducting quantum bits," *MRS Bulletin*, vol. 38, no. 10, pp. 816–825, 2013.

[14] R. Hanson, L. P. Kouwenhoven, J. R. Petta, S. Tarucha, and L. M. K. Vandersypen, "Spins in few-electron quantum dots," *Reviews of Modern Physics*, vol. 79, no. 4, pp. 1217–1265, 2007.

[15] J. R. Petta, A. C. Johnson, J. M. Taylor, E. A. Laird, A. Yacoby, M. D. Lukin, C. M. Marcus, M. P. Hanson, and A. C. Gossard, "Coherent Manipulation of Coupled Electron Spins in Semiconductor Quantum Dots," *Science*, vol. 309, pp. 2180–2184, 2005.

[16] M. D. Shulman, O. E. Dial, S. P. Harvey, H. Bluhm, V. Umansky, and A. Yacoby, "Demonstration of entanglement of electrostatically coupled singlet-triplet qubits," *Science*, vol. 336, no. 6078, pp. 202–205, 2012.

[17] S. M. Frolov, S. R. Plissard, Stevan Nadj-Perge, L. P. Kouwenhoven, and Erik P.A.M. Bakkers, "Quantum computing based on semiconductor nanowires," *MRS Bulletin*, vol. 38, no. 10, pp. 809–815, 2013.

[18] E. Biolatti, R. C. Iotti, P. Zanardi, and F. Rossi, "Quantum Information Processing with Semiconductor Macroatoms," *Physical Review Letters*, vol. 85, no. 26, pp. 5647–5650, 2000.

[19] F. Troiani, E. Molinari, and U. Hohenester, "High-finesse optical quantum gates for electron spins in artificial molecules," *Physical Review Letters*, vol. 90, no. 20, p. 206802, 2003.

[20] D. V. Talapin and Y. Yin, "Themed issue: Chemical transformations of nanoparticles," *Journal of Materials Chemistry*, vol. 21, no. 31, pp. 11 454–11 456, 2011.

[21] W. J. Baumgardner, Z. Quan, J. Fang, and T. Hanrath, "Timing matters: The underappreciated role of temperature ramp rate for shape control and reproducibility of quantum dot synthesis," *Nanoscale*, vol. 4, no. 12, pp. 3625–3628, 2012.

[22] J. J. Finley, M. Sabathil, P. Vogl, G. Abstreiter, R. Oulton, A. I. Tartakovskii, D. J. Mowbray, M. S. Skolnick, S. L. Liew, A. G. Cullis, and M. Hopkinson, "Quantum-confined Stark shifts of charged exciton complexes in quantum dots," *Physical Review B - Condensed Matter and Materials Physics*, vol. 70, no. 20, pp. 2–5, 2004.

[23] N. Akopian, G. Patriarche, L. Liu, J. C. Harmand, and V. Zwiller, "Crystal phase quantum dots," *Nano Letters*, vol. 10, no. 4, pp. 1198–1201, 2010.

[24] M. Bouwes Bavinck, K. D. Jöns, M. Zieliński, G. Patriarche, J. C. Harmand, N. Akopian, and V. Zwiller, "Photon cascade from a single crystal phase nanowire quantum dot," *Nano Letters*, vol. 16, no. 2, pp. 1081–1085, 2016.

[25] D. Spirkoska, J. Arbiol, A. Gustafsson, S. Conesa-Boj, F. Glas, I. Zardo, M. Heigoldt, M. H. Gass, A. L. Bleloch, S. Estrade, M. Kaniber, J. Rossler, F. Peiro, J. R. Morante, G. Abstreiter, L. Samuelson, and A. Fontcuberta I Morral, "Structural and optical properties of high quality zinc-blende/wurtzite GaAs nanowire heterostructures," *Physical Review B - Condensed Matter and Materials Physics*, vol. 80, no. 24, pp. 1–9, 2009.

[26] C. Fasth, A. Fuhrer, M. T. Bjork, and L. Samuelson, "Tunable double quantum dots in InAs nanowires defined by local gate electrodes," *Nano Letters*, vol. 5, no. 7, pp. 1487–1490, 2005.

[27] Y. Hu, H. O. Churchill, D. J. Reilly, J. Xiang, C. M. Lieber, and C. M. Marcus, "A Ge/Si heterostructure nanowire-based double quantum dot with integrated charge sensor," *Nature Nanotechnology*, vol. 2, no. 10, pp. 622–625, 2007.

[28] M. Cai, Y. Liu, W. Liu, and T. Yu, "Binding energy of the exciton in type-II quantum wells," *Physica B: Physics of Condensed Matter*, vol. 176, no. 4, pp. 327–333, 1992.

[29] K. Pemasiri, M. Montazeri, R. Gass, L. M. Smith, H. E. Jackson, J. Yarrison-Rice, S. Paiman, Q. Gao, H. H. Tan, C. Jagadish, X. Zhang, and J. Zou, "Carrier dynamics and quantum confinement in type II ZB-WZ InP nanowire homostructures," *Nano Letters*, vol. 9, no. 2, pp. 648–654, 2009.

[30] G. W. Bryant, "Excitons in quantum boxes: Correlation effects and quantum confinement," *Physical Review B*, vol. 37, no. 15, pp. 8763–8772, 1988.

[31] G. Bastard, E. E. Mendez, L. L. Chang, and L. Esaki, "Exciton binding energy in quantum wells," *Physical Review B*, vol. 26, no. 4, pp. 1974–1979, 1982.

[32] F. Troiani, U. Hohenester, and E. Molinari, "Electron-hole localization in coupled quantum dots," *Physical Review B - Condensed Matter and Materials Physics*, vol. 65, no. 16, pp. 1–4, 2002.

[33] M. Taherkhani, M. Willatzen, J. Mork, N. Gregersen, and D. P. McCutcheon, "Type-II quantum-dot-in-nanowire structures with large oscillator strength for optical quantum gate applications," *Physical Review B*, vol. 96, no. 12, pp. 1–9, 2017.

[34] J. I. Climente, C. Segarra, F. Rajadell, and J. Planelles, "Electrons, holes, and excitons in GaAs polytype quantum dots," *Journal of Applied Physics*, vol. 119, no. 12, 2016.

[35] Y. Z. Hu, M. Lindberg, and S. W. Koch, "Theory of optically excited intrinsic semiconductor quantum dots," *Physical Review B*, vol. 42, no. 3, pp. 1713–1723, 1990.

[36] A. Barenco and M. A. Dupertuis, "Quantum many-body states of excitons in a small quantum dot," *Physical Review B*, vol. 52, no. 4, pp. 2766–2778, 1995.

[37] G. Jacopin, L. Rigutti, L. Largeau, F. Fortuna, F. Furtmayr, F. H. Julien, M. Eickhoff, and M. Tchernycheva, "Optical properties of wurtzite/zinc-blende heterostructures in GaN nanowires," *Journal of Applied Physics*, vol. 110, no. 6, 2011.

[38] L. Zhang, J. W. Luo, A. Zunger, N. Akopian, V. Zwiller, and J. C. Harmand, "Wide InP nanowires with wurtzite/zincblende superlattice segments are type-II whereas narrower nanowires become type-I: An atomistic pseudopotential calculation," *Nano Letters*, vol. 10, no. 10, pp. 4055–4060, 2010.

[39] P. Corfdir and P. Lefebvre, "Importance of excitonic effects and the question of internal electric fields in stacking faults and crystal phase quantum discs: The model-case of GaN," *Journal of Applied Physics*, vol. 112, no. 5, 2012.

[40] E. Ribeiro, A. O. Govorov, W. Carvalho, and G. Medeiros-Ribeiro, "Aharonov-Bohm signature for neutral polarized excitons in type-II quantum dot ensembles," *Physical Review Letters*, vol. 92, no. 12, pp. 1–4, 2004.

[41] B. Bansal, M. Hayne, M. Geller, D. Bimberg, and V. V. Moshchalkov, "Excitonic Mott transition in type-II quantum dots," *Physical Review B - Condensed Matter and Materials Physics*, vol. 77, no. 24, pp. 4–7, 2008.

[42] S. Kim, Y. T. Lim, E. G. Soltesz, A. M. De Grand, J. Lee, A. Nakayama, J. A. Parker, T. Mihaljevic, R. G. Laurence, D. M. Dor, L. H. Cohn, M. G. Bawendi, and J. V. Frangioni, "Near-infrared fluorescent type II quantum dots for sentinel lymph node mapping," *Nature Biotechnology*, vol. 22, no. 1, pp. 93–97, 2004.

[43] T. Unold, K. Mueller, C. Lienau, T. Elsaesser, and A. D. Wieck, "Optical control of excitons in a pair of quantum dots coupled by the Dipole-Dipole interaction," *Physical Review Letters*, vol. 94, no. 13, pp. 1–4, 2005.

[44] G. Ortner, M. Bayer, Y. Lyanda-Geller, T. L. Reinecke, A. Kress, J. P. Reithmaier, and A. Forchel, "Control of vertically coupled InGaAs/GaAs quantum dots with electric fields," *Physical Review Letters*, vol. 94, no. 15, pp. 1–4, 2005.

[45] X. Li, Y. Wu, D. Steel, D. Gammon, T. H. Stievater, D. S. Katzer, D. Park, C. Piermarocchi, and L. J. Sham, "An all-optical quantum gate in a semiconductor quantum dot," *Science*, vol. 301, no. 5634, pp. 809–811, 2003.

[46] A. Zrenner, E. Beham, S. Stufler, F. Findeis, M. Bichler, and G. Abstreiter, "Coherent properties of a two-level system based on a quantum-dot photodiode," *Nature*, vol. 418, no. 6898, pp. 612–614, 2002.

[47] A. Barenco, D. Deutsch, A. Ekert, and R. Jozsa, "Conditional quantum dynamics and logic gates," *Physical Review Letters*, vol. 74, no. 20, pp. 4083–4086, 1995.

[48] I. Vurgaftman, J. R. Meyer, and L. R. Ram-Mohan, "Band parameters for III-V compound semiconductors and their alloys," *Journal of Applied Physics*, vol. 89, no. 11 I, pp. 5815–5875, 2001.

[49] L. M. Ramaniah and S. V. Nair, "Optical absorption in semiconductor quantum dots: A tight-binding approach," *Physical Review B*, vol. 47, no. 12, pp. 7132–7139, 1993.

[50] L. E. Brus, "A simple model for the ionization potential, electron affinity, and aqueous redox potentials of small semiconductor crystallites," *The Journal of Chemical Physics*, vol. 79, no. 11, pp. 5566–5571, 1983.

[51] W. Kohn, "Quantum theory of cyclotron resonance in semiconductors: general theory," *Physical Review*, vol. 102, no. 4, p. 1956, 1956.

[52] E. O. Kane, "Band structure of indium antimonide," *Journal of Physics and Chemistry of Solids*, vol. 1, no. 4, pp. 249–261, 1957.

[53] C. R. Pidgeon and R. N. Brown, "Interband magneto-absorption and faraday rotation in InSb," *Physical Review*, vol. 146, no. 2, pp. 575–583, 1966.

[54] J. A. Majewski and P. Vogl, *Quantum theory of structure: Tight-binding systems.* Elsevier B.V., 1989, vol. 2.

[55] L. Goodwin, A. J. Skinner, and D. G. Pettifor, "Generating transferable tight-binding parameters: Application to silicon," *europhysics letters*, vol. 9, no. 7, pp. 701–706, 1989.

[56] G. Klimeck, R. C. Bowen, T. B. Boykin, C. Salazar-Lazaro, T. A. Cwik, and A. Stoica, "Si tight-binding parameters from genetic algorithm fitting," *Superlattices and Microstructures*, vol. 27, no. 2, pp. 77–88, 2000.

[57] G. Klimeck, R. C. Bowen, T. B. Boykin, and T. A. Cwik, "Sp3s* Tight-Binding Parameters for Transport Simulations in Compound Semiconductors," *Superlattices and Microstructures*, vol. 27, no. 5, pp. 519–524, 2000.

[58] J. Kim, L. W. Wang, and A. Zunger, "Comparison of the electronic structure of pyramidal quantum dots with different facet orientations," *Physical Review B - Condensed Matter and Materials Physics*, vol. 57, no. 16, pp. R9408–R9411, 1998.

[59] C. E. Pryor and M. E. Pistol, "Atomistic k. p theory," *Journal of Applied Physics*, vol. 118, no. 22, 2015.

[60] P. Lodahl, S. Mahmoodian, and S. Stobbe, "Interfacing single photons and single quantum dots with photonic nanostructures," *Reviews of Modern Physics*, vol. 87, no. 2, pp. 347–400, 2015.

[61] P. Carpena, J. A. Lo, and V. Gasparian, "Energy dependence of the effective mass in the envelope-function approximation," *Physica B*, vol. 253, pp. 242–249, 1998.

[62] P. E. D. F. Junior and G. M. Sipahi, "Electronic band structure of polytypical nanowhiskers," *Physics Procedia*, vol. 28, pp. 72–78, 2012.

[63] P. E. Faria Junior and G. M. Sipahi, "Band structure calculations of InP wurtzite/zinc-blende quantum wells," *Journal of Applied Physics*, vol. 112, no. 10, 2012.

[64] L. A. Coldren, S. W. Corzine, and Milan L. Masanovic, *Diode lasers and photonic integrated circuits*, 1989, vol. 53.

[65] M. Bayer, O. Stern, P. Hawrylak, S. Fafard, and A. Forchel, "Hidden symmetries in the energy levels of excitonic artificial atoms," *Nature*, vol. 405, no. 6789, pp. 923–926, 2000.

[66] R. Rinaldi, P. V. Giugno, R. Cingolani, H. Lipsanen, M. Sopanen, J. Tulkki, and H. Lipsanen, "Zeeman effect in parabolic quantum dots," *Physical Review Letters*, vol. 77, no. 2, pp. 342–345, 1996.

[67] N. Baer, P. Gartner, and F. Jahnke, "Coulomb effects in semiconductor quantum dots," *The European Physical Journal B*, vol. 42, no. 2, pp. 231–237, 2004.

[68] Elias Goldmann, "From Structure to Spectra: Tight-Binding Theory of InGaAs Quantum Dots," Master of Science Thesis, University of Bremen.

[69] H. W. Van Kesteren, E. C. Cosman, W. A. Van Der Poel, and C. T. Foxon, "Fine structure of excitons in type-II GaAs/AlAs quantum wells," *Physical Review B*, vol. 41, no. 8, pp. 5283–5292, 1990.

[70] E. Blackwood, M. J. Snelling, R. T. Harley, S. R. Andrews, and C. T. B. Foxon, "Exchange interaction of excitons in GaAs heterostructures," *Physical Review B*, vol. 50, no. 19, pp. 14 246–14 254, 1994.

[71] M. Bayer, A. Kuther, A. Forchel, A. Gorbunov, V. B. Timofeev, F. Schäfer, and J. P. Reithmaier, "Electron and hole g factors and exchange interaction from studies of the exciton fine structure in In0 . 60Ga 0 . 40As quantum dots," *Physical Review Letters*, vol. 82, no. 8, pp. 22–25, 1999.

[72] B. R. Salmassi and G. E. W. Bauer, "Exchange interaction in type -II quantum wells," *Physical Review B*, vol. 39, no. 3, pp. 1970–1972, 1989.

[73] V. Krapek, P. Klenovský, and T. Sikola, "Type-I and type-II confinement in quantum dots: Excitonic fine structure," *Acta Physica Polonica A*, vol. 129, no. 1, pp. A66–A69, 2016.

[74] C. J. Cramer, *Essentials of computational chemistry theories and models*, 2004, vol. 2.

[75] P. Navratil, S. Quaglioni, I. Stetcu, and B. R. Barrett, "Recent developments in no-core shell-model calculations," *Journal of Physics G: Nuclear and Particle Physics*, vol. 36, no. 8, 2009.

[76] E. Waltersson, C. J. Wesslén, and E. Lindroth, "Performance of the coupled-cluster singles and doubles method applied to two-dimensional quantum dots," *Physical Review B - Condensed Matter and Materials Physics*, vol. 87, no. 3, pp. 1–11, 2013.

[77] L. S. Cederbaum, O. E. Alon, and A. I. Streltsov, "Coupled-cluster theory for systems of bosons in external traps," *Physical Review A - Atomic, Molecular, and Optical Physics*, vol. 73, no. 4, pp. 1–13, 2006.

[78] F. Pederiva, C. J. Umrigar, and E. Lipparini, "Diffusion Monte Carlo study of circular quantum dots," *Physical Review B*, vol. 62, no. 12, pp. 8120–8125, 2000.

[79] A. Harju, "Variational Monte Carlo for interacting electrons in quantum dots," *Journal of Low Temperature Physics*, vol. 140, no. 3-4, pp. 181–210, 2005.

[80] K. Bergmann, H. Theuer, and B. W. Shore, "Coherent population transfer among quantum states of atoms and molecules," *Rev. Mod. Phys.*, vol. 70, no. 3, pp. 1003–1023, 1998.

[81] N. V. Vitanov, A. A. Rangelov, B. W. Shore, and K. Bergmann, "Stimulated Raman adiabatic passage in physics, chemistry, and beyond," *Reviews of Modern Physics*, vol. 89, no. 1, pp. 1–66, 2017.

[82] X. Lacour, N. Sangouard, S. Guérin, and H. R. Jauslin, "Arbitrary state controlled-unitary gate by adiabatic passage," *Physical Review A - Atomic, Molecular, and Optical Physics*, vol. 73, no. 4, pp. 1–6, 2006.

[83] I. I. Beterov, M. Saffman, E. A. Yakshina, V. P. Zhukov, D. B. Tretyakov, V. M. Entin, I. I. Ryabtsev, C. W. Mansell, C. Maccormick, S. Bergamini, and M. P. Fedoruk, "Quantum gates in mesoscopic atomic ensembles based on adiabatic passage and Rydberg blockade," *Physical Review A - Atomic, Molecular, and Optical Physics*, vol. 88, no. 1, pp. 1–5, 2013.

[84] T. Pellizzari, S. A. Gardiner, J. I. Cirac, and P. Zoller, "Decoherence, continuous observation, and quantum computing: A cavity QED model," *Physical Review Letters*, vol. 75, no. 21, pp. 3788–3791, 1995.

[85] N. Sangouard, X. Lacour, S. Guérin, and H. R. Jauslin, "Fast SWAP gate by adiabatic passage," *Physical Review A - Atomic, Molecular, and Optical Physics*, vol. 72, no. 6, pp. 1–5, 2005.

[86] A. Kuhn, G. W. Coulston, G. Z. He, S. Schiemann, K. Bergmann, and W. S. Warren, "Population transfer by stimulated Raman scattering with delayed pulses using spectrally broad light," *The Journal of Chemical Physics*, vol. 96, no. 6, pp. 4215–4223, 1992.

[87] M. Scala, B. Militello, A. Messina, and N. V. Vitanov, "Stimulated Raman adiabatic passage in an open quantum system: Master equation

approach," *Physical Review A - Atomic, Molecular, and Optical Physics*, vol. 81, no. 5, pp. 1–7, 2010.

[88] P. A. Ivanov, N. V. Vitanov, and K. Bergmann, "Spontaneous emission in stimulated Raman adiabatic passage," *Physical Review A - Atomic, Molecular, and Optical Physics*, vol. 72, no. 5, pp. 1–8, 2005.

[89] Y. B. Band and P. S. Julienne, "Population transfer by multiple stimulated Raman scattering," *Journal of Chemical Physics*, vol. 95, no. 8, pp. 5681–5685, 1991.

[90] M. Scala, B. Militello, A. Messina, and N. V. Vitanov, "Microscopic description of dissipative dynamics of a level-crossing transition," *Physical Review A - Atomic, Molecular, and Optical Physics*, vol. 84, no. 2, pp. 1–5, 2011.

[91] J. R. Kuklinski, U. Gaubatz, F. T. Hioe, and K. Bergmann, "Adiabatic population transfer in a three-level system driven by delayed laser pulses," *Physical Review A*, vol. 40, no. 11, pp. 6–9, 1989.

[92] N. V. Vitanov, M. Fleischhauer, B. W. Shore, and K. Bergmann, *Coherent manipulation of atoms and molecules by sequential laser pulses*, 2001, vol. 46.

[93] M. Kumagai and T. Takagahara, "Excitonic and nonlinear-optical properties of dielectric quantum-well structures," *Physical Review B*, vol. 40, no. 18, pp. 12 359–12 381, 1989.

[94] T. Takagahara, "Effects of dielectric confinement and electron-hole exchange interaction on excitonic states in semiconductor quantum dots," *Physical Review B*, vol. 47, no. 8, pp. 4569–4584, 1993.

[95] L. Medina and E. Ley Koo, "Mathematics motivated by physics: The electrostatic potential is the Coulomb integral transform of the electric charge density," *Revista Mexicana de Fisica E*, vol. 54, no. 2, pp. 153–159, 2008.

[96] P. Tighineanu, R. Daveau, E. H. Lee, J. D. Song, S. Stobbe, and P. Lodahl, "Decay dynamics and exciton localization in large GaAs quantum

dots grown by droplet epitaxy," *Physical Review B - Condensed Matter and Materials Physics*, vol. 88, no. 15, pp. 1–13, 2013.

[97] A. Reigue, J. Iles-Smith, F. Lux, L. Monniello, M. Bernard, F. Margaillan, A. Lemaitre, A. Martinez, D. P. McCutcheon, J. Mørk, R. Hostein, and V. Voliotis, "Probing electron-phonon interaction through two-photon interference in resonantly driven semiconductor quantum dots," *Physical Review Letters*, vol. 118, no. 23, pp. 1–6, 2017.

[98] S. Stobbe, P. T. Kristensen, J. E. Mortensen, J. M. Hvam, J. Mørk, and P. Lodahl, "Spontaneous emission from large quantum dots in nanostructures: Exciton-photon interaction beyond the dipole approximation," *Physical Review B - Condensed Matter and Materials Physics*, vol. 86, no. 8, 2012.

[99] H. J. Krenner, M. Sabathil, E. C. Clark, A. Kress, D. Schuh, M. Bichler, G. Abstreiter, and J. J. Finley, "Direct observation of controlled coupling in an individual quantum dot molecule," *Physical Review Letters*, vol. 94, no. 5, pp. 1–4, 2005.

[100] E. A. Stinaff, M. Scheibner, A. S. Bracker, I. V. Ponomarev, V. L. Korenev, M. E. Ware, M. F. Doty, T. L. Reinecke, and D. Gammon, "Optical signatures of coupled quantum dots," *Science*, vol. 636, no. 2006, pp. 636–640, 2010.

[101] Lucio Robledo, J. Elzerman, G. Jundt, M. Atatüre, A. Högele, S. Fält, and Atac Imamoglu, "Conditional dynamics of interacting quantum dots," *Science*, vol. 320, no. May, pp. 772–776, 2008.

[102] O. Gywat, G. Burkard, and D. Loss, "Biexcitons in coupled quantum dots as a source of entangled photons," *Physical Review B - Condensed Matter and Materials Physics*, vol. 65, no. 20, pp. 2 053 291–2 053 295, 2002.

[103] M. Bayer, P. Hawrylak, K. Hinzer, S. Fafard, M. Korkusinski, Z. R. Wasilewski, O. Stern, and A. Forchel, "Coupling and entangling of quantum states in quantum dot molecules," *Science*, vol. 291, no. 5503, pp. 451–453, 2001.

[104] J. J. Garcia-Ripoll and J. I. Cirac, "Quantum computation with unknown parameters," *Physical Review Letters*, vol. 90, no. 12, 2003.

[105] P. Zanardi and M. Rasetti, "Holonomic quantum computation," *Quantum Error Correction*, vol. 9780521897, pp. 397–411, 2012.

[106] K. Kim, M. S. Chang, S. Korenblit, R. Islam, E. E. Edwards, J. K. Freericks, G. D. Lin, L. M. Duan, and C. Monroe, "Quantum simulation of frustrated Ising spins with trapped ions," *Nature*, vol. 465, no. 7298, pp. 590–593, 2010.

[107] Z. Kis and F. Renzoni, "Qubit rotation by stimulated Raman adiabatic passage," *Physical Review A*, vol. 65, no. 3, pp. 1–4, 2002.

[108] O. Marquardt, M. Ramsteiner, P. Corfdir, L. Geelhaar, and O. Brandt, "Modeling the electronic properties of GaAs polytype nanostructures: Impact of strain on the conduction band character," *Physical Review B*, vol. 95, no. 24, pp. 1–8, 2017.

[109] U. Bockelmann and G. Bastard, "Phonon scattering and energy relaxation in two-, one-, and zero-dimensional electron gases," *Physical Review B*, vol. 42, no. 14, pp. 8947–8951, 1990.

[110] M. Trif, V. N. Golovach, and D. Loss, "Spin-spin coupling in electrostatically coupled quantum dots," *Physical Review B - Condensed Matter and Materials Physics*, vol. 75, no. 8, pp. 1–14, 2007.

[111] A. V. Kuhlmann, J. Houel, A. Ludwig, L. Greuter, D. Reuter, A. D. Wieck, M. Poggio, and R. J. Warburton, "Charge noise and spin noise in a semiconductor quantum device," *Nature Physics*, vol. 9, no. 9, pp. 570–575, 2013.

[112] D. Press, K. De Greve, P. L. McMahon, T. D. Ladd, B. Friess, C. Schneider, M. Kamp, S. Höfling, A. Forchel, and Y. Yamamoto, "Ultrafast optical spin echo in a single quantum dot," *Nature Photonics*, vol. 4, no. 6, pp. 367–370, 2010.

[113] E. V. Denning, J. Iles-Smith, D. P. McCutcheon, and J. Mork, "Protocol for generating multiphoton entangled states from quantum dots in the

presence of nuclear spin fluctuations," *Physical Review A*, vol. 96, no. 6, pp. 1–9, 2017.

[114] G. Éthier-Majcher, D. Gangloff, R. Stockill, E. Clarke, M. Hugues, C. Le Gall, and M. Atatüre, "Improving a Solid-State Qubit through an Engineered Mesoscopic Environment," *Physical Review Letters*, vol. 119, no. 13, pp. 1–6, 2017.

[115] X. Xu, B. Sun, P. R. Berman, D. G. Steel, A. S. Bracker, D. Gammon, and L. J. Sham, "Coherent population trapping of an electron spin in a single negatively charged quantum dot," *Nature Physics*, vol. 4, no. 9, pp. 692–695, 2008.

[116] A. Greilich, D. R. Yakovlev, A. Shabaev, a. L. Efros, I. a. Yugova, R. Oulton., V. Stavarache, D. Reuter, A. Weick, and M. Bayer, "Mode locking of electron spin coherence in singly charged quantum dots." *Science*, vol. 313, no. 5785, pp. 341–345, 2006.

[117] B. B. Zhou, A. Baksic, H. Ribeiro, C. G. Yale, F. J. Heremans, P. C. Jerger, A. Auer, G. Burkard, A. A. Clerk, and D. D. Awschalom, "Accelerated quantum control using superadiabatic dynamics in a solid-state lambda system," *Nature Physics*, vol. 13, no. 4, pp. 330–334, 2017.

[118] B. J. Liu, Z. H. Huang, Z. Y. Xue, and X. D. Zhang, "Superadiabatic holonomic quantum computation in cavity QED," *Physical Review A*, vol. 95, no. 6, pp. 1–6, 2017.

[119] M. V. Berry, "Transitionless quantum driving," *Journal of Physics A: Mathematical and Theoretical*, vol. 42, no. 36, 2009.

[120] X. Yan, X. Zhang, J. Li, Y. Wu, and X. Ren, "Self-catalyzed growth of pure zinc blende 110 InP nanowires," *Applied Physics Letters*, vol. 107, no. 2, p. 023101, 2015.

[121] N. G. Stoltz, P. M. Petroff, and R. J. Warburton, "A coherent single-hole spin in a semiconductor," *Science*, vol. 325, no. July, pp. 70–73, 2009.

[122] K. Bergmann, N. V. Vitanov, and B. W. Shore, "Perspective: Stimulated Raman adiabatic passage: The status after 25 years," *Journal of Chemical Physics*, vol. 142, no. 17, 2015.

[123] B. W. Shore, "Picturing stimulated Raman adiabatic passage: a STIRAP tutorial," *Advances in Optics and Photonics*, vol. 9, no. 3, p. 563, 2017.

[124] M. Russ, D. M. Zajac, A. J. Sigillito, F. Borjans, J. M. Taylor, J. R. Petta, and G. Burkard, "High-fidelity quantum gates in Si/SiGe double quantum dots," *Physical Review B*, vol. 97, no. 8, pp. 1–9, 2018.

[125] T. S. Koh, S. N. Coppersmith, and M. Friesen, "High-fidelity gates in quantum dot spin qubits," *PNAS*, vol. 110, no. 49, pp. 19 695–19 700, 2013.

[126] M. Abramowitz, I. A. Stegun, and D. Miller, "Handbook of mathematical functions with formulas, graphs and mathematical tables (National bureau of standards applied mathematics series No. 55)," p. 239, 1965.